

MASSIVE STAR CLUSTER EVOLUTION IN ACTION: THE EXTREME
ENVIRONMENTAL IMPACTS OF WOLF-RAYET STARS

Kimberly Rene Sokal
Glenwood Springs, Colorado

B.A. in Physics and Astrophysics, University of Colorado at Boulder, 2009

M.S. in Astronomy, University of Virginia, 2012

A Dissertation Presented to the Graduate
Faculty of the University of Virginia
in Candidacy for the Degree of
Doctor of Philosophy

Department of Astronomy

University of Virginia
June, 2016

Committee Members:

Prof. Kelsey E. Johnson
Prof. Rémy Indebetouw
Prof. Aaron S. Evans
Prof. Herman H. Shugart

© Copyright by
Kimberly Rene Sokal
All rights reserved
June 10, 2016

Abstract

Massive stars modify their environment with ionizing photons, fast winds, and eventual supernova explosions; feedback that is enhanced when the stars are clustered. The highest concentrations of massive stars are found in massive and super star clusters, which represent some of the most intense regions of star formation and can dominate the energetics of a galaxy. Massive star clusters form in thick, dense envelopes of natal material that largely obscure the early cluster evolution. However, massive stars forming within the embedded cluster ionize the surrounding material, making the cluster detectable at radio wavelengths. These stars then blow away the surrounding material, eventually revealing the cluster at optical wavelengths. However, this transition is not well understood, despite implications for the fate of the cluster itself and its impact on the local environment and host galaxy.

With my thesis, I highlight an overlooked yet potentially significant source of feedback – Wolf-Rayet (WR) stars – that may contribute to cluster emergence. Previous works suggested that massive star clusters will have cleared out their natal material before the massive stars have evolved into the WR phase, during which huge amounts of ionization and mechanical feedback are output. Yet, I identified a massive star cluster, S26 in the galaxy NGC 4449, that challenges that expectation. S26 was originally detected as a radio source and was surprisingly observed to host WR stars. Due to S26, I hypothesize the WR feedback provides the tipping point in the combined feedback processes that drive a massive star cluster to emerge. I follow up this discovery with an observational survey to investigate the role of WR stars in massive star cluster evolution. Using optical spectra to search for WR signatures in a radio-selected sample, I present a sample of 45 emerging massive star clusters, 21 with significant detections of the WR signature. Additionally, I find that the sources with highest extinctions do not host WR stars and have ages beyond the onset of the WR phase, which may indicate that clusters without WR stars stay embedded for longer periods of time. This thesis has vastly expanded the number of known “emerging WR clusters”, as well as revealed a possible acceleration of the removal of natal material in clusters hosting WRs compared to those without.

Acknowledgements

First of all, I must say thank you to my thesis committee, Kelsey, Remy, Aaron, and Hank, for your time and guidance. From there, I have so many people that I am grateful for, and as such, this list is by no means exhaustive.

To Kelsey: You ended your own thesis with the notion that a rough road leads to the stars. I agree, but often worried that the only way was *ad astra per alia porci*. Thank you for helping me bypass needing pigs to fly, by taking one step at a time. For your undying enthusiasm and promotion of scientific curiosity, for finding ways to get me past my lows, for teaching me to promote my achievements (and have them) and effectively communicate science, for supporting and sometimes forcing my independence, and ultimately for your advisement for and beyond the technical science stuff, I owe many of my graduate accomplishments and growth to you.

To Remy: You have been an important source of knowledge, critique, and aid throughout this process. I would also like to thank you for caring about me as a person and reassuring me early on about my ability to be an astronomer.

To Phil: Thank you for your sage advice and collaboration, as well as so much more; from your encouragement to braving high elevation observing to welcoming me into your home with your family.

To Steve: I began my journey as an astronomer as your research assistant. I appreciate the opportunities you gave me, which are far beyond a typical undergraduate's reach, and all that you taught me.

To my colleagues and officemates/ academic family: Thank you for your time, shared experiences, and acceptance. Sabrina, I look up to your strength and charisma. LM, thanks for teaching me so many tricks of the trade. Sandy and Lauren, I am grateful for our nail painting parties, the sharing of talents, our commiserating, your generosity, and you both making me feel appreciated.

A huge shout-out to all of my friends. Good times and general distractions have been had by all. Thanks for all the beers. Sarah and Jo, I never would have made it past the first couple of years of graduate school without you. Jenni and Kels, thanks for being my loving forever friends, ignoring such great distances apart.

To Chris: There is no way to fully sum up all of the gratitude that I have for you; I am so lucky to have you in my life. You have been my biggest supporter, and you always know how best to do so. Here is to exploring the world and eating our way through it, wandering in the wilderness, running 10 miles, sunny days in vineyards, chill nights in, and many happy times. Thank you.

To my parents, I love you. Thank you for always being there for me, particularly when others are not. You have been extremely supportive, and thank you for saying so. I appreciate the care packages and you dropping whatever you are doing to answer how long I should boil an egg. I am extremely proud of you for taking full advantage of your retirement; I love the photos of your adventures.

To DSBK-ers: Outreach has provided me with a greater sense of value beyond learning and doing science. My participation in Dark Skies, Bright Kids! reminded me every week how fun astronomy can be while also helping to provide access to science to those who rarely get it. I sincerely thank all of the DSBK coaches and volunteers for starting and continuing this worthy mission.

Lastly, the inclusion of women is the first step to change the perception that science is not a womens activity. Likely because many of those with whom I work consciously address this issue, I feel I have been more fortunate than many. Thanks to those of you who help promote women and the disadvantaged. Keep pushing for astronomy to be better.

Table of contents

Abstract	ii
Acknowledgements	iii
List of Figures	xiii
List of Tables	xiv
1 Introduction	1
1.1 Wolf-Rayet Stars	1
1.1.1 The Origin of the “Wolf and Rayet” Term	1
1.1.2 The Spectra and Subtypes of WR Stars	4
1.1.3 Understanding the Evolution of Classical WR Stars	5
1.2 Massive and Super Star Clusters	10
1.2.1 The Discovery of Bright, Blue, Compact Extragalactic Star Clusters	10
1.2.2 Terminology: Massive Star Clusters versus Super Star Clusters	15
1.2.3 The Evolution of Massive Star Clusters	17
1.2.4 Fate: Globular Cluster or Dissipation?	20
1.3 Feedback	22
1.3.1 The Feedback Mechanisms	22
1.3.2 Potential for WR Stars to Increase Feedback	26
1.4 Contents of This Thesis	29
2 An Emerging Wolf-Rayet Massive Star Cluster in NGC 4449	31
2.1 Overview	31
2.2 Background	32
2.3 Observations and Data Reduction	36
2.3.1 Optical Spectra from APO	36
2.3.2 Infrared Archival Data	37
2.3.2.1 <i>Spitzer</i> IRAC and MIPS	37
2.3.2.2 <i>Herschel</i> PACS and SPIRE	37
2.4 General Properties of S26	40

2.4.1	Extinction	40
2.4.2	Electron Temperatures, Density, and Pressure	41
2.4.3	Metallicity via Oxygen Abundance	41
2.4.4	Age	42
2.5	WR Features and the Massive Star Populations	43
2.5.1	Determining the Number of WR Stars	43
2.5.2	Determining the Number of O-stars	45
2.6	The Thermal Radio Component of S26	46
2.7	Dissecting the Dust	49
2.7.1	Photometry	49
2.7.2	SED of S26	50
2.7.3	The Best Fit Dust and Grain Model	51
2.7.4	Dust Mass and Star Formation Efficiency	52
2.8	Discussion	55
2.8.1	Massive Star Populations of S26 in Context	55
2.8.1.1	Estimates through STARBURST99	55
2.8.1.2	WR Population Trends with Metallicity	56
2.8.1.3	Additional Considerations	59
2.8.2	Impact of the Massive Stars on the Cluster Evolution	60
2.8.2.1	The Potential Ionized Bipolar Outflow in S26	60
2.8.2.2	The Importance of Winds from Evolved Stars	62
2.8.2.3	Describing the Evolutionary Phase of S26	64
2.8.3	Similarities to 30 Doradus in the LMC	64
2.9	Summary	67
3	The Prevalence and Impact of Wolf-Rayet Stars in Emerging Massive Star Clusters	70
3.1	Overview	70
3.2	Background	71
3.3	The Sample Selection: Emerging Massive Star Clusters	75
3.4	Observations	78
3.4.1	Optical Spectra	79
3.4.2	Optical Archival Imaging	81
3.5	Detecting WR Emission	81
3.5.1	Identifying the WR Bump	81
3.5.2	Classifications According to Observed WR Emission	86
3.6	Characterizing the Environments	88
3.6.1	Photometry	88
3.6.2	Nebular Emission Line Measurements and Corrections	88
3.6.3	Nebular Properties	89
3.6.3.1	Interstellar Extinction	89
3.6.3.2	Ionized Gas Density and Temperature	90

3.6.3.3	Metallicity	90
3.6.4	Estimating the Ionizing Flux	94
3.6.5	Fundamental Properties and STARBURST99 Models	95
3.6.6	Determining the Massive Star Populations	97
3.7	Results	99
3.7.1	The Commonality of WR Stars in Radio-selected Emerging Clusters	99
3.7.2	Comparing the Massive Star Populations	103
3.7.3	Evaluating Whether the Sources are Still Embedded	105
3.7.4	The Excitation of the Sample	106
3.7.5	A Different Population: Non-WR Clusters	109
3.8	Conclusions and Discussion	117
	Appendix A: Source Spectra and Images	120
4	Summary	132
	References	136

List of Figures

1.1	An original drawing from 1890 showing the mysterious blue band observed in the spectra of the bright Wolf-Rayet stars compared to the lines of the Bunsen flame based on Vogel’s observations.	2
1.2	An <i>Hubble Space Telescope</i> image capturing the explosive mass loss nebula of the WR star WR 124. This image showcases the spectacular result of the stellar winds ejecting material, and the star can be seen glowing in the center.	4
1.3	A view of the characteristic emission lines in WR spectra. From Crowther (2007), optical spectroscopy of WR stars in the Milky Way, in which the variations in line strengths between different WR subtypes are clear. The most well known line featured in the spectra of WN stars is He II 4686 Å and for WC stars, C IV at 5808 Å.	6
1.4	A cartoon from Eldridge (2008) depicting the life cycle and structure of a massive star from the main sequence through the stages of a RSG, WR, and eventual supernova as a Type Ib/c.	8
1.5	Figure 1 from Massey (2013) showing the evolution of massive stars by plotting the Geneva evolutionary tracks (Ekström et al. 2012) at solar metallicity. Regardless of initial stellar mass, the evolution is quite flat.	9
1.6	A grey scale color map (B-V) of the merger remnant NGC 3597. The star forming regions are derived from this map, and are clearly unresolved, yet their properties were indicative of young globular clusters.	12
1.7	A Wide Field Camera image of the Antennae galaxy, observed before the <i>HST</i> servicing mission. Other than a few foreground stars, each point-like object is a star cluster.	13
1.8	A stunning modern view of the Antennae galaxy, imaged by the Advanced Camera for Surveys (ACS) on <i>HST</i>	14
1.9	A plot from Portegies Zwart et al. (2010) that clearly displays the mass function of young clusters (< 1 Gyr) in various galaxies. The dotted and dashed curves represent a Schechter function with a turnover mass M_* as indicated, which may depend on galactic environment. As the general shape of the mass function is a power law, the distinction between massive star clusters and SSCs is somewhat arbitrary.	16

1.10	A cartoon diagram of the evolution of massive star clusters from K.E. Johnson, depicting the expected similarities of the evolutionary stages of a single massive star to that of the massive star clusters.	18
1.11	The dominant feedback mechanism in an observation study of massive star clusters in the LMC appears to be warm gas pressure (due to photoionization), as shown by this figure from Lopez et al. (2014), however it is suspected that radiation pressure may be more important at earlier times.	24
1.12	Various simulations from Dale et al. (2014) showing resulting morphologies of the cold natal gas of a massive star cluster that may be cleared out by feedback: (top left) control with no feedback, (top right) ionization, (bottom left) stellar winds, and (bottom right) winds and ionization.	25
1.13	The increased potential for feedback is clear in the most recent stellar evolutionary codes (Ekström et al. 2012). Top: from Fierlinger et al. (2016), the mass loss and kinetic energy are shown. Bottom: from Topping & Shull (2015), the ionizing photon rates also show enhancements over the WR phase.	27
2.1	An <i>HST</i> rgb image ($H\alpha$, I, B) showing nebular emission surrounding a compact optical cluster in S26. The green contours show emission at 3.6 μm (Reines et al. 2008).	34
2.2	Flux calibrated spectra taken with DIS on the 3.5 m Telescope at Apache Point Observatory of the cluster S26 in NGC 4449, zoomed in on the broad Wolf-Rayet features. The dotted line shows the subtracted nebular features. Top—The “blue bump,” a composite of broad lines at 4640 \AA , 4650 \AA , and 4686 \AA . Bottom—The broad “red bump” centered at 5808 \AA	35
2.3	An infrared view of the massive cluster S26 in NGC 4449. From top left moving clockwise: an <i>Spitzer</i> IRAC rgb image (3.6, 5.8, and 8.0 μm), <i>Spitzer</i> MIPS 24 μm , <i>Herschel</i> PACS R (170 μm), and <i>Herschel</i> SPIRE PLW (500 μm). The extraction regions for constructing the source SED (Fig. 2.6) are plotted in red (small 5” \sim 100 pc circle) and green (large 15” \sim 300 pc circle). S26 is a dominate source of emission even at the longest wavelengths.	39
2.4	STARBURST99 predictions for the cluster age vs. the equivalent width of the $H\beta$ (4861 \AA) line (see Section 2.8.1.1). The observed EW of $H\beta$ for the massive star cluster S26 in NGC 4449 (solid line with uncertainties shown as a shadowed region) implies an age of 3.1 ± 0.3 Myr.	42

- 2.5 Identifying the thermal radio component in the radio SED of S26, as observed by Reines et al. (2008), with a χ^2 fit to the observed fluxes of the expected emission assuming thermal emission goes as $F_\nu \propto \nu^{-0.1}$ while non-thermal emission as $F_\nu \propto \nu^{-0.7}$. Top: constraining the fit such that the radius is set to 50 pc, as observed by the irregular 3σ contour of the radio continuum, the flux has non-thermal contributions of 14% at 1.3 cm. Bottom: allowing the radius to be a free parameter (although under-constraining the fit) results in an increased non-thermal contribution of 28% at 1.3 cm from a region of radius 2.3 pc. 48
- 2.6 An SED of the optical to far-IR emission from the massive star cluster S26 with dust and grain models over plotted for comparison. Optical spectra (green line) is from Reines et al. (2010), and a STARBURST99 model (dotted green line) clearly demonstrates an abundance of IR emission to the expected stellar emission. The IR photometry and dust and grain model fitting utilize two apertures: a small 5" aperture used to extract emission from images with native PSFs, and a large 15" aperture used to extract emission from images convolved to the resolution of SPIRE 500 μm . The best fit dust and grain model from Draine & Li (2007) are plotted for the corresponding aperture (large or small), where the dotted line shows the model spectra and the empty circular dots show the photometric fluxes. The SED clearly shows strong PAH features and large amounts of dust surrounding S26. The change in PAH emission in the IRAC bands at 5.8 and 8.0 μm and the shift in the peak IR emission can be seen between the two IR aperture SEDs, plausibly due to increased exciting radiation and destruction of PAHs toward the cluster center. 51
- 2.7 The estimated age vs. the observed WR and O-star populations, and WR/O population ratio, of the cluster S26 (data points). The evolutionary synthesis model of STARBURST99 (Leitherer 1999), which utilizes a Kroupa IMF with upper and lower limits of 0.1 - 120 M_\odot 56
- 2.8 A compilation of observed population ratios in nearby galaxies compared to different predictions. Star points show the observed ratios in the massive star cluster S26 in NGC 4449. Lines show model predictions of (Meynet & Maeder 2005) (dotted; including stellar rotation) and computed results for new models from the Geneva group for $Z = 0.006$ (Neugent et al. 2012) and $Z = 0.014$ (Georgy et al. 2012). 57
- 2.9 An *HST* $H\alpha$ image zoomed in on S26, showing the morphology of a bipolar ionized outflow. 61

2.10	The optical and radio estimated properties of S26 plotted on the extragalactic H II region size-density relation (Gilbert & Graham 2007; Hunt & Hirashita 2009). As discussed in Section 2.6, the observed radio emission can be modeled with an input radius of 50 pc or with the radius as a free parameter.	65
3.1	Optical spectra observed with the 4m Mayall Telescope at KPNO of a subset of the WR clusters. Dashed lines indicate the location of the broad WR bumps, and a zoom in on the WR bumps is shown in the figure on the right, where a roughly traced continuum guides the eye.	79
3.2	Archival <i>HST</i> images ($H\alpha$, B, I) of the target galaxies NGC 2366 and NGC 4449. Insets are zoomed in on sample sources, with the corresponding region overlaid on the host galaxy image with a white square for ease of comparison. White circles ($2''5$) are overlaid and show the extraction regions used for photometry. The line style of this overlaid circle indicates the source's classification: solid for WR clusters, dot-dash for Candidate clusters, and dotted for Non-WR clusters.	82
3.3	A scatter plot showing the sensitivity to identifying a significantly detected WR feature. The colored lines are estimated detection limits adopting an observed FWHM of the WR feature from the sample (as indicated in the legend of either the minimum or weighted average) and requiring a 3σ detection.	86
3.4	The radio spectral index α plotted vs. the 6 cm flux density. WR clusters are the star markers color-coded by host galaxy and "No-bump" sources are the gray squares (both Non-WR clusters and Other classes included here). It is clear that the "No-bump" and WR clusters sample the same parameter space.	87
3.5	Histograms of the V-band photometric luminosity of the sample. Colors indicate the WR cluster class, and the black hatches indicate the Non-WR clusters. Left: the raw (observed) luminosity distribution of both classes is similar. Right: the extinction-corrected (intrinsic) luminosity distribution shows some differences between sources with and without WR stars, highlighting that some of the Non-WR clusters exhibit higher extinctions and thus are intrinsically brighter.	89
3.6	Ages of the sources in the sample (with WR clusters on the left, and Non-WR clusters on the right) as estimated by the measured equivalent width (EW) of $H\beta$ and predictions from STARBURST99 models, with the appropriate metallicity track plotted as separate panels.	97
3.7	The distributions of the stellar cluster mass, obtained by scaling the V-band photometry to STARBURST99 models, of the sample.	98

3.8 A pie chart clearly shows the distribution of the classes observed in my sample, with emerging WR clusters as the most common and making up $\sim 50\%$ of the sample. From (Sokal et al. 2015b). 102

3.9 STARBURST99 (Leitherer et al. 1999) predictions for the behavior of the equivalent width of the WR emission at 4686 \AA for all relevant metallicity tracks. It is clear that the WR emission is not constant over the WR phase. 103

3.10 The estimated ratio of the number of WR stars to O-stars plotted with STARBURST99 predictions (dotted line). The estimated populations ratios of sources in this sample are generally consistent with the STARBURST99 models, occasionally somewhat higher. 105

3.11 Populations ratios estimated for these sources in comparison to their metallicity (left: WC/WN, right: WR/O). Observations of other regions, both individual star-forming regions and averaged galactic areas, are overplotted. Uncertainties clutter the plot, but it is clear that the population ratios are similar to predictions and other regions. 106

3.12 A plot comparing the ionized flux inferred from thermal radio emission to that inferred from optical nebular $H\beta$ emission. The colors are the same as Figure 3.4. Most sources show a higher ionizing flux inferred from the radio than from the optical observations, suggestive that the sources are still partially embedded. 107

3.13 The BPT diagram (Baldwin et al. 1981) used to evaluate the excitation mechanisms. This full sample spans across the diagram. Generally, the sample is also above where average SDSS star-forming galaxies lie shown by the dotted line (Brinchmann et al. 2008) and borders the theoretical and empirical limits that are produced by star formation along that are shown as dashed and dotted-dashed lines (Kewley et al. 2001; Kauffmann et al. 2003). 108

3.14 A look into the ages and extinctions of the sources in the sample. The top/right panel shows a histogram of ages/extinctions and the distribution of these properties are markedly different between the two classes of emerging massive star clusters (WR clusters in pink, non-WR clusters in gray). The main figure shows these properties in comparison as extinction versus age. The most highly extincted sources do not have detected WR features and tend to have larger ages. 110

3.15 Similar to Figure 3.14, the age versus the ratio of the ionizing flux estimated from radio to that from $H\beta$, which serves as an extinction measure as well. The Non-WR clusters tend to occupy the upper right side of the plot in comparison to the WR clusters. 111

3.16	A plot showing the cumulative distribution functions (CDF) of the extinctions of the WR and Non-WR clusters. I perform the Kolmogorov-Smirnov (KS) test and the Anderson-Darling (AD) test on the distributions of the ages and extinctions. For the extinction distributions, p -values of 0.0003 (KS test) and 0.0009 (AD test) were found, showing that the extinction distributions of the two classes are statistically different. The age distributions are similarly statistically different. . .	112
A1	Optical spectra observed with the 4m Mayall Telescope at KPNO and the 6.5m MMT of another subset of the WR clusters, otherwise the same as Figure 3.1.	120
A2	Optical spectra observed with the 6.5m MMT of the rest of the WR clusters, otherwise the same as Figure 3.1.	121
A3	Optical spectra observed with the 4m Mayall Telescope at KPNO and the 6.5m MMT of a subset of the ‘no-bump’ sources, otherwise the same as Figure 3.1 without the zoom-in panels of WR feature regions.	122
A4	Optical spectra observed with the 6.5m MMT of the rest of the ‘no-bump’ sources, otherwise the same as Figure A3.	123
A5	Archival <i>HST</i> and KP 2.1m images ($H\alpha$, B, I) of the target galaxies NGC 4214 and NGC 6946. Insets and overlaid regions are the same as 3.2 with the exception that the extracted region and corresponding overlaid circle on source NGC 4214 - Object 15/16 is $4''0$	124
A6	Archival <i>HST</i> images ($H\alpha$, B, I) of the target galaxy M51. Insets and overlaid regions are the same as Figure 3.2.	125

List of Tables

1.1	Initial Stellar Mass	8
2.1	Emission Line Properties of S26	38
2.2	Massive Star Populations in S26	45
2.3	SED of S26: Photometry and Model Parameters	53
3.1	Target Host Galaxies	77
3.2	Classification and the WR Features	84
3.2	Classification and the WR Features	85
3.3	Source Properties	91
3.4	Nebular Properties of the WR Clusters	92
3.5	Massive Star Populations in the WR Clusters	100
A1	Optical Spectral Observations	126
A1	Optical Spectral Observations	127
A2	Archival V-Band Imaging Observations	128
A3	Optical Characteristics of the Sample	129
A4	Emission Line Fluxes for WR Clusters ^a	130
A5	Emission Line Fluxes for Non-WR Clusters ^a	131

Chapter 1

Introduction

1.1 Wolf-Rayet Stars

1.1.1 The Origin of the “Wolf and Rayet” Term

In contrast to the spectra of most stars, which show absorption lines, three stars whose spectra instead exhibited emission lines were discovered at the Paris Observatory in 1867 by Charles Wolf and Georges Rayet. Wolf and Rayet noted a bright blue band in each of the three stellar spectra, and soon several additional of these Wolf-Rayet stars were discovered (Huggins & Huggins 1890, see sketches of the spectra in Figure 1.1). At the time, the origin of this blue band was perplexing, the report by Huggins & Huggins (1890) stated “we regret that the insufficiency of our instrumental means has left our examination of the spectra of these stars less complete than we could wish.” It was clear that by showing emission lines, the Wolf-Rayet spectra were similar to that of planetary nebula, except that these stars displayed no signs of nebulosity. Comparison to a Bunsen flame ruled out that the line could be due to hydrogen, and a hydrocarbon origin was also rejected. The astounding conclusion to this story, which is an important reminder about difficulties of scientific inquiries, is that the blue emission line is now known to result from helium, which was not discovered until 1868. The characteristic emission line observed by Wolf and Rayet that originally defined these Wolf-Rayet spectra is He II at 4686 Å.

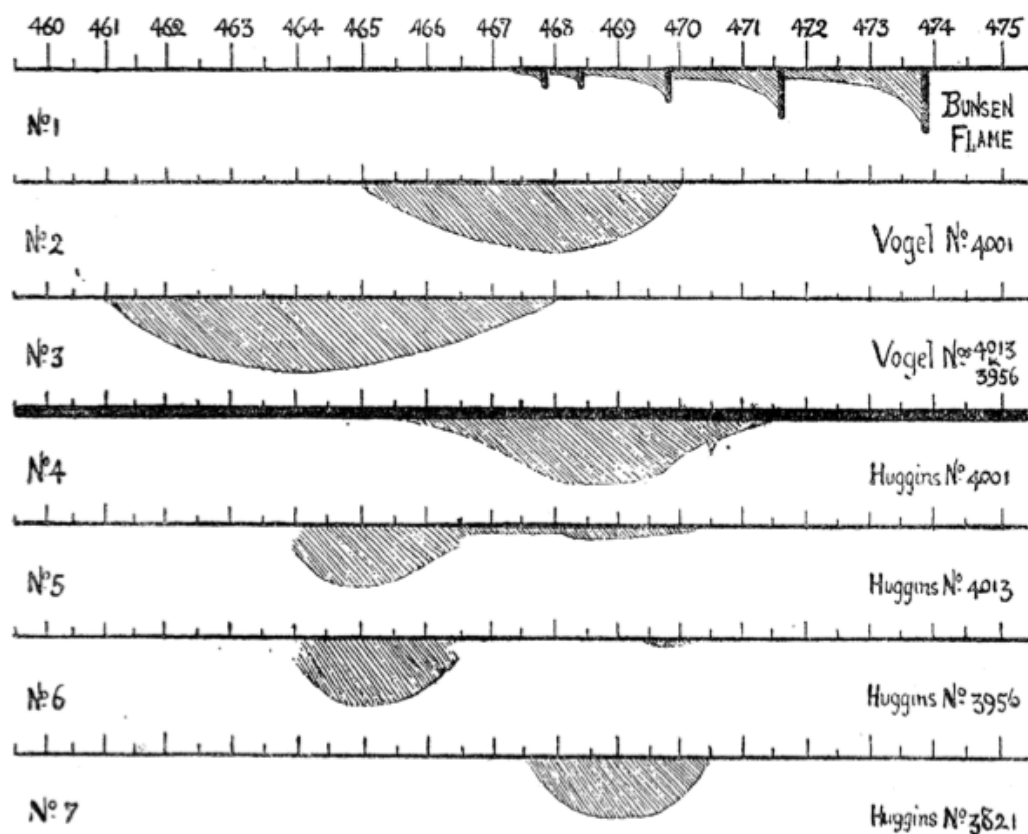


Fig. 1.1.— An original drawing from 1890 showing the mysterious blue band observed in the spectra of the bright Wolf-Rayet stars compared to the lines of the Bunsen flame based on Vogel's observations; from Huggins & Huggins (1890).

The Wolf-Rayet, hereafter WR, descriptor is now used as a spectral classification of broad emission lines from stellar burning products of ionized helium, nitrogen, or carbon that become observable due to considerable mass loss, this phenomenon likely due to the Eddington factor (proximity to the Eddington limit) (Vink 2015). The Eddington limit is the maximal luminosity of a star, above which radiation pressure would drive an outflow. It quickly became apparent that WR spectra have two flavors: nitrogen-rich (WN) and carbon-rich (WC). The WR spectra are displayed by a heterogeneous set of objects: classic WR stars, extremely high mass stars that also show hydrogen in emission (WNh and Of/WN stars), central stars of planetary nebula, and certain supernova. It is the first two types, which are massive stars with ties to star formation and the power to alter their surroundings, for which the

Wolf-Rayet name is best known. Yet, the later share similar spectral characteristics. The central stars of planetary nebula (CSPNe) are the evolved cores of stellar mass stars that are exposed after the Asymptotic Giant Branch (AGB) phase, which also produce the planetary nebulae. As the cores of the AGB stars are composed of carbon and oxygen, the CSPNe can thus display the carbon-rich WC lines in their spectra in addition to nebular emission lines and are denoted by square brackets ([WC4] for instance). Much more rare, a supernova will display a WR spectrum for only a few hours (Liu et al. 2000; Groh 2014), during which helium is quickly accelerated by the ejecta. These supernova are named, for clarity, with an “X” by some, such that the spectral typing is XWN4 (Groh 2014).

Classical WR stars are massive stars ($> 25 M_{\odot}$) in their advanced evolutionary stages, and have exposed their helium-burning core by shedding the outer layers off the star with high mass loss rates and fast stellar winds. Gamow (1943) first suggested that nuclear processed material may be responsible for the spectral appearance of WR stars. Conti (1976) then realized that these nuclear burning products were revealed by significant mass loss due to stellar winds. This evolutionary scheme, called the Conti scenario (Maeder 1983), can be likened to peeling off the layers of an onion, where the strong stellar winds are shedding the outer layers off the star to expose the chemically evolved regions within, displaying H-burning products and subsequently He-burning products. WR stars are several million times brighter than the Sun (Crowther 2007) and have temperatures from 30,000 to 200,000 K. The strong emission lines defining the WR spectra originate in these optically-thick winds, which can have terminal velocities from 400-5000 km s⁻¹ (van der Hucht 2001). After spending roughly 10% of their total lifetime as a WR star (Meynet & Maeder 2005; Rosslowe & Crowther 2015, for ~ 0.25 -0.5 Myr;), WR stars are commonly described to “live fast, die hard” because, in addition to their extreme mass loss, they quickly end their lives in ~ 3 -5 Myr (Groh et al. 2014) as supernova (SN) explosions and possibly gamma ray bursts (Leloudas et al. 2010).



Fig. 1.2.— An *Hubble Space Telescope* image capturing the explosive mass loss nebular of the WR star WR 124. This image showcases the spectacular result of the stellar winds ejecting material, and the star can be seen glowing in the center. Credit: ESA/Hubble & NASA. Acknowledgement: Judy Schmidt.

1.1.2 The Spectra and Subtypes of WR Stars

While WR stars are commonly referred to as an evolutionary phase of O-stars, it is important to note that the WR classification is actually a spectroscopic phase from

which we infer an evolutionary phase. The difference is explained by Groh et al. (2014) such that this is the spectral appearance of a star, which is determined by the surface and wind properties, versus the state of the stellar interior, which is set by nuclear burning stages and stellar structure. This distinction is critical for accurate discussion between stellar evolution theorists and observers, but is often dismissed because many of the WR spectral features reflect nuclear burning products.

As stated above, much of the WR emission arises in the stellar wind, which is dense enough to become optically thick, and results in spectroscopically identifiable, broad emission lines. Thus, the classification of WR stars is based on these features, rather than on stellar parameters such as effective temperature (van der Hucht 2001). In general, WR stars are classified beyond WN and WC subtypes by using line strengths and line ratios according to Crowther (2007). Stars with N III-V and He I-II are labeled WN1-WN9. WC stars are classified based on C III-IV and O III-V lines as WC4-WC9, and also include an extension of this subtype with enhanced O lines that are called WO stars. WO stars range from WO1 - WO4 based on O V-VI and C IV lines. Additionally, the hotter stars are described as early “E”, such that WNE include WN1-WN5 and WCE include WC4-6, and the cooler stars are as late “L” and include the remaining subtypes (Crowther 2007). Example spectra and their classifications are shown in Figure 1.3.

Rather than the classic evolved helium-burning WR stars, the hydrogen-rich WN stars (WNh) and extreme Of stars (Of/WN stars) are thought to be an extension of the upper main sequence (Smith & Conti 2008; Crowther & Walborn 2011). Their spectra can include hydrogen emission and absorption lines (more similar to Of stars than WN stars) but exhibit WR emission lines as well. They are extremely massive, $>65 M_{\odot}$ (Langer et al. 1994; Crowther et al. 1995), with strong mass loss that results in the WR phenomena.

1.1.3 Understanding the Evolution of Classical WR Stars

A massive star changes spectral classifications, and thus subtypes of WR stars, as it evolves through the Conti Scenario. The most basic evolutionary path is described

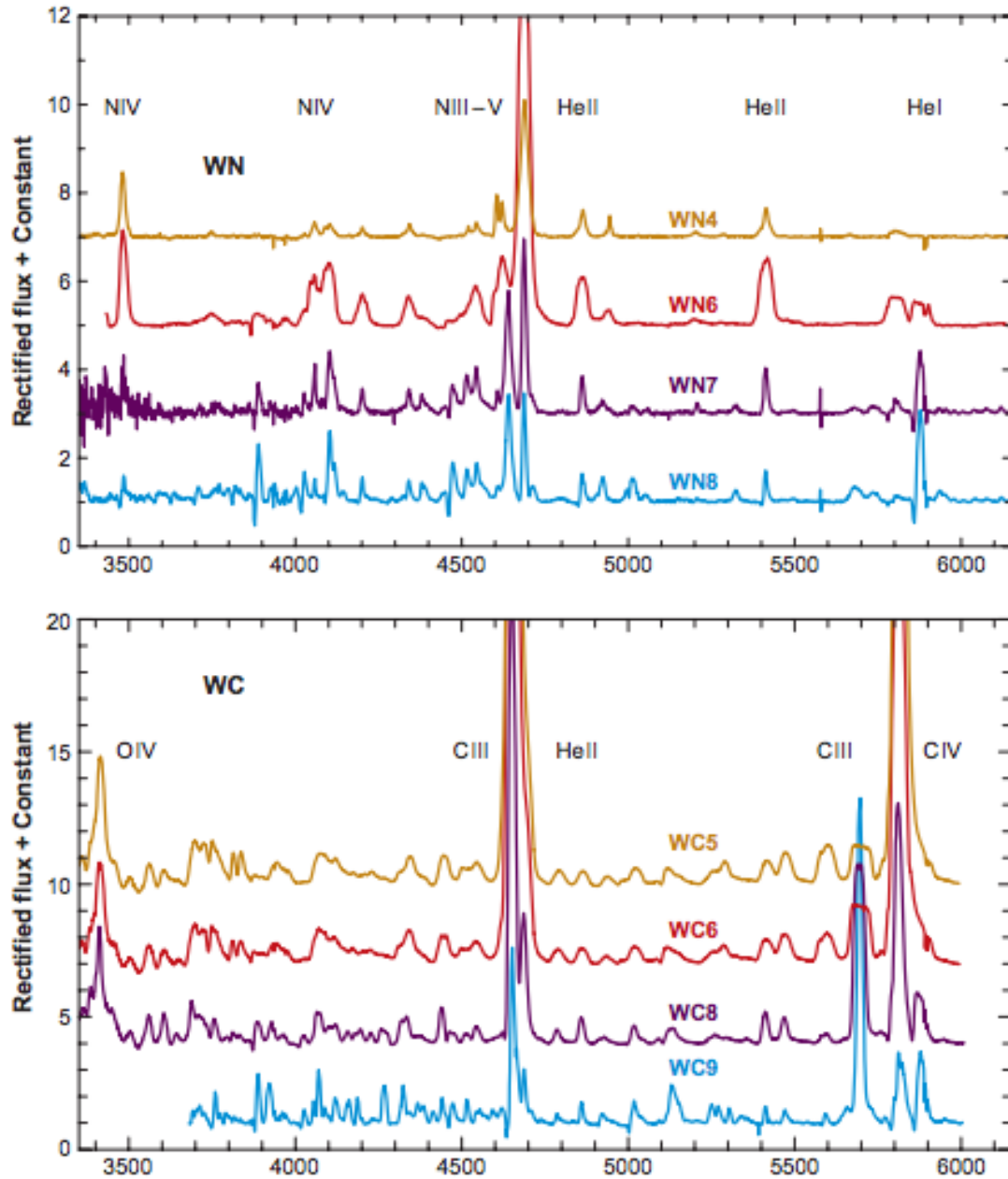


Fig. 1.3.— A view of the characteristic emission lines in WR spectra. From Crowther (2007), optical spectroscopy of WR stars in the Milky Way, in which the variations in line strengths between different WR subtypes are clear. The most well known line featured in the spectra of WN stars is He II 4686 \AA and for WC stars, C IV at 5808 \AA .

by simply peeling off stellar layers in order of chemical complexity, such as O \rightarrow luminous blue variable (LBV) \rightarrow WN \rightarrow WC \rightarrow WR \rightarrow SN Ib/c or, for a much less massive star, as O \rightarrow red super giant (RSG) \rightarrow WN \rightarrow SN Ib/c. This basic evolution of an O-star is depicted in the cartoon in Figure 1.4. In reality, the evolution can be more complex; this process is heavily dependent on mass and metallicity. The various evolutionary paths due to different initial masses can be followed in Figure 1.5, which shows the Geneva evolutionary models. A more detailed evolution for a specific case study is described by Groh et al. (2014). By modeling a non-rotating 60 M_{\odot} star and produced its spectrum throughout its lifetime, the star evolves as follows: *O3 I (at the ZAMS), O4 I (middle of the H-core burning phase), B supergiant (BSG), B hypergiant (BHG), hot luminous blue variable (LBV; end of H-core burning), cool LBV (H-shell burning through the beginning of the He-core burning phase), rapid evolution through late WN and early WN, early WC (middle of He-core burning), and WO (end of He-core burning until core collapse)* (Groh et al. 2014). Thus:

O3 I \rightarrow O4 I \rightarrow BSG \rightarrow BHG \rightarrow LBV \rightarrow WNL \rightarrow WNE \rightarrow WC \rightarrow WO.

The metallicity is key as mass loss, convection, and mixing in radiative zones are integral to the evolution (Meynet et al. 2016). Mass loss becomes less efficient and the winds are weaker at lower metallicities (Vink et al. 2001; Eldridge & Vink 2006), and thus it is more difficult for a massive star to produce a WR star at low metallicity than at high metallicity. This also means that the minimum initial mass of an O-star required to produce a WR star similarly increases, examples are given in Table 1.1.

Additionally, WR stars can also form from binary systems, which trigger mass loss through mass transfer (Georgy et al. 2012). This formation channel may thus produce WR stars from a lower initial mass star; a WR star could be produced instead of an RSG, as in the case of an 15-20 M_{\odot} star in a close binary (Georgy et al. 2015). The number of WR stars formed from a binary would also be relatively insensitive to metallicity as well. Thus at lower metallicities, many of the WR stars are produced from the binary channel. This formation channel is somewhat observationally supported; the newest survey of the WR star populations in the Milky Way estimates the duration of the WR phase is consistent with that predicted from a mix of single non-rotating stars and binaries (Rosslowe & Crowther 2015).

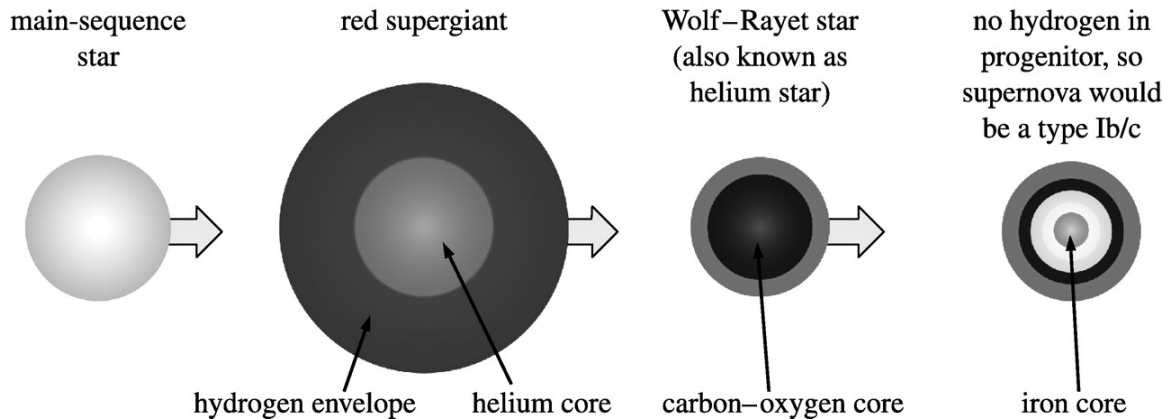


Fig. 1.4.— A cartoon from Eldridge (2008) depicting the life cycle and structure of a massive star from the main sequence through the stages of a RSG, WR, and eventual supernova as a Type Ib/c.

As for their deaths, WR stars have long been thought to be the progenitors of core-collapse SN, Type Ib and Type Ic, although this has been observationally difficult to prove; only a few candidate SN progenitors that may be WR stars have been identified (Corsi et al. 2012; Cao et al. 2013). Recent observations found an WR-like progenitor through spectral observations of the wind (Gal-Yam et al. 2014), although this is often disputed. Yet, the observed lack of clearly detected WR progenitors over the last 15 years statistically suggests that WR stars may not, in fact, be SN progenitors. We have no clear cases (only upper limits and a couple of candidates) where a WR star was a progenitor to a SN (Smartt 2015); there is a probability of roughly 0% of

Table 1.1. Initial Stellar Mass

	O-star	WNL	WNE	WC
Solar	15.8 M_{\odot}	20.0 M_{\odot}	25.3 M_{\odot}	27.0 M_{\odot}
LMC	14.2 M_{\odot}	32.1 M_{\odot}	60.8 M_{\odot}	63.1 M_{\odot}
SMC	12.6 M_{\odot}	53.5 M_{\odot}	–	–

Note. — This table lists the minimal initial stellar mass of a star for it to be able to enter a given WR phase, which varies with metallicity, as predicted from the most recent evolutionary tracks (from Georgy et al. 2015).

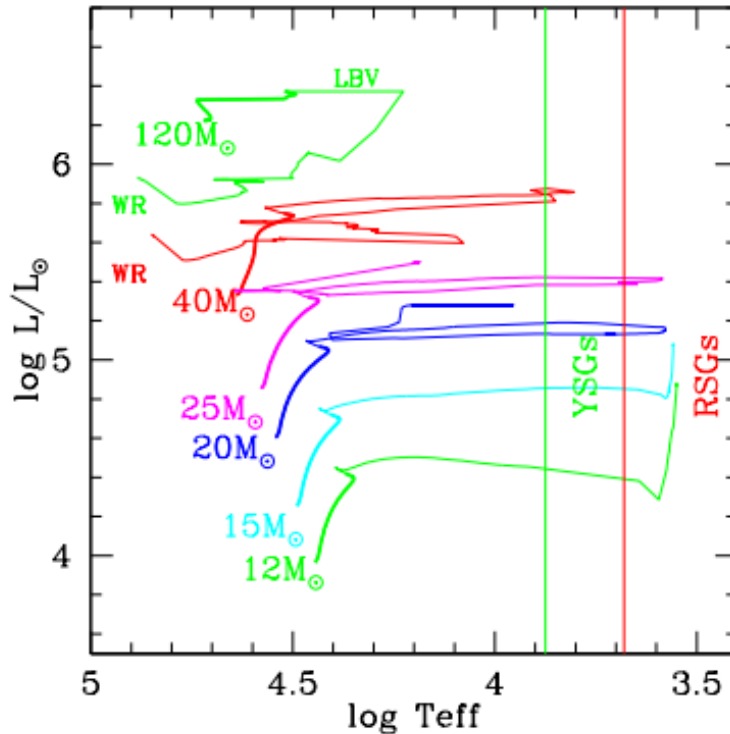


Fig. 1.5.— Figure 1 from Massey (2013) showing the evolution of massive stars by plotting the Geneva evolutionary tracks (Ekström et al. 2012) at solar metallicity. The main sequence is shown in bold, and the YSG and RSG regions are marked. Regardless of initial stellar mass, the evolution after the main sequence is relatively flat, except for the most massive stars.

this lack of evidence, if we expect that WR stars should explode as SN. These non-conclusive results may suggest that these SNe are produced instead by a population of less massive binary systems (Eldridge et al. 2013), or if the progenitors are WR stars, that the WR stars become too dim at core-collapse or produce failed SNe and instead form black holes (Smartt 2015). However, much work on this topic clearly remains, and the supernovae resulting from WR stars have not yet been conclusively ruled out. Additionally, WR stars may also be the progenitors of long-duration, soft gamma ray bursts (Woosley & Bloom 2006; Leloudas et al. 2010). As such, recent observational surveys (e.g. Crowther & Bibby 2009) hope to pinpoint enough WR stars in other galaxies that eventually one will SNe within our lifetime.

Because WR stars are stellar physics laboratories, are located in massive star forming regions, produce stellar feedback that can alter surrounding environments, and possibly end their lives with fantastic death throes, WR stars are extremely useful objects to study across many fields of astronomy. Yet, they are rather rare due to their short lifespans. Only hundreds of WR stars have been catalogued in the Milky Way. The VII Catalogue had an inventory of 227 galactic WR stars (van der Hucht 2001). Since then, and including new techniques at near-IR wavelengths, the number of known WR stars has increased to 635 since March 2014 (Rosslowe & Crowther 2015). If we extrapolate how many WR stars there should be within the entire Milky Way, there could be 1,000 (Rosslowe & Crowther 2015) to 6,000 stars (van der Hucht 2001), which is, regardless, an extremely low percentage of the total stellar content. However, the number of individual detections of WR stars in other star forming galaxies, such as in M31 by Neugent et al. (2012) increases steadily. Moreover, some extragalactic star clusters, specifically those called massive star clusters and super star clusters, host hundreds of WR stars in a single, densely packed region – increasing the potential impact of the WR stars and thus their importance.

1.2 Massive and Super Star Clusters

1.2.1 The Discovery of Bright, Blue, Compact Extragalactic Star Clusters

The star clusters in the Milky Way are found in two rather distinct forms: young, blue open clusters that are made up of a handful of stars or old, red, and spherical globular clusters that are much more massive. Yet, early observations of other galaxies did not suggest the same two populations. Instead it was found that star clusters in the Magellanic Clouds showed differences compared to these MW clusters (Hodge 1961), and a handful of blue, unresolved clusters detected in additional galaxies were also found to be much brighter than the Galactic open clusters. Because the brightest objects are the easiest to detect, the brightest clusters, and therefore the most massive and young, were first identified. The young populous clusters observed

in the Magellanic Clouds include even today’s best known example of a bright, blue cluster as 30 Doradus. Attributing the color to the youth and the unresolved nature to compactness, it was suggested that the clusters could be progenitors to objects like the MW’s globular clusters. Therefore, these rich, blue, luminous clusters came to be described by a wide variety of names: circular globulars, young globulars, blue globulars, and the adopted “young populous clusters” (Hodge 1961); super associations (e.g., Wray & de Vaucouleurs 1980); young blue clusters and bluish knots (van den Bergh 1981); superluminous young star clusters (Arp & Sandage 1985); and super star clusters (Arp & Sandage 1985; Melnick et al. 1985). By ruling out potentially incorrect distances to foreground stars as a possible alternative explanation, the extreme luminosities of the “super star clusters” in NGC 1705 by Melnick et al. (1985) and NGC 1569 by Arp & Sandage (1985) were verified, along with the super star cluster (SSC) nomenclature.

Although rare in the local universe, these luminous clusters were revealed in a variety of environments, from local group galaxies (such as M33 or NGC 1613 for example, Melnick & D’Odorico 1978; Sandage & Katem 1976), late type galaxies (Wray & de Vaucouleurs 1980), starburst galaxies (e.g. M82 and NGC 1569; van den Bergh 1981; Arp & Sandage 1985), to mergers (such as NGC 3597 by Lutz 1991). Possibly the most important pre-*Hubble Space Telescope* (*HST*) observation of a population of SSCs was of the “luminous blue clusters,” whose mass and luminosity truly rivaled that of globular clusters, observed in the merger remnant galaxy NGC 3597 (Lutz 1991), shown in Figure 1.6. These observations suggested that such star clusters may form as a result of the galaxy merging process. However, the poor angular resolution of ground-based telescope paired with the compactness of the SSCs severely limited further investigation of this mode of star formation (O’Connell et al. 1994).

With the launch of *HST*, new stunning images with superior angular resolution showed that SSCs could be found in huge numbers beyond the local group, and were so widespread that they became known as a cluster class (Ho 1997). Even with aberrations before the servicing mission, Holtzman et al. (1992) discovered ~ 60 blue, point like objects in *HST* observations of NGC 1275, a peculiar merging galaxy,

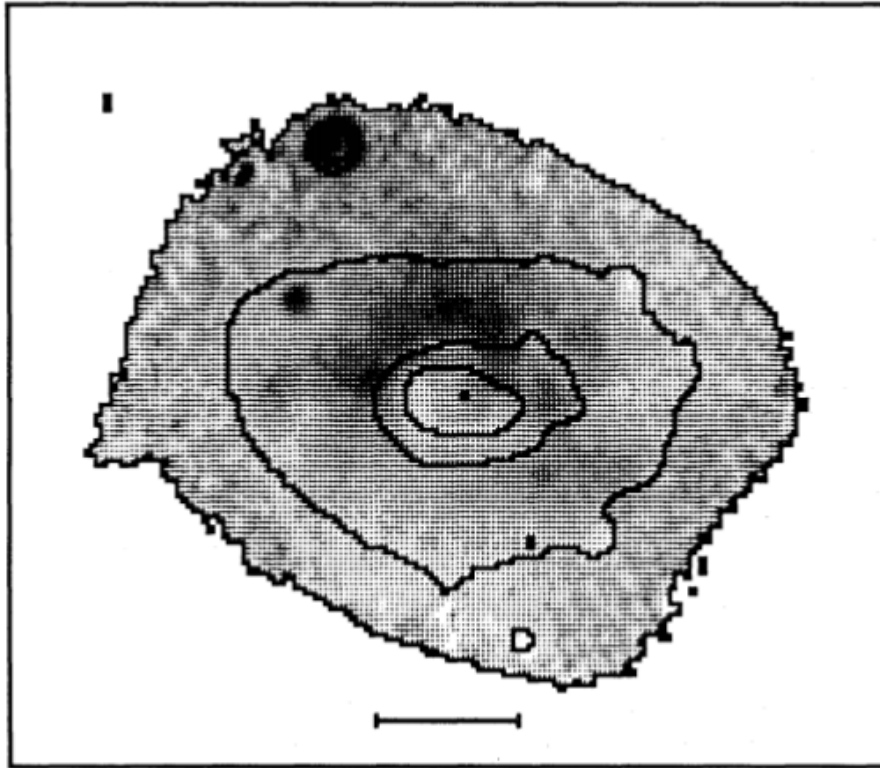


Fig. 1.6.— A grey scale color map (B-V) of the merger remnant NGC 3597. The scale bar is $10''$ and B-band contours are over plotted. The star forming regions are derived from this map, and are clearly unresolved, yet their properties were consistent with young globular clusters. From Lutz (1991).

which became a “catalyst in this active new field” to search for young globular clusters (Whitmore 1999). Whitmore et al. (1993) discovered similar populations in the prototypical merger remnant NGC 7252, whose isolation provided a clearer indication that these clusters might form in merging galaxies (Whitmore 1999). Then, further bright, blue, point-like objects were revealed in star-forming dwarf galaxies NGC 1140 (Hunter et al. 1994), NGC 1569 and NGC 1705 (O’Connell et al. 1994), M 82 (O’Connell et al. 1995), NGC 253 (Watson et al. 1996), as well as in circumnuclear star forming rings (e.g., Benedict et al. 1993; Barth et al. 1996). The common element of the environments in which these discoveries were made is high star formation, suggesting that massive star clusters pinpoint extreme star formation events (Hunter et al. 1994; Whitmore 2003). The richest collection to date of identified SSCs was

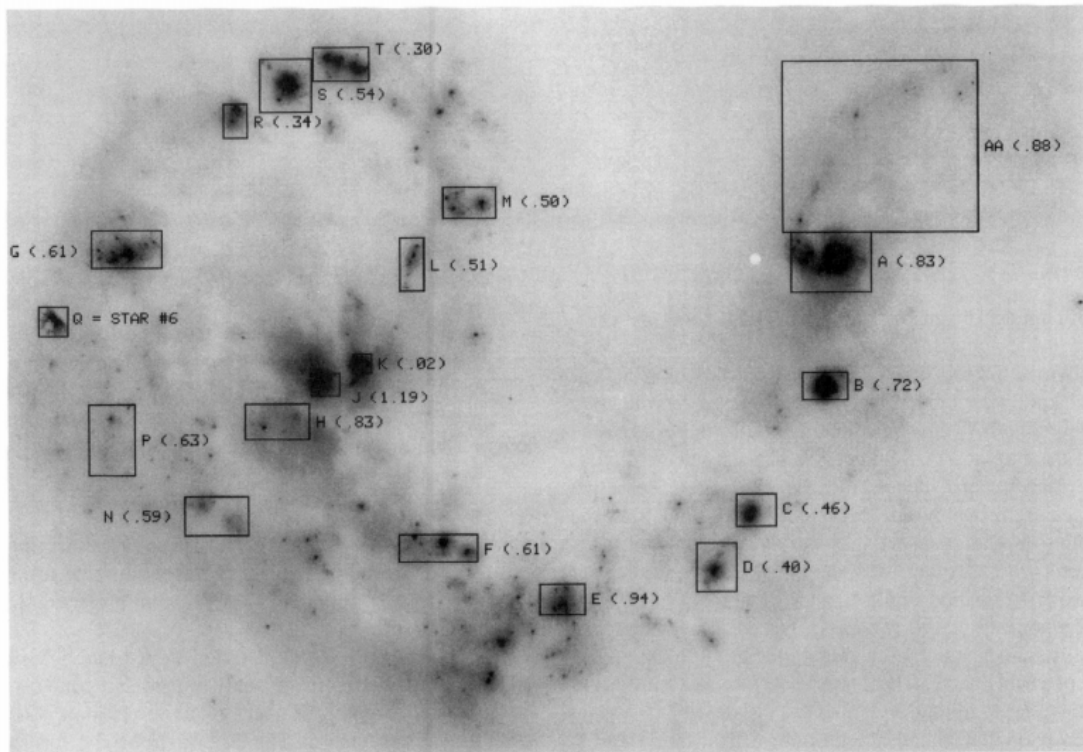


Fig. 1.7.— A Wide Field Camera image of the Antennae galaxy, observed before the *HST* servicing mission, from Whitmore & Schweizer (1995). The Antennae host the richest collection of SSC’s that is known: other than a few foreground stars, each point-like object is a star cluster. The boxes denote star formation knots from an early study by Rubin et al. (1970), identified by letters and with the mean color index V-I in parenthesis. This image features the benefits of high resolution (even with aberration) in contributing to the new “discovery” of SSCs by *HST*.

found with pre-refurbishment *HST* observations by Whitmore & Schweizer (1995) of the merging Antennae Galaxy (NGC 4038/4039), discovering over 700 bright, young, barely resolved clusters that became the most compelling evidence that globular clusters can form during gas-rich mergers (Whitmore & Schweizer 1995). An image of the overlap region of the Antennae from the pre-refurbishment *HST* observations is shown in Figure 1.7, and an incredible comparison image taken with the current *HST* capabilities is shown in Figure 1.8.

Since these early discoveries that showed the potential for wealth of star clusters in starbursts and mergers, almost every gas-rich merger observed with *HST* has revealed



Fig. 1.8.— A stunning modern view of the Antennae galaxy, imaged by the Advanced Camera for Surveys (ACS) on *HST*. Compared to the *HST* image before the servicing mission in Figure 1.7 –upon which much interest for this field was based– it is amazing to see not only how small the SSCs are when they are better resolved, but also how many more become distinct. Credit: B. Whitmore, NASA, ESA, and the Hubble Heritage Team (STScI/AURA)-ESA/Hubble Collaboration.

similar star clusters (Whitmore 1999) and furthermore, SSCs have also been found in a wide variety of environments. An UV snapshot survey confirmed the connection of these clusters to star formation, finding them even in normal disc galaxies (Ho

1997; Larsen & Richtler 2000), indicating that compact clusters are common amongst regions with elevated star formation rather than only extreme starbursts (Ho 1997; Whitmore 1999). In fact, young star clusters represent not only a tell-tale sign of vigorous star formation; most, if not all, stars may form in clusters (Lada & Lada 2003) – although most will not stay bound or survive (Fall 2004) and that star formation in clusters could be the dominant mode of star formation in galaxy interactions (Ho 1997; de Grijs 2004).

1.2.2 Terminology: Massive Star Clusters versus Super Star Clusters

When multitudes of young massive star clusters were found, it became clear that these clusters appear to follow a continuous mass distribution. In general, the cluster luminosity function and mass function can be described by a power law with an index of -2, though there might be an exponential truncation at $10^5 M_{\odot}$ in quiescent galaxies and $10^6 M_{\odot}$ in starbursts (Portegies Zwart et al. 2010). Figure 1.9 shows the cluster mass distribution in different galaxies. However, this power law distribution contrasts the luminosity function of globular clusters, possibly muddling their evolutionary connection – this will be discussed in Section 1.2.4. The luminosity function of globular clusters is instead consistent with a Gaussian (Whitmore 1999). This difference may indicate that the fainter, diffuse clusters get destroyed (Whitmore 1999), and therefore many of the less massive star clusters do not contribute to the observed luminosity function of globular clusters, although may have been present in the cluster initial mass function.

As there is a continuum of cluster masses, the terminology regarding these objects has become rather vague and varied. Portegies Zwart et al. (2010) emphasize the important characteristics of these star clusters are that they are young, dense, and massive; however, a meaningful definition of a “massive star cluster” is as subjective as that of a “normal” galaxy (Larsen 2004). It has become rather fashionable to call all of these bright, blue clusters Young Massive Clusters (YMCs); they can simply be more massive than open clusters in the Milky Way (Larsen 2004). Galliano et al. (2008)

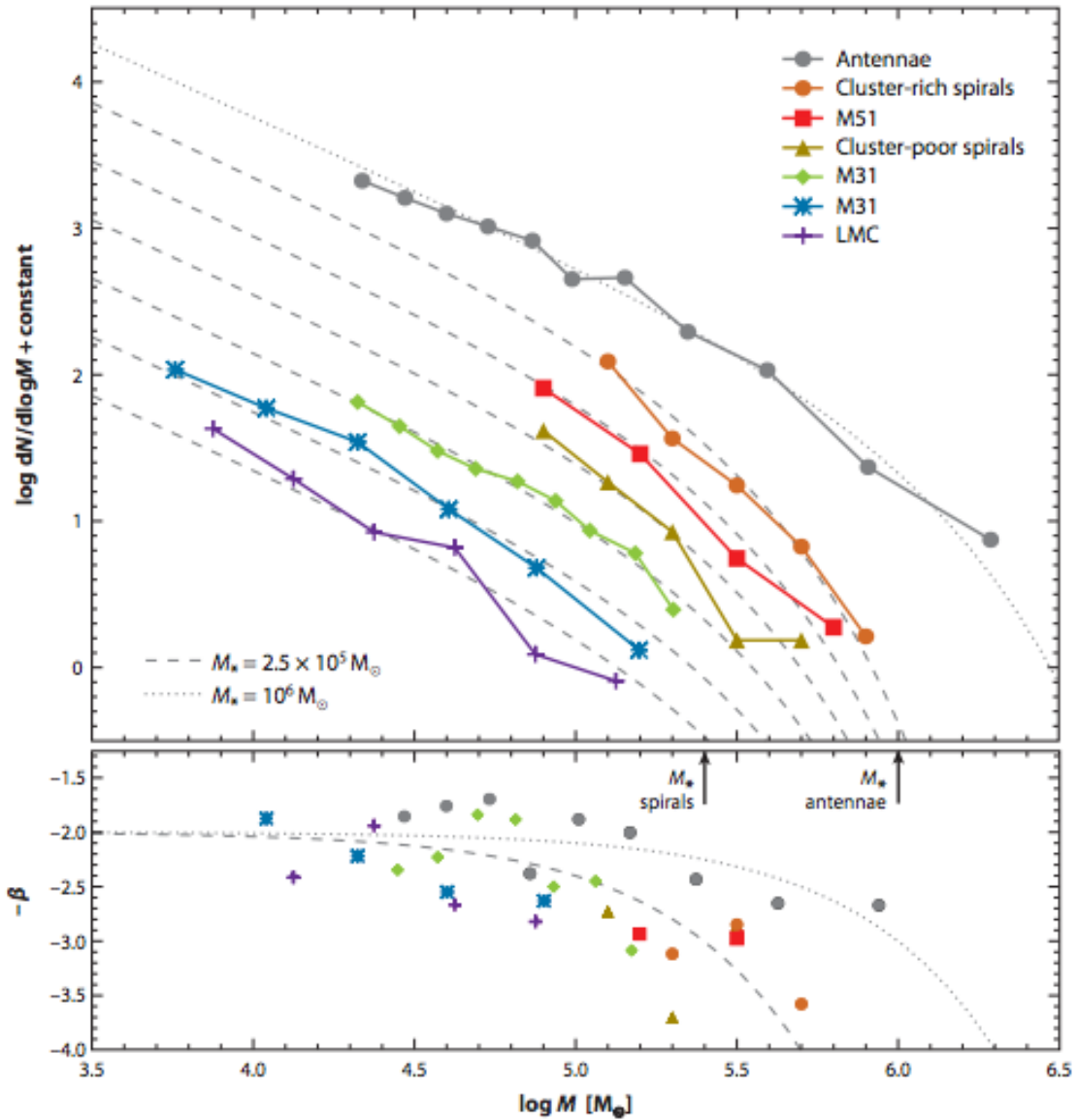


Fig. 1.9.— A plot from Portegies Zwart et al. (2010) that clearly displays the mass function of young clusters (< 1 Gyr) in various galaxies. The dotted and dashed curves represent a Schechter function with a turnover mass M_* as indicated, which may depend on galactic environment. As the general shape of the mass function is a power law, the distinction between massive star clusters and SSCs is somewhat arbitrary.

uses YMC for clusters that are more massive than $10^5 M_\odot$, have radii smaller than 5 pc, and younger than 100 Myr. Broadly, Portegies Zwart et al. (2010) concentrate

on clusters with ages below 100 Myr and masses above $>10^4 M_{\odot}$. Ho (1997) includes clusters that have ages less than a few hundred Myr, radii less than a few parsecs, and masses ranging from $10^4 M_{\odot}$ - $10^6 M_{\odot}$.

More dramatic, the term “super star cluster” originates due to their very high luminosities, and is often reserved for the most extreme massive star clusters. Some specific definitions for this term include: diameters less than 50pc and luminosities such that $M_v \leq -10$ (O’Connell et al. 1994) or luminosities of one to two magnitudes higher than R136 (Ho 1997). Yet ultimately, Galliano et al. (2008) states a preference for the more generic YMC, because SSC can imply that a cluster is visible in the optical (due to the origin of the name) and thus may not translate well to earlier evolutionary stages when a cluster is still embedded in birth material. For the purposes of this work and from here on out, we use the generic term “massive star cluster” to refer all star clusters of $>10^{3-4} M_{\odot}$, regardless of age. We adopt a definition of “super star cluster” for any massive star cluster above an arbitrary minimum mass of 10^5 or $10^6 M_{\odot}$. We do not associate an evolutionary stage with the use of the term “massive star cluster.”

1.2.3 The Evolution of Massive Star Clusters

A picture of massive star cluster evolution has developed in which massive star clusters form in thick, dense envelopes of natal material similar to vastly scaled up versions of single massive stars (Johnson 2002), depicted in Figure 1.10 as a cartoon. The evolution of a massive star cluster starts with the collapse of a massive ($\gtrsim 10^{5-6} M_{\odot}$) molecular cloud, subsequently forming hundreds to thousands of massive stars. Yet these stars form embedded in the natal cocoon, and the early evolution of the cluster is effectively obscured from view at many wavelengths. However, the massive stars within the embedded cluster begin to ionize the surrounding material, making the cluster first observable with radio wavelengths that can pierce through the cocoon to detect the thermal free-free emission arising from ionized gas (e.g., Kobulnicky & Johnson 1999; Turner et al. 2000). A number of these analogs to Ultra-Compact H II (UCH II) regions have been identified in other galaxies (e.g. Kobulnicky &

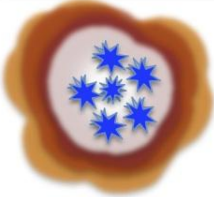
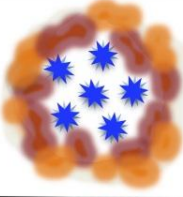
Evolutionary State		Observable Wavelengths
Proto Cluster		Millimeter - Infrared
Natal Cluster		Radio - Infrared
Emerging Cluster		Infrared - Optical
Adolescent Cluster		Ultraviolet - Infrared

Fig. 1.10.— A cartoon diagram of the evolution of massive star clusters from K.E. Johnson, depicting the expected similarities of the evolutionary stages of a single massive star to that of the massive star clusters.

Johnson 1999; Turner et al. 2000; Johnson & Kobulnicky 2003; Johnson et al. 2004; Tsai et al. 2006; Reines et al. 2008; Johnson et al. 2009; Tsai et al. 2009; Aversa et al. 2011; Kepley et al. 2014) with a flat or inverted spectral index, indicative of the thermal free-free emission from dense young H II regions. Kobulnicky & Johnson (1999) dubbed these sources as Ultra-Dense H II regions (UDH IIs) (or similarly “supernebulae” by Turner et al. 2000).

The massive stars, hidden in these cocoons, will continue to evolve and proceed to evacuate the surrounding material. One possible example of this emerging evolutionary stage are emission line clusters (ELC). Identified in the Antennae galaxies,

ELCs are a type of H II region that are young versions of SSCs and exhibit broadened Br γ line emission suggestive of massive stars evacuating their surroundings via wind (Gilbert & Graham 2007). Finally, the massive stars will clear enough natal material away to reveal the star cluster at optical wavelengths, by which time further star formation has been halted (Agertz et al. 2013). This results in the final early evolutionary stage as the bright and blue optical clusters that were originally identified as SSCs. The entire massive/super star cluster evolutionary sequence can be summarized as: protocluster \rightarrow UDH II \rightarrow emerging cluster (ELC) \rightarrow YMC/SSC (e.g. Whitmore et al. 2014).

A descriptive, multi wavelength classification scheme for the early evolution of massive star clusters has been developed by Whitmore et al. (2014) using CO, radio, optical/near-IR continuum, and optical/near-IR line emission observational criteria, which we quote below:

- *Stage 0 (diffuse giant molecular clouds) [turbulent equilibrium] – Knots of diffuse CO emission are detected, but no radio or optical/near-IR emission is observed. These regions generally appear as dark regions of dust in optical images.*
- *Stage 1 (protocluster, <0.1 Myr) [high pressure, gravitational collapse] – Compact CO emission is detected, but no radio or optical/near-IR emission is observed. This stage is expected to be very short lived (i.e., <0.1 Myr) and hence it is very rarely observed.*
- *Stage 2 (embedded cluster, 0.1–1 Myr) [onset of star formation] – Thermal radio emission is detected along with CO emission. No optical/near-IR continuum is observed, but weak line emission may be present if an O star has formed. Low mass clusters may never form an O star (i.e., due to stochasticity; see Fouesneau & Lançon 2010). The very recently formed cluster is deeply embedded in its natal gas during this stage.*
- *Stage 3 (emerging cluster, 1–3 Myr) [removal of gas and dust] – The very young cluster is observed primarily in the radio, optical/near-IR emission lines, and faintly in the optical continuum. There may still be weak CO associated with*

the object, but in many cases the CO is from an adjoining GMC or protocluster. The cluster is moderately extinguished by dust, with A_V typically 1 mag.

- *Stage 4 (young cluster, 3 Myr–10 Myr) [ISM feedback] – The cluster is increasingly observable in the optical and in optical/ near-IR emission lines (the latter typically in the form of bubbles), due to the removal of much of the natal gas and dust by feedback. CO emission is gone, but weak radio continuum emission is still observed in many cases. The A_V values have dropped to <1 mag.*
- *Stage 5 (intermediate/old clusters, >10 Myr) [spectral dimming, evaporation] – The cluster is observed in the optical/near-IR, although it has faded, and ionized gas is no longer observed because the massive stars have evolved into stellar remnants. The cluster slowly loses stars due to two-body encounters (i.e., evaporation; see also Fall & Chandar (2012) for a discussion of various other star cluster destruction processes).*

1.2.4 Fate: Globular Cluster or Dissipation?

After a massive star cluster has evolved through the stages presented above, their fate is thought either to become a globular cluster, or to be destroyed by becoming unbound. Since their discovery, SSCs were thought to represent analogs to young globular clusters, and possibly actually evolve into globular clusters – this fate is quite important as it suggests that globular clusters could still be forming today and not only in the early Universe (e.g., Ho 1997; Larsen & Richtler 2000; Johnson 2002; Portegies Zwart et al. 2010). If the most important qualification for a star cluster to be considered as a globular cluster is that it is massive and compact, then massive star clusters in the early universe are their “logical” progenitors (Portegies Zwart et al. 2010). Because protoglobular clusters in the early universe are unobservable, this connection offers an exciting opportunity to understand the formation and evolution of globular clusters.

Yet, there remain unknowns and it has become clear that not all massive star clusters evolve into globular cluster-like objects. The first concern was that massive

star clusters and globular clusters may not even be related. As mentioned in Section 1.2.2, the power law luminosity distribution of massive star clusters is different from the luminosity distribution of globular clusters, which is instead consistent with a Gaussian (Whitmore 1999). This was actually interpreted early on to suggest that there is no connection between massive star clusters and globular clusters (van den Bergh 1995). However, rather than suggesting that these objects are inherently different, it is now believed that the distinct luminosity distributions may indicate the effects of physical processes. For instance, one possibility is that the fainter, diffuse clusters get destroyed (Whitmore 1999). In this case, even if the cluster initial mass function follows a power law mass distribution, fewer lower massive star clusters will survive and become globular clusters, and thus will not contribute to the observed luminosity function of globular clusters (producing a Gaussian instead).

Some evidence that destruction processes are at work is seen with an observed disparity between forming and older cluster populations. Lada & Lada (1991, 2003) identified that the birth rate of star clusters (embedded clusters) exceeds the population of older star clusters in the MW, and this disagreement has similarly been observed in other galaxies as well (Chandar et al. 2010). This was interpreted as “infant mortality,” thought to be caused by disruption of the star cluster during the early gas expulsion phase (Lada & Lada 2003), although cluster destruction can later be caused by several other mechanisms as well, such as two-body relaxation and tidal shocks (Gnedin & Ostriker 1997). Infant mortality is caused by stellar feedback removing the ISM, and often includes violent relaxation due to this mass loss, is expected during cluster ages < 10 Myr. Stellar feedback may continue to cause some cluster destruction until $\sim 10^8$ yr, then tidal disturbances $> 10^8$ yr, and ultimately two body relaxation (also called evaporation) will dominantly cause disruption on long timescales, on the order of a Hubble time (Fall et al. 2009). The early disruption processes are particularly intriguing, as if the cluster is not immediately destroyed, they will weaken the ability of a cluster to stay bound – impacting the cluster beyond the young 10 Myr timescale (Gnedin & Ostriker 1997).

While it is clear that there are many cluster disruption mechanisms in place, solving the luminosity distribution puzzle remains elusive. One debate is the extent to

which any of the cluster disruption processes, or combination thereof, have a mass dependence sufficient to explain this (Gnedin & Ostriker 1997; Fall et al. 2009; Bastian et al. 2012). Mass dependent processes can explain the change in luminosity distribution from an initial power law to the ultimate Gaussian, although Fall et al. (2009) claim evaporation is sufficient to produce this result. Even in this explanation, it is apparent that the timescales of the destruction are not understood. A major wrinkle in the entire debate is that the evidence is predominately based on luminosity distributions, and as luminosity does not directly translate to mass, but also depends strongly on age, the assumptions in binning and the sample selection will clearly impact the results. For instance, studies using the same dataset in the SMC have resulted in opposing conclusions in regard to the mass dependence (Chandar et al. 2006; Gieles et al. 2007). Another real possibility is that many of the young massive star “clusters” could be actually unbound associations instead (and thus the initial power law may not include only bound objects Bastian et al. 2012). In the same way, if distributions are weighted averages over all time frames, masses, and states of being bound, one would expect a power law (thus dissimilar to the log-normal mass function of globular clusters). Yet ultimately, whether the population of the massive star clusters that survive is determined by infant mortality, other later processes, or the extent to which a young cluster is gravitationally bound, only a small fraction (1-10%) of massive star clusters will remain bound on long timescales (Fall et al. 2009). One of the biggest remaining questions in this field is what fraction will become globular clusters (i.e., what fraction survive Whitmore 1999).

1.3 Feedback

1.3.1 The Feedback Mechanisms

As mentioned above in Section 1.2.3, star clusters evolve from embedded protoclusters to the well-studied optical star clusters as young stars inject energy and momentum – a process called feedback, which is what is responsible for the early evolution of the massive star clusters and altering their natal cocoon. Feedback will form an

H II region, drive the dynamics of the resulting H II region (e.g., Krumholz & Matzner 2009; Lopez et al. 2014), and eventually evacuate the natal material through many different physical processes and mechanisms.

The energy from photons emitted from the stars is conserved as it interacts with surrounding material. The photon’s energy can ionize atoms; any remaining energy that doesn’t escape will heat the gas. The blue light ($\lambda < 512 \text{ \AA}$) from massive stars has enough energy to ionize atoms, particularly hydrogen atoms (these have an ionization energy threshold of 13.6 eV). Thus, H II regions are produced as soon as massive stars in the process of forming start emitting light, and thus begin to ionize and heat the surrounding material. The heated ionized gas composing the H II region is in contrast with the surrounding cold material, creating a pressure imbalance. This pressure from the warm ionized gas causes an acceleration outward, resulting in an expansion of the H II bubble (Dale et al. 2005; Walch et al. 2012; Dale et al. 2014). This feedback process is referred to broadly as “photoionization” (e.g., Sales et al. 2014), but also includes the warm ionized gas pressure (e.g., Lopez et al. 2011).

The momentum from the photons in their interactions is also conserved, so there is a net momentum transfer to the gas and dust. Thus, each atom that absorbs a photon (gets photoionized) will also experience a velocity kick. The term “radiation pressure” is then the net effect that results in a pressure force, although radiation pressure is also sometimes regarded as the energy density of the radiation field (Lopez et al. 2011), and is regardless one of the most important feedback processes (Krumholz & Matzner 2009; Fall et al. 2010; Murray et al. 2010; Lopez et al. 2011).

The stellar radiation also has the potential to be absorbed by surrounding dust and be re-radiated in the infrared. This dust-processed infrared radiation will exert a pressure determined by the energy density of the radiation field that was absorbed. Thus, the dust-processed radiation pressure can be dynamically important if the radiation is trapped inside a H II shell that is optically thick to the IR light (Krumholz & Matzner 2009; Murray et al. 2010).

Beyond emitting photons, stars also contribute feedback through outflows, jets, winds, and supernova. Supernova can considerably impact star clusters, however, the focus of this thesis will be the timeframes and feedback mechanisms that occur *before*

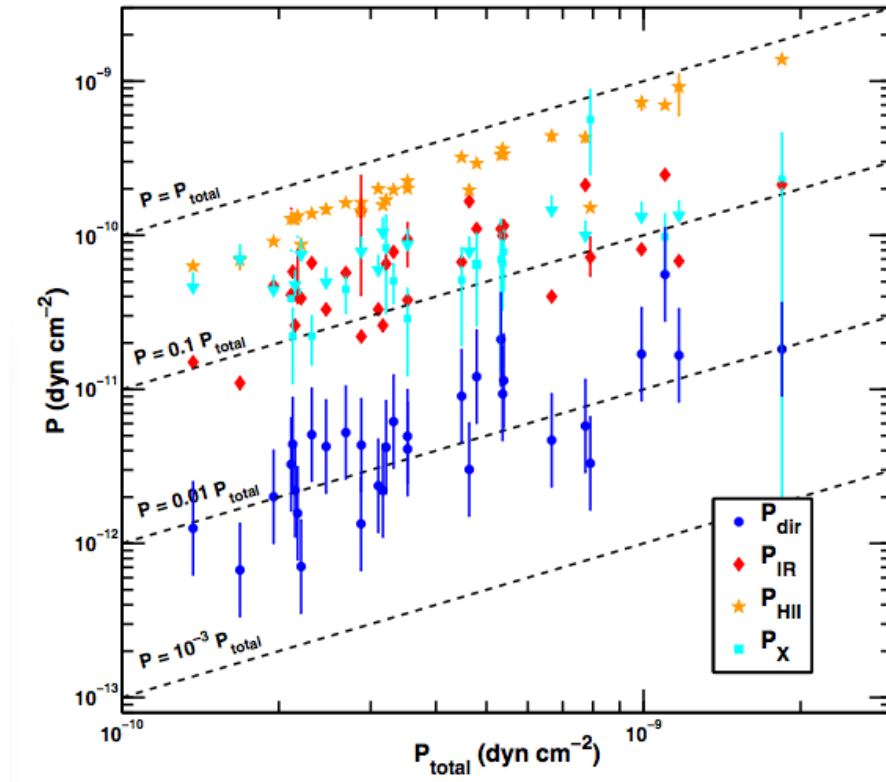


Fig. 1.11.— The dominant feedback mechanism in an observation study of massive star clusters in the LMC appears to be warm gas pressure (due to photoionization), as shown by this figure from Lopez et al. (2014), however it is suspected that radiation pressure may be more important at earlier times.

the stars explode as supernova, and are thus not considered further here. Analogously, protostellar outflows and jets from low mass stars are also omitted from consideration in this thesis. While important in low-mass star clusters (e.g., Cunningham et al. 2011), the dynamic contributions of protostellar outflows and jets are negligible at the massive star cluster scale (Matzner 2007). On the other hand, in massive star clusters where many massive stars are present, the stellar winds from the massive stars inject energy (the integrated energy is as much as from a supernova explosion), momentum, mass, and metals into their surroundings, carving out cavities (Rogers & Pittard 2013) and removing natal gas (Calura et al. 2015). In addition, shock heating from all these various processes will produce hot X-ray gas and, thus, hot gas pressure will also contribute feedback (e.g., Stevens & Hartwell 2003; Pellegrini et al. 2011;

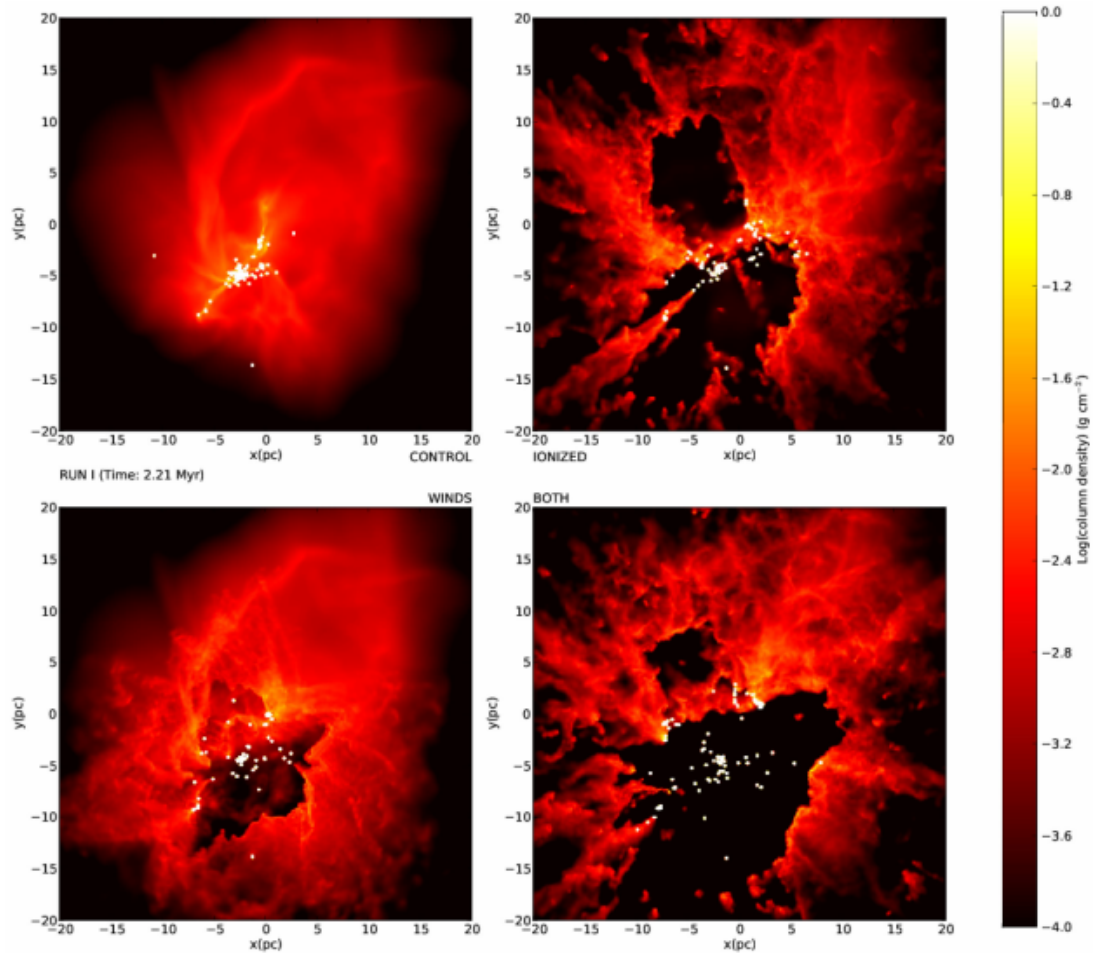


Fig. 1.12.— Various simulations from Dale et al. (2014) showing resulting morphologies of the cold natal gas of a massive star cluster that may be cleared out by feedback: (top left) control with no feedback, (top right) ionization, (bottom left) stellar winds, and (bottom right) winds and ionization.

Rogers & Pittard 2014).

In general, the relative importance of different feedback mechanisms on driving the evolution of the H II region and on the surrounding natal material is not yet understood (Lopez et al. 2011). The expansion of the ionized gas likely dominates H II regions driven by single massive stars to massive star clusters, for instance in analytic studies (e.g., Matzner 2002), simulations (e.g., Dale et al. 2005), and observational studies as shown in Figure 1.11 (in the Large Magellanic Clouds by Lopez et al. 2014). However, radiation pressure may also be the dominant feedback

mechanism early on (Krumholz & Matzner 2009; Lopez et al. 2011). The processed infrared radiation pressure is not in the running as a dominant feedback process; it is observed to be insignificant in H II regions in the LMC Lopez et al. (2011, 2014). Thus, the effects of processed infrared radiation pressure are often not included in studies; rather the “single-scattering” regime (only the direct radiation pressure considered) is often the focus of feedback studies instead (Sales et al. 2014). Stellar winds are thought to be less important energetically in the dynamics of H II regions, as the output energy equivalent to that of a supernova can leak and escape (e.g., Rogers & Pittard 2013). Yet, it is becoming increasingly clear that stellar winds should not be ignored. Winds are more efficient than the H II region pressure in removing extremely dense material and in determining the morphology (Dale et al. 2014). In addition, the impact of later supernova is increased by up to a factor of two to six, if winds have cleared molecular material (Walch & Naab 2015; Fierlinger et al. 2016). These details demonstrate that the feedback phase of massive star clusters is complicated, with different mechanisms contributing at different times and interplay between them (Sales et al. 2014). See Figure 1.12 for a visual comparison of the effects of a couple different feedback processes on a star cluster.

1.3.2 Potential for WR Stars to Increase Feedback

Thus far, the contribution of additional feedback from WR stars has not been addressed in the literature. The WR feedback may be significant in the evolution of some massive star clusters, and will be the topic of this thesis. There are good reasons to suspect that WR stars may be important in how massive star clusters emerge. The feedback from many different physical processes may be increased during the WR phase, including the two leading candidates for the dominant feedback process (photoionization and radiation pressure). There might be a slight increase in the luminosity of the stars (and thus cluster) during the WR phase for stars with certain initial masses or properties, which would produce more radiation pressure than that from O-stars, as follows. The Geneva models at solar metallicity (Ekström et al. 2012) show that non-rotating stars have a higher luminosity during the WNL

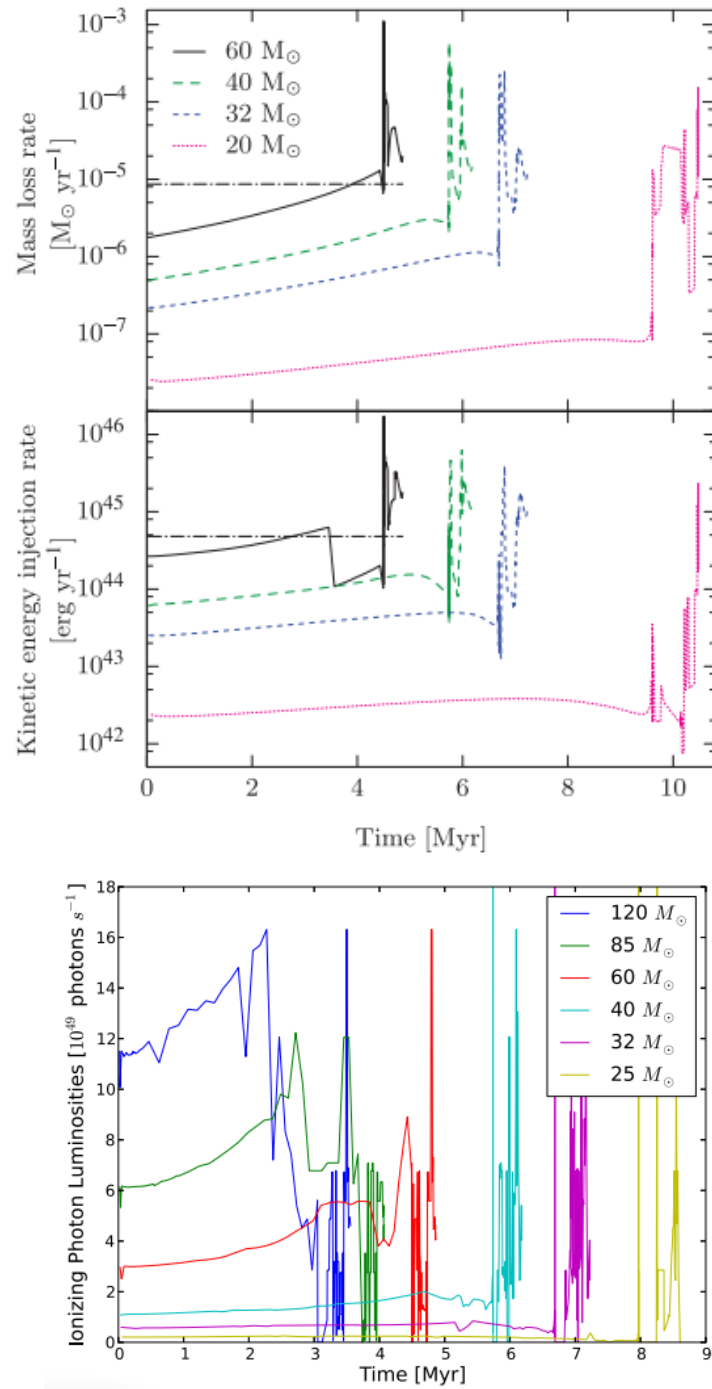


Fig. 1.13.— The increased potential for feedback is clear in the most recent stellar evolutionary codes (Ekström et al. 2012). Top: from Fierlinger et al. (2016), the mass loss and kinetic energy are shown. Bottom: from Topping & Shull (2015), the ionizing photon rates also show enhancements over the WR phase.

phase than during their O-star phase (see Figure 1 in Georgy et al. 2012). If rotating, this only follows for stars with lower initial stellar masses ($\sim 25 M_{\odot}$). At a low metallicity of $z=0.002$ (Georgy et al. 2013), where a higher initial mass is required to make a WR star through single star evolutionary paths, the stars with initial stellar masses $> 85M_{\odot}$ exhibit higher luminosities during the WR phase compared to the earlier stages. Observationally, the findings may not be in agreement with the predictions; as shown in HR diagrams, WC stars in the MW appear below the previously predicted tracks (Sander et al. 2012), and WN stars in the LMC and M31 fall across and below evolutionary tracks (Hainich et al. 2014; Sander et al. 2014). Regardless of the luminosity, the WR winds can cause chemical enrichment (Kehrig et al. 2013), leading to greater opacities and a corresponding increase in radiation pressure.

Additionally, the ionizing flux for stars with an initial mass of $60 M_{\odot}$ is increased by an order of magnitude, and more for stars with initial masses less than $60 M_{\odot}$, when they have evolved into the WR phase (at solar metallicity; Topping & Shull 2015), which is shown in Figure 1.13. Higher ionizing photon rates from WR stars can result in more photoionization in comparison to that produced by O-stars, and thus result in higher ionized gas pressure.

Lastly, the feedback potential of the winds was first realized by Abbott (1982), somewhat unexpectedly, in calculating how significant the wind power contributions from WR stars could be. For many stars, particularly those initial masses less than $60 M_{\odot}$, the wind power output during the short WR phase is more than that produced during the hydrogen burning phase when on the main-sequence. Abbott (1982) also estimated that more than half of the mass and energy input by early type stars into the nearby interstellar medium was from WR stars, which were only 5% of the studied stellar population.

However this contribution is less apparent when approximate WR properties are considered, say for stars with initial masses greater than $60 M_{\odot}$. In the generic case, WR winds will input roughly ten times the instantaneous energy than O-star winds. Then, the short lifespan of the WR stars, roughly a tenth of the O-stars' lifetime, leads to a simple calculation that the integrated energy output by the winds is similar over the lifetime of the O-stars and the WR stars; this has likely led to somewhat

ignoring the WR star contributions to the feedback. Yet as Abbott (1982) showed early on, and in the case of the other feedback processes as well, the evolution of the star for each specific initial masses matters and the output energy may be much higher (see Figure 1.13).

Most importantly, if there is an increase in feedback during the WR phase, the influence on the environment may be increased beyond that of the previous O-star phase particularly because of the carved out cavities due to the O-star feedback. In the same way that the impact of supernova is amplified if the region was previously cleared out (Agertz et al. 2013; Walch & Naab 2015) because steady feedback has been shown to be more efficient than a blast (Fierlinger et al. 2016), the impact of the WR feedback should be increased after the O-star feedback has (very slowly) done its work. Clearly, there is much work to be done to understand the interplay amongst the different feedback mechanisms (Calura et al. 2015), including the WR contributions.

1.4 Contents of This Thesis

This thesis investigates the potential role of WR stars in the early evolution of massive star clusters and is primarily composed of two in-depth works that have been published in refereed journals. Chapter 2 was published in the *Astronomical Journal* in January 2015 (Sokal et al. 2015a). After Reines et al. (2010) published observations showing WR features in a partially embedded massive star cluster S26 in NGC 4449, I infer the evolutionary significance of this seemingly surprising feature. It is clear the massive star populations, particularly the WR stars, in S26 are drastically altering enshrouding natal material and revealing the optical cluster hidden inside. With a multi-wavelength analysis of S26, I hypothesize that the contribution of feedback from WR stars may provide the tipping point in the combined feedback processes that drive a massive star cluster to emerge.

In Chapter 3, I describe an observational survey, inspired by S26 in NGC 4449, to assess the role of WR stars in the emergence of massive star clusters. The primary goal is to examine the evacuation process in action by finding more clusters in the

same evolutionary phase as S26. In addition to identifying a sample of emerging massive star clusters hosting WR stars, I find that the prevalence of the WR stars in the targeted emerging massive star clusters is an important result, as a clear detection of the WR bump is observed in 50% of the radio-selected sample. Additionally, there are key differences between the emerging massive star clusters with and without WR stars. This work is to be published by the *Astrophysical Journal* (Sokal et al. 2016). Finally, I give a brief summary and look forward in Chapter 4.

Chapter 2

An Emerging Wolf-Rayet Massive Star Cluster in NGC 4449

2.1 Overview

Here, I present a panchromatic investigation of the partially embedded, emerging massive cluster Source 26 (= S26) in NGC 4449 with optical spectra obtained at Apache Point Observatory and archival *Hubble*, *Spitzer*, and *Herschel*¹ *Space Telescope* images. First identified as a radio continuum source with a thermal component due to ionized material, the massive cluster S26 also exhibits optical Wolf-Rayet (WR) emission lines that reveal a large evolved massive star population. Using optical spectra, I find that S26 is host to ~ 240 massive stars, of which ~ 18 are WR stars; the relative populations are roughly consistent with other observed massive star-forming clusters and galaxies. Infrared SEDs of S26 extracted over two spatial scales (~ 100 pc and ~ 300 pc) clearly exhibit warm dust and polycyclic aromatic hydrocarbon (PAH) emission. The best fit dust and grain models reveal that both the intensity of the exciting radiation and PAH grain destruction increase toward the cluster center. Given that the timescale of evacuation is important for the future dynamical evolution of the cluster, it is important to determine whether O- and WR stars can evacuate the material gradually before supernova do so on a much faster timescale. With a minimum age of ≈ 3 Myr, it is clear that S26 has not yet fully evacuated its natal

material, which indicates that un-evolved O-type stars alone do not provide sufficient feedback to remove the gas and dust. I hypothesize that the feedback of WR stars in this cluster may be necessary for clearing the material from the gravitational potential of the cluster. As it is emerging and host to WR stars, S26 is similar to Emission Line Clusters observed in the Antennae Galaxies and may be considered a younger analog to 30 Doradus in the LMC.

2.2 Background

The energetics of galaxies are largely driven by the evolution of massive stars; and when clustered, the impact of these stars can be catastrophic. Massive stars modify their environment through strong, fast winds and eventual supernova explosions. These processes inject energy and distribute heavy elements, making massive stars critical to galaxy evolution (Maeder & Conti 1994). Massive stars are found in the highest concentrations in massive and super star clusters (SSCs), which host hundreds to thousands of massive stars in a few parsecs and form in the most intense regions of star formation in the universe. However, the physical conditions that produce SSCs, or even slightly smaller massive star clusters, remain uncertain, although it is apparent the feedback from the constituent massive stars will drive the cluster evolution. In this work, I present a massive star cluster undergoing a major transition that may develop our understanding of the interplay of massive stars and SSC evolution.

A picture of SSC evolution has developed in which SSCs form in thick, dense envelopes of natal material similar to scaled up versions of single massive stars (Johnson 2002). SSC evolution starts with a molecular cloud proto-cluster that begins to form stars, yet as these stars are still embedded in the natal cocoon, the early evolution is effectively obscured from view at many wavelengths. However, the massive stars within the embedded cluster begin to ionize the surrounding material. A number of these analogs to Ultra-compact H II (UCH II) regions have been identified in other galaxies; these vastly scaled up systems are detected as radio continuum sources (e.g. Kobulnicky & Johnson 1999; Turner et al. 2000; Johnson & Kobulnicky 2003; Johnson et al. 2004; Tsai et al. 2006; Reines et al. 2008; Johnson et al. 2009; Tsai et al.

2009; Aversa et al. 2011; Kepley et al. 2014) with a flat or inverted spectral index, indicative of thermal free-free emission from dense young H II regions. Kobulnicky & Johnson (1999) dubbed these sources as Ultra-dense H II regions (UDH IIs) (or similarly “supernebulae” by Turner et al. 2000).

The massive stars will continue to evolve and proceed to evacuate the surrounding material. One possible example of this emerging evolutionary stage are emission line clusters (ELC). Identified in the Antennae galaxies, ELCs are a type of H II region that are younger versions of SSCs and exhibit broadened Br γ line emission suggestive of massive stars evacuating their surroundings via wind (Gilbert & Graham 2007). Finally, the massive stars will be revealed at optical wavelengths and regulate or halt star formation (Agertz et al. 2013). This results in the final early evolutionary stage of SSCs as bright and blue optical clusters that are well studied with *Hubble Space Telescope* (*HST*) (Whitmore & Schweizer 1995). This last stage can be exemplified by the well-known region 30 Doradus (30 Dor) in the LMC, which is the closest SSC analog. The entire massive/SSC evolutionary sequence can be summarized as: protocluster \rightarrow UDH II \rightarrow emerging cluster (ELC) \rightarrow SSC (e.g. Whitmore et al. 2014).

Although some of the steps in the evolution have been outlined, ultimately the physical process of an UDH II region becoming a cleared-out, optical SSC is not yet well understood. For instance, cluster age measurements are not feasible until the stars are optically visible after clearing embedding material and the most massive stars have started to evolve off the main sequence. Population comparisons suggest that the UDH II phase lasts for < 1 Myr (Kobulnicky & Johnson 1999), however, a radio and optical study of NGC 4449 revealed that some clusters may in fact remain embedded up to 5 Myr (Reines et al. 2008). As for the evacuation process, many models assume an instantaneous removal at some given age (such as in Palfzner & Kaczmarek 2013). This picture is too simplified, as the rate of removal will surely change the fate of the cluster (Baumgardt & Kroupa 2007). Even accounting for the rate of removal is not enough: as shown by Palfzner & Kaczmarek (2013), a scenario simply comparing SFE or expulsion timescales is too limited to describe a cluster’s ability to stay bound and thus survive.

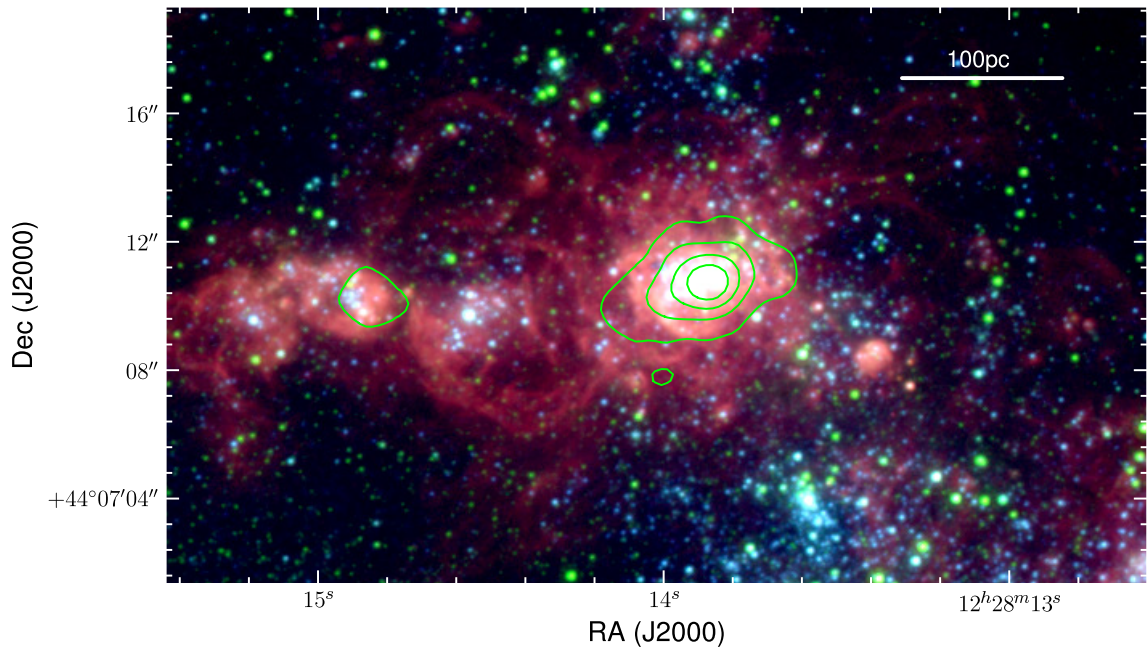


Fig. 2.1.— An *HST* rgb image ($H\alpha$, I, B) showing nebular emission surrounding a compact optical cluster in S26. The green contours show 3,4,5, and 6σ emission at 3.6 cm (Reines et al. 2008); the 3σ contour corresponds to a region with a radius of ~ 50 pc.

Perhaps most paramount, the dominant mechanism responsible for the evacuation of the natal material is unclear. Massive stars erode the obscuring envelope through a combination of stellar feedback processes including direct radiation from stars; pressure from cold, warm (the ionized H II region itself), and hot gas; dust processed IR radiation; protostellar winds and jets; and stellar winds and supernovae (e.g. Lopez et al. 2014). Yet, the relative importance of these mechanisms in removing the natal material is under debate—especially how these processes are coupled to the molecular cloud material (as discussed in Rogers & Pittard 2013).

I have identified a young massive cluster in NGC 4449 that appears to be undergoing this major transition between evolutionary phases, and its stellar content

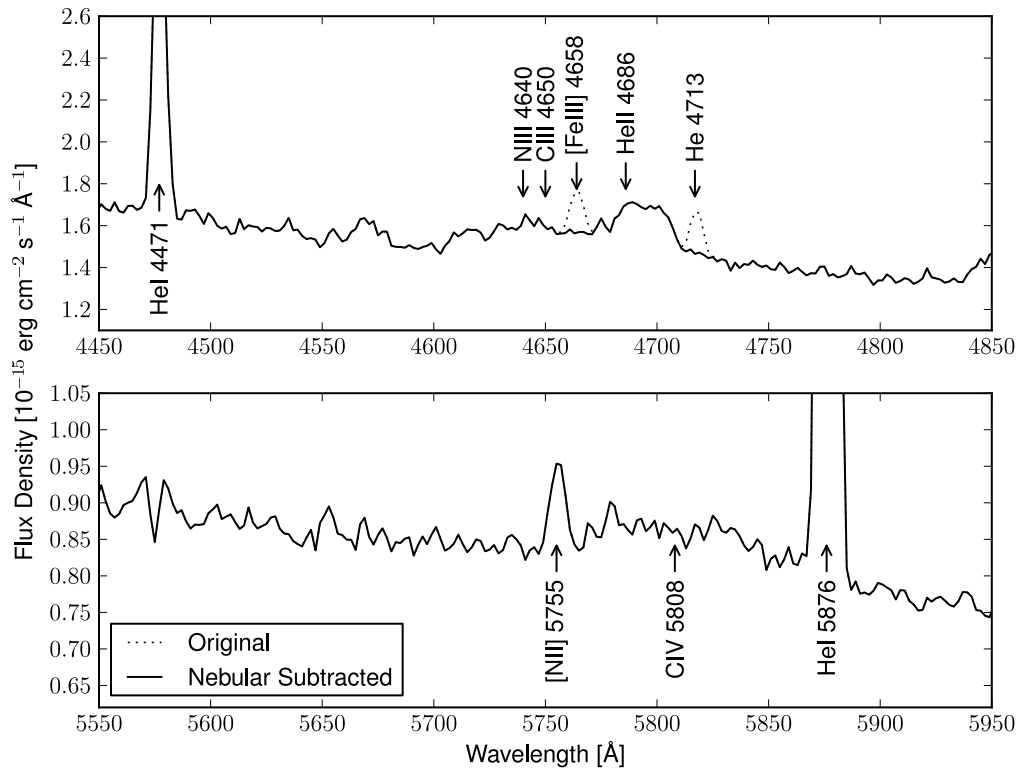


Fig. 2.2.— Flux calibrated spectra taken with DIS on the 3.5 m Telescope at Apache Point Observatory of the cluster S26 in NGC 4449, zoomed in on the broad Wolf-Rayet features. The dotted line shows the subtracted nebular features. Top—The “blue bump,” a composite of broad lines at 4640 Å, 4650 Å, and 4686 Å. Bottom—The broad “red bump” centered at 5808 Å. Obvious nebular and WR features are labeled.

is consistent with winds comprising a large component of the feedback driving the evolution. The massive star cluster (roughly 50 pc; shown in Figure 2.1) cataloged by Reines et al. (2008) as Source 26—S26 hereafter—in NGC 4449 simultaneously exhibits a thermal free-free radio emission component (Reines et al. 2008) and optical spectra showing features that reveal the presence of Wolf-Rayet (WR) stars (see Figure 2.2 and Reines et al. 2010) that begin to appear in ~ 3 Myr (Conti 1993). WR stars undergo rapid mass loss through fast winds with which they can drastically impact their environment. Thus, S26 may have been caught in the act of breaking out of

its natal cocoon, driven by the winds of the WR stars, providing an opportunity to observe the impact of evolved massive stars on their natal environment.

S26 is in a relatively low metallicity environment, and thus not only represents an important stage in cluster evolution, but also offers a window into a regime of star formation that is not well understood. The host galaxy NGC 4449 is an irregular Magellanic spiral that is close enough, at 3.9 Mpc (Annibali et al. 2008) where $1'' \sim 18$ pc, to resolve individual star-forming regions. Shown in Figure 2.3, the massive star cluster S26 can be found northward of the central part of the galaxy, at 12:28:13.86 +44:07:10.4 (Reines et al. 2008). The metallicity of the region has been measured from $Z = 0.004$ ($=0.28 Z_{\odot}$; Ryś et al. 2011) to $Z = 0.0063$ ($=0.44 Z_{\odot}$; Lequeux et al. 1979), which is comparable to the Large Magellanic Cloud (LMC) at $Z = 0.0068$ ($O/H = 8.37$; Russell & Dopita 1990).

In this section, I present a multi-wavelength analysis of the massive star cluster S26 in NGC 4449. The optical spectra and archival infrared data and reduction are discussed in Section 2.3. I evaluate general properties of the region, such as extinction and age, in Section 2.4. I determine the massive star populations in Section 2.5 and identify the thermal radio emission in Section 2.6. In Section 2.7, I construct SEDs and find the best fit dust models. In Section 2.8, I put S26’s massive star populations in context, discuss winds as possibly driving the evolution, and look at the similarities between S26 and 30 Doradus in the LMC. Finally, I present conclusions briefly in Section 2.9.

2.3 Observations and Data Reduction

2.3.1 Optical Spectra from APO

S26 in NGC 4449 was observed on 2008 April 13 with the 3.5 m telescope at Apache Point Observatory (Reines et al. 2010), using the red and blue channels of the Dual Imaging Spectrograph (DIS) in low-resolution mode. The total exposure time was 30 minutes, producing a signal-to-noise ratio per pixel of ~ 60 in the blue and ~ 45 in the red continua. The spectrum has a resolution of $\sim 7 \text{ \AA}$ over a wavelength range of

$\sim 3800\text{-}9800 \text{ \AA}$ and was reduced using IRAF and IDL routines. S26 was observed with a $1''.5 \times 360''$ slit and its spectrum was extracted from a $4''.4$ window. The correction factor to account for slit loss is 1.9, determined by comparisons to *HST* photometry of a region of radius $3''.3$ ($\approx 60 \text{ pc}$). Further details can be found in Reines et al. (2010).

The spectrum of the cluster S26 clearly displays typical WR line features (Fig. 2.2; also Reines et al. 2010), explained in detail in Section 2.5. After the initial spectral reduction of Reines et al. (2010), emission line features are further processed in this work using the IRAF SPLOT package. The blue bump WR feature, a composite feature of lines at 4650 and 4686 \AA , is analyzed after the prominent, superimposed nebular lines [Fe III] (4658 \AA) and He I and [Ar IV] (4713 \AA) are subtracted (Fig. 2.2). The observed line flux, extinction corrected line fluxes (see Section 2.4.1), and equivalent widths are given for emission lines in Table 2.1. Results are similar to those in Reines et al. (2010) for the only presented line, $\text{H}\alpha$.

2.3.2 Infrared Archival Data

2.3.2.1 *Spitzer* IRAC and MIPS

Infrared data from the *Spitzer Space Telescope* (Werner et al. 2004) were retrieved from the *Spitzer* Science Center Archive, consisting of InfraRed Array Camera (IRAC) (Fazio et al. 2004) and Multiband Imaging Photometer for SIRTf (MIPS) (Rieke et al. 2004) imaging. NGC 4449 was imaged with IRAC (PI: G. Fazio) at 3.6, 4.5, 5.8, and 8.0 μm (FWHM of $\sim 1''.9$; Fazio et al. 2004) and MIPS (PI: R. Kennicutt) at 24 μm (FWHM of $\sim 6''$; Rieke et al. 2004). The post-basic calibrated data from IRAC and MIPS images are used, which were reduced with the *Spitzer* Science Center pipeline. The flux calibration uncertainty is 2% (Reach et al. 2005) for IRAC and 4% for MIPS (Engelbracht et al. 2007).

2.3.2.2 *Herschel* PACS and SPIRE

The ESA *Herschel Space Observatory* (Pilbratt et al. 2010) has observed NGC 4449 as part of the Dwarf Galaxy Survey (Madden et al. 2013). NGC 4449 was observed with

Table 2.1. Emission Line Properties of S26

Wavelength (Å)	Identification	Observed Flux (10^{-13} ergs cm^{-2} s^{-1})	Extinction Corrected Flux (10^{-13} ergs cm^{-2} s^{-1})	EW (Å)
3835	H η	0.195 (0.013)	0.306 (0.059)	7.8 (0.7)
3868	[Ne III]	0.754 (0.033)	1.18 (0.22)	29.5 (2.7)
3889	H ζ	0.527 (0.023)	0.82 (0.15)	21.1 (1.5)
3970	H ϵ	0.607 (0.026)	0.95 (0.17)	25.1 (2.0)
4076	[S II]	0.019 (0.013)	0.030 (0.021)	0.8 (0.6)
4102	H δ	0.720 (0.023)	1.12 (0.19)	33.5 (1.5)
4341	H γ	1.323 (0.042)	2.03 (0.33)	70.0 (4.1)
4363	[O III]	0.066 (0.017)	0.101 (0.031)	3.6 (1.2)
4471	He I	0.116 (0.011)	0.177 (0.033)	7.1 (1.0)
4650	[C III] (blue bump)	0.102 (0.018)	0.155 (0.037)	7.1 (1.3) ^a
4658	[Fe III]	0.015 (0.001)	0.0223 (0.0035)	0.94 (0.02)
4686	He II (blue bump)	0.077 (0.013)	0.116 (0.026)	5.3 (0.9) ^a
4713	[Ar IV]/He I	0.014 (0.001)	0.0213 (0.0033)	0.96 (0.02)
4861	H β	3.00 (0.11)	4.52 (0.68)	185 (49)
4959	[O III]	4.33 (0.24)	6.50 (1.00)	300 (200)
5007	[O III]	13.40 (0.46)	20.07 (2.96)	940 (750)
5755	[N II]	0.009 (0.001)	0.0125 (0.0017)	1.0 (0.1)
5808	[C IV] (red bump)	0.040 (0.026)	0.059 (0.039)	4.9 (3.4) ^a
5876	He I	0.348 (0.013)	0.510 (0.067)	43.6 (3.6)
6300	[O I]	0.0410 (0.0035)	0.0595 (0.0087)	6.13 (0.72)
6312	[S III]	0.0486 (0.0033)	0.0705 (0.0096)	7.25 (0.70)
6548	[N II]	0.101 (0.070)	0.15 (0.10)	8.7 (8.5)
6563	H α	9.60 (0.32)	13.86 (1.66)	580 (380)
6584	[N II]	0.350 (0.093)	0.51 (0.15)	46 (28)
6678	He I	0.106 (0.0051)	0.153 (0.019)	18.9 (1.6)
6717	[S II]	0.294 (0.024)	0.423 (0.059)	59 (27)
6732	[S II]	0.218 (0.023)	0.314 (0.049)	44 (23)
7065	He I	0.0778 (0.0066)	0.112 (0.015)	15.9 (2.7)
7137	[Ar III]	0.344 (0.013)	0.493 (0.056)	66.5 (8.6)
7319	[O II]	0.0728 (0.0039)	0.104 (0.012)	16.1 (1.5)
7330	[O II]	0.0584 (0.0034)	0.083 (0.010)	13.0 (1.3)
7751	[Ar III]	0.0827 (0.0048)	0.117 (0.014)	19.3 (2.3)
9069	[S III]	0.974 (0.043)	1.36 (0.14)	500 (630)
9532	[S III]	2.503 (0.086)	3.49 (0.33)	... ^b

Note. — Tabulated quantities are: intrinsic wavelength, common identification, observed flux, extinction corrected flux, and equivalent width (EW). Uncertainties follow in parentheses.

^aThe WR features are broad.

^bNot well constrained.

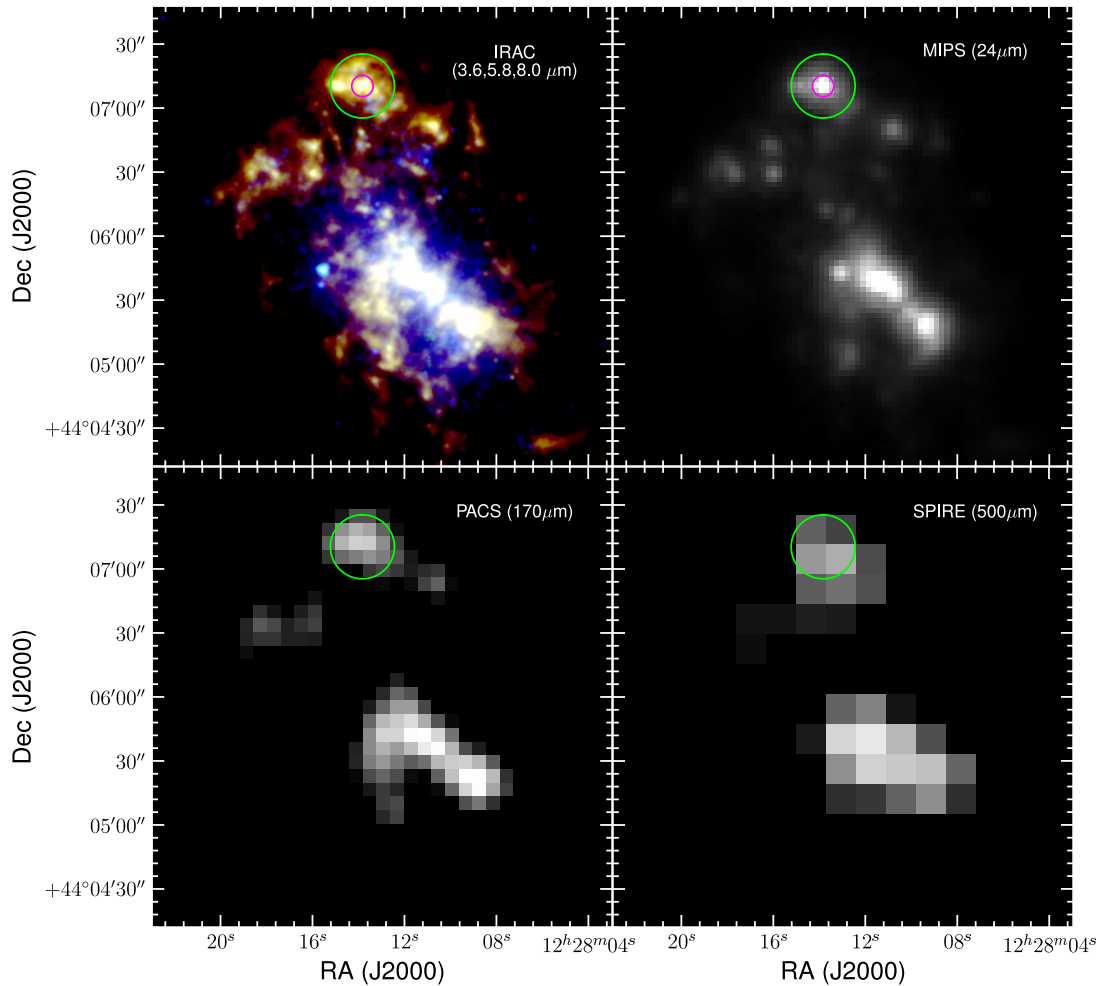


Fig. 2.3.— An infrared view of the massive cluster S26 in NGC 4449. From top left moving clockwise: an *Spitzer* IRAC rgb image (3.6, 5.8, and 8.0 μm), *Spitzer* MIPS 24 μm , *Herschel* PACS R (170 μm), and *Herschel* SPIRE PLW (500 μm). The extraction regions for constructing the source SED (Fig. 2.6) are plotted in red (small 5'' \sim 100 pc circle) and green (large 15'' \sim 300 pc circle). S26 is a dominate source of emission even at the longest wavelengths.

the Photodetector Array Camera and Spectrometer (PACS) (Poglitsch et al. 2010) at 70, 100, and 160 μm (FWHM of the point-spread function PSF is 5.2, 7.7, and 12''.0, respectively) and the Spectral and Photometric Imaging REceiver (SPIRE) (Griffin et al. 2010) at 250, 350, and 500 μm (FWHM of 18.2, 24.9, and 36''.3, respectively).

The newly released “Level 2.5” data from PACS are analyzed, using MadMap

images to preserve extended structure (Rémy-Ruyer et al. 2013). The PACS calibration uncertainty is of the order of 10%, e.g. Fritz et al. (2012). For the SPIRE data, I analyze the “Level 2.0” and adopt a conservative uncertainty of 15% on flux calibration, as according to the SPIRE observer’s manual (<http://herschel.esac.esa.int/Docs/SPIRE/html/>) the overall calibration uncertainty for the SPIRE photometer is 7-15%. For both PACS and SPIRE datasets, astrometric corrections are applied to the data using the peak emission of the nucleus of NGC 4449.

2.4 General Properties of S26

2.4.1 Extinction

The extinction of a star-forming region is crucial for accurate line measurements, as well as information on the extent to which a source is embedded. Using nebular lines only measures extinction toward gas that is not very heavily extinguished and thus can be biased low. The extinction of S26 is derived through optical nebular Balmer line and radio fluxes from Reines et al. (2008). Extinction curves for the 30 Doradus region of the LMC (Misselt et al. 1999; Fitzpatrick 1985) are used to convert the Balmer decrement to A_V , appropriate as the dust processing and the metallicity of the two regions are similar, roughly $Z = 0.008$ (Russell & Dopita 1990). Use of a Milky Way extinction curve changes the measured extinction by only $\sim 10\%$.

The total extinction of S26 is measured to be $A_V = 0.41$ and is used in correcting the optical line fluxes in Table 1. Subtraction of the Galactic foreground extinction results in an internal extinction of $A_{V,i} = 0.35$: along the S26 line of sight, the Milky Way galactic extinction is measured as $E(B-V) = 0.019$ (Schlegel et al. 1998), converted assuming the standard galactic curve $A_V = 3.1 E(B-V)$. Within the uncertainties, this internal extinction is in agreement with $A_{V,i} = 0.40$ as estimated by Reines et al. (2010) by fitting the spectrum with STARBURST99 models.

2.4.2 Electron Temperatures, Density, and Pressure

In order to probe the pressure as well as measure oxygen abundance as a proxy for metallicity, I estimate the electron density and temperatures in S26. These physical conditions in the ionized gas of S26 are determined through ratios of line fluxes using the five-level atom model (De Robertis et al. 1987) with the NEBULAR package in IRAF. The electron density is estimated using the S II line ratio $6716\lambda/6731\lambda$ and the S⁺ electron temperature given by the line ratio $(6716\lambda+6731\lambda)/4076\lambda$. The electron density is estimated to be $n_e(\text{S II}) \approx 75 \text{ cm}^{-3}$, although it may vary by as much as a factor of four due to propagation of flux uncertainties also impacting the temperature. The S⁺ electron temperature is $T(\text{S II}) = 6500 \pm 800 \text{ K}$. The O⁺ electron temperature is determined by $T(\text{O II}) = T(\text{N II})$ (Izotov et al. 1994), which results from the H II photoionization models of Stasińska (1990), and is measured to be $T(\text{N II}) = 13500 \pm 1400 \text{ K}$ using the [N II] ratio $(6548\lambda+6584\lambda)/5755\lambda$. The O⁺⁺ electron temperature is measured to be $T(\text{O III}) = 9400 \pm 500 \text{ K}$ using the [O III] ratio $(4959\lambda+5007\lambda)/4363\lambda$. Using the estimated density of 75 cm^{-3} then implies a pressure of $P/k = 7.5 \times 10^5 \text{ cm}^{-3} \text{ K}$ for S26. The temperatures, density, and pressure estimated for S26 fit the observed range of typical H II regions in disk galaxies and ELC regions in the Antennae Galaxy (Gilbert & Graham 2007; Hunt & Hirashita 2009). Thus, the standard H II temperature of 10^4 K as a representative single temperature is assumed throughout this work.

2.4.3 Metallicity via Oxygen Abundance

I derive the oxygen abundances using the standard T_e method with two distinct temperature zones in the photoionized H II region, as in Izotov et al. (1994, 1997), using the O⁺ and O⁺⁺ electron temperatures are explained above. The total oxygen abundance is derived by $\text{O}/\text{H} = \text{O}^+/\text{H}^+ + \text{O}^{2+}/\text{H}^+$: O⁺ ionic abundance is measured with the summed flux of the doublet $7319/7330\lambda$, and O²⁺ ionic abundance is determined using ionic abundances for the lines 4363λ , 4959λ , and 5007λ . The total oxygen abundance is measured to be $12 + \log(\text{O}/\text{H}) = 8.3 \pm 0.2$, which is in agreement with checks using empirical relations from Izotov et al. (2006) that were computed with

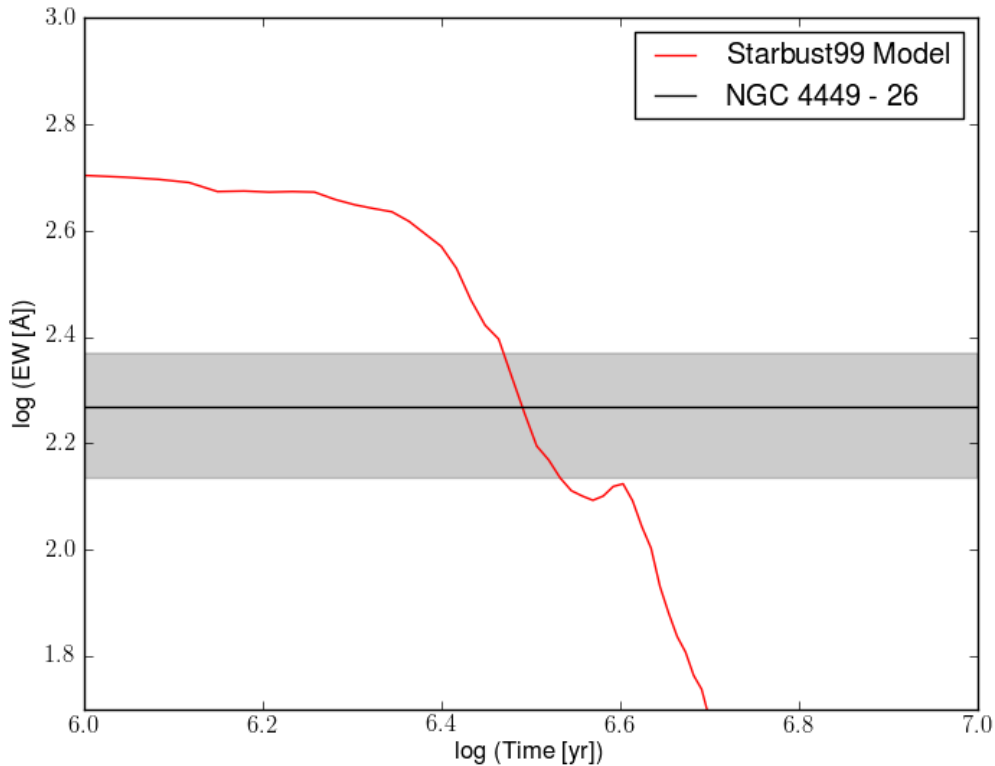


Fig. 2.4.— STARBURST99 predictions for the cluster age vs. the equivalent width of the $H\beta$ (4861 \AA) line (see Section 2.8.1.1). The observed EW of $H\beta$ for the massive star cluster S26 in NGC 4449 (solid line with uncertainties shown as a shadowed region) implies an age of $3.1 \pm 0.3 \text{ Myr}$.

new photoionization models. By assuming a simple scaling relation and the solar metallicity value $12+\log(\text{O}/\text{H})_{\odot} = 8.69$ (Asplund et al. 2009), the oxygen abundance converts roughly to a metallicity of $Z \sim 0.006$ ($=0.4 Z_{\odot}$), similar to the LMC. The measured oxygen abundance of S26 is in excellent agreement with the value found by Lequeux et al. (1979) of $12+\log(\text{O}/\text{H}) = 8.38$.

2.4.4 Age

Ages are instrumental to characterizing the timescales of the early evolutionary stages of massive star clusters, as well as necessary for comparisons to predictions and other

observed objects. The age of S26 is estimated by comparing the equivalent width of $H\beta$ to the evolutionary synthesis models of STARBURST99 (Leitherer 1999), using the measured equivalent width of $H\beta$ of $\approx 185 \text{ \AA}$, and adopting a metallicity of $Z = 0.008$ (see details provided in Section 2.8.1.1). As shown in Figure 2.4, I derive an age of $3.1 \pm 0.3 \text{ Myr}$ for S26, consistent with Reines et al. (2010).

2.5 WR Features and the Massive Star Populations

The first hint of the important evolutionary phase of S26 was the discovery of an optical feature due to WR stars (Reines et al. 2010). WR stars are spectroscopically identifiable via unique emission lines and are divided into subtypes of nitrogen-rich WNs, carbon-rich WCs, and oxygen-rich WOs; the presence of several WR stars will produce broad features in the integrated optical spectrum known as WR “bumps” (Fig. 2.2). S26 clearly displays broad WR features of both WN and WC populations, namely the “blue bump” near 4650 \AA , consisting of a blend of $[\text{N III}] 4640 \text{ \AA}$, $[\text{C III}] 4650 \text{ \AA}$, and He II at 4686 \AA , and the “red bump” due to $[\text{C IV}]$ at 5808 \AA . The emission at 4686 \AA of S26 does not display a clearly distinct nebular component (Fig. 2.2) often seen in the integrated spectra of WR galaxies e.g. Conti (1991). However, at relatively low metallicities, such as S26, the stellar component is thought to dominate (Schaerer & Vacca 1998). The expected nebular emission for a population of 3 - 3.5 Myr should be $\log\left(\frac{I(\text{nebular He II } [4686 \text{ \AA}])}{I(H\beta)}\right) \sim -2$ according to Schaerer & Vacca (1998). Thus, the expected nebular emission is too low to be significantly detected or distinguished from the stellar emission at 4686 \AA with this dataset, and thus the lack of resolved nebular emission is not surprising. Other WR features that could further classify the WR population would be similarly too faint to detect.

2.5.1 Determining the Number of WR Stars

The luminosity of a WR feature can be used to constrain the WR population and estimating the WR star populations in an extragalactic source has become fairly

standardized (e.g. Schaerer & Vacca 1998; Guseva et al. 2000). The number of WR stars can be estimated as $N_{\text{WR}} = L_{\text{WR}}/L_{\text{o,WR}}$, with $L_{\text{o,WR}}$ as a typical single WR star producing the feature and L_{WR} as the observed luminosity of that feature from the source. The subtypes can be separately analyzed with their respective WR lines. Many uncertainties result from this method due to the inherent range of WR line fluxes emitted by individual stars, averaging over WR subtypes, and the currently poor understanding of the impact of environment on WR line fluxes. Nonetheless, it is useful to estimate the massive star populations within a cluster, as long as the range of uncertainties are kept in mind while interpreting the results.

In order to constrain the WR subtype populations in S26, the method of Guseva et al. (2000) is adopted. The red bump at 5808 Å is thought to be produced only by WCE stars and can be compared to representative WC4 stars. The number of WC stars can be approximated as $N_{\text{WC}} = L(5808 \text{ Å})/L_{\text{WC4}}(5808 \text{ Å})$, assuming a typical luminosity of a single WC4 star at 5808 Å is 3.0×10^{36} ergs s⁻¹ as measured in the LMC (Schaerer & Vacca 1998).

Determining the number of WN stars is less straight forward because the blue bump includes contributions from both WN and WC stars. The relative contribution of WC stars to the blue bump feature can be estimated from the red bump, unique to the WCs, and is described by the coefficient $k = L_{\text{WC4}}(4650 \text{ Å})/L_{\text{WC4}}(5808 \text{ Å})$ (Guseva et al. 2000). I adopt a value of $k=1.71 \pm 0.53$ (Schaerer & Vacca 1998; Guseva et al. 2000), although uncertainties are large due to variations in relative line fluxes (Schaerer & Vacca 1998). After subtracting the estimated WC contribution from the total measured flux in the blue bump, the number of WN stars is found by comparing the remaining emission to a typical WN star. I assume a typical WN of a WNL (WN7) star to be with a luminosity of 2.0×10^{36} erg s⁻¹ in the blue bump (4650 + 4686 Å; Guseva et al. 2000) as in the LMC.

In total, I have estimated 20 ± 14 WR stars in S26, comprised of roughly 4 ± 3 WC and 16 ± 13 WN stars. The results can be found in Table 2.2. The uncertainties are estimated from assuming a typical flux, using the observed flux range in the LMC by Schaerer & Vacca (1998), as well as from flux measurement uncertainties in Table 2.1. Due to the large range of observed variation of fluxes, the uncertainties are

correspondingly, and unavoidably, large. Another potential uncertainty that has not been accounted for arises from the weak He II line emission from the most massive O-stars (Of-stars), which may result in an overestimate of WN stars. However, this effect is expected to be small at the metallicity and age of S26, roughly Of/O \sim 0.15, which with the weak He II emission (10% of a WN star) would contribute a total of \sim 2 WN stars (Schaerer & Vacca 1998). Additionally the ratio of WC to WN stars appears normal, see Section 2.8.1.2, and thus Of-star contamination is likely not important.

2.5.2 Determining the Number of O-stars

Identifying the total massive star population in S26 is important for understanding the feedback processes that are altering the cluster. In addition to the massive WR stars that are driving strong winds and hard radiation throughout the cluster, the O-star populations will also contribute ionizing radiation and additional (albeit weaker) winds. The number of O-stars can be estimated by determining the population needed to produce the observed ionizing photons Q_o , after subtracting off the WR contributions. The ionizing flux seen at optical wavelengths is simply estimated through empirical relations from Schaerer & Vacca (1998). Using $H\beta$ at 4861 Å, the ionizing flux is $Q_o \sim 170 \times 10^{49}$ photons s^{-1} . The number of O-stars are thus estimated by assuming

$$N_O = (Q_o - N_{WR}Q_{o,WR})/(\eta_o Q_{o,O7V})$$

Table 2.2. Massive Star Populations in S26

Type	Number
O	219 ± 15
WNL	15 ± 12
WCE	3 ± 3
WR _{total}	18 ± 13
WR/O	0.084 ± 0.058
WC/WN	0.23 ± 0.26

(Guseva et al. 2000). The parameter η_o is the ratio of O7V stars to all O-stars, included to account for different O-star subtypes occurring within IMF (as subtypes produce different ionizing photon fluxes). At an age of 3.1 Myr and Salpeter IMF, I find $\eta_o \sim 1.2$ for the cluster S26 (Schaerer & Vacca 1998), near the peak value resulting from a WR rich phase. A typical ionizing photon flux for an O-star is $Q_{o,O7V}$ is taken to be $10^{48.75} \text{ s}^{-1}$ from an O7V star (Martins et al. 2005) and 10^{49} s^{-1} for a WR star (Guseva et al. 2000; Scherer et al. 1999). O-star population uncertainties are estimated by accounting for the measured flux uncertainty in S26, estimated uncertainties on η_o , and uncertainties for the subtracted WR populations. With a WR population of $N_{\text{WR}} = 18$ from above, I find there are approximately 219 ± 15 total O-stars harbored in the massive star cluster S26.

2.6 The Thermal Radio Component of S26

The radio spectral indices of S26 indicate that the source hosts mixed thermal and non-thermal contributions; and as shown in Figure 2.1, the radio continuum contours additionally change from a resolved, irregular shape at 3σ to an unresolved, compact peak at 6σ . Despite the messy nature of S26, it is necessary to identify the radio emission produced by the H II region itself in S26. I decompose the observed radio emission to the published fluxes at 1.3, 3.6, and 6.0 cm from Reines et al. (2008) and assume the thermal emission follows $F_\nu \propto \nu^{-0.1}$ and non-thermal emission as $F_\nu \propto \nu^{-0.7}$ (e.g. Baars et al. 1977). The thermal emission is, however, dependent on both the size and density of the emitting region as $S_{\nu,\text{thermal}} \propto 2kT\nu^2\tau_\nu/c^2$, and the models are thus under-constrained. To better constrain the fit, the approximate size of the 3.6 cm radio continuum emission region is adopted. The 3σ contour suggests a radius of ~ 50 pc—however a smaller size would be derived if only the unresolved peak emission was used (Reines et al. 2008, also seen in Figure 2.1).

I find the model with the lowest χ^2 by both setting the radius and leaving it as a free parameter, as shown in Figure 2.5. By imposing a radius of the adopted value of 50 pc, the density is $n_e = 21.5 \text{ cm}^{-3}$ and the non-thermal contributions at 1.3 cm are $14\% \pm 15\%$, the band least contaminated by non-thermal emission. If the radius

is unconstrained, the thermal radio emission results from a region of radius of $r = 2.3$ pc, a density of $n_e = 2.0 \times 10^3 \text{ cm}^{-3}$, and non-thermal contributions at 1.3 cm of $28\% \pm 25\%$. The fit is under-constrained for both models ($\chi_{\text{red}}^2 \sim 0.5$ and ~ 0.1 for a set and free radius) and the equality of the fits cannot discriminate between the two conditions and rather express both as possibilities.

Thus, the radio data is consistent with both a large, low-density H II region typical of Giant H II regions (GHRs) and a very dense, compact region typical of UDH IIs (or, more likely, a combination of the two, although the data do not permit a more sophisticated model). S26 clearly has associated extended thermal radio emission, thus there may be a low filling factor of small dense regions or a single very dense region within a larger, less dense S26 H II region. This type of scenario has been observed in Mrk 996, where the extremely dense ($n_e \sim 10^6 \text{ cm}^{-3}$) nucleus is surrounded by a less dense ($\sim 10^2 \text{ cm}^{-3}$) star-forming region, along with WR stars (Telles et al. 2014). Thus, it seems the flux at 1.3 cm of $S_{\nu, 1.3 \text{ cm}} \sim 1360 \mu\text{Jy}$ is roughly representative of the thermal radio emission. While S26 is not solely a thermal source, decomposition shows the flux at 1.3 cm can be considered primarily thermal.

While the majority of the thermal radio emission may be emitted by an H II region surrounding the cluster, the WR populations will also contribute to the observed radio flux. Strong WR winds are known to produce thermal free-free radio emission, approximated by the scaling relation

$$S_{\nu} \propto \frac{\dot{M}}{v_{\infty}^{4/3}} \frac{\nu^{0.6}}{D^2}$$

in which \dot{M} is the mass loss rate, v_{∞} is the terminal wind velocity, and D is the distance (Crowther 2007). Using this relation, the expected radio flux density contribution from the WR stars in S26 can identify whether the H II region or the WR winds are the likely dominant emitter. Accounting for metallicity, I can estimate the expected radio flux density by scaling from galactic WR stars observed with the Very Large Array (Cappa et al. 2004). Exactly how mass-loss rates depend on environment is not well known, although mass-loss rates at low metallicities are observed to be lower than higher metallicity environments as $\dot{M}_{\text{WN}} \propto Z^{0.7}$ and $\dot{M}_{\text{WC}} \propto Z^{0.5}$ (Crowther &

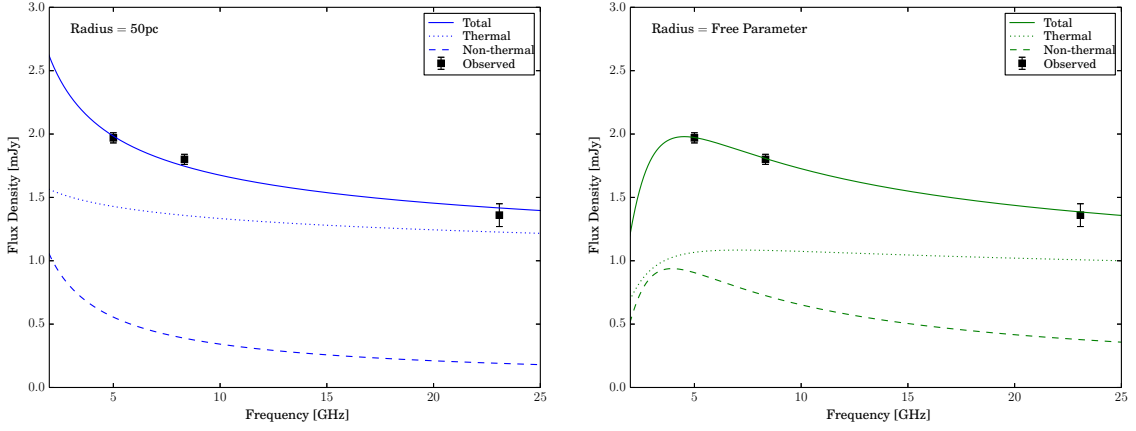


Fig. 2.5.— Identifying the thermal radio component in the radio SED of S26, as observed by Reines et al. (2008), with a χ^2 fit to the observed fluxes of the expected emission assuming thermal emission goes as $F_\nu \propto \nu^{-0.1}$ while non-thermal emission as $F_\nu \propto \nu^{-0.7}$. Top: constraining the fit such that the radius is set to 50 pc, as observed by the irregular 3σ contour of the radio continuum, the flux has non-thermal contributions of 14% at 1.3 cm. Bottom: allowing the radius to be a free parameter (although under-constraining the fit) results in an increased non-thermal contribution of 28% at 1.3 cm from a region of radius 2.3 pc.

Hadfield 2006). Clumping in the winds can additionally reduce mass loss rates by factors of two (Crowther 2007). Taking a generic WC star for example, WR 5 (WC6 star) with $S_\nu = 0.20$ mJy at 3.6 cm (Cappa et al. 2004) would produce $S_{\nu,3.6 \text{ cm}} \sim 5.2 \times 10^{-8}$ mJy at the distance and metallicity of S26 in NGC 4449. Similarly, the radio flux density of a WN star could produce $S_{\nu,3.6 \text{ cm}} \sim 5.6 \times 10^{-7}$ mJy (e.g. the WN 7 star WR 100). Summing the total population of WR stars in S26 and scaling to 1.3 cm, a flux density of around $S_{\nu,1.3 \text{ cm}} \sim 9 \times 10^{-6}$ mJy is expected due to the WR winds, which compared to the observed flux of $S_{\nu,1.3 \text{ cm}} \sim 1.360$ mJy, is negligible. Therefore, the thermal radio emission at 1.3 cm resulting from the WR winds is $1:10^{-5}$ to the thermal radio emission observed in S26 and the majority must be resulting from free-free emission from the H II region ionized by the stars.

2.7 Dissecting the Dust

Archival data of the galaxy NGC 4449 from near-infrared to far-infrared wavelengths is utilized to construct the spectral energy distribution (SED) of the massive star cluster S26. The infrared emission from S26 is clearly one of the dominating sources in its host galaxy, shown in Figure 2.3, and at the longest wavelength (500 μm) is comparable in brightness to the nuclear emission.

2.7.1 Photometry

Embedding material surrounding S26 is evident throughout the rich archival dataset of NGC 4449 and can be characterized through photometry and the construction of an SED. An SED provides key information on the heated dust properties and is crucial in describing the evolutionary phase. However, the wavelength coverage from a few to hundreds of μm , along with source complexity as well as corresponding worsening resolution, necessitates careful treatment of the different datasets to preserve the shape of the SED.

Photometry is performed using two apertures to evaluate both the resolved emission and the total emission, which additionally will provide insight into any radial trends; the apertures are overlaid in Figure 2.3 and explained below. Aperture photometry is performed using the IDL procedure SURPHOT (Reines et al. 2008). The uncertainties are dominated by background subtraction, and these are estimated empirically by calculating the standard deviation of the fluxes measured using different backgrounds.

Using native PSFs, I use a small extraction aperture for images where S26 is resolved from nearby sources (images centered at 100 μm or less). A small circular aperture with a radius of 5" (~ 100 pc; see Figure 2.3) is adopted, which sufficiently excludes nearby sources while including the resolved emission from S26. I follow the IRAC Instrument Handbook for Calibration of Extended Sources http://irsa.ipac.caltech.edu/data/SPITZER/docs/irac/iracinstrumenthandbook/29/#_Toc296497401 as well as the procedure in Rémy-Ruyer et al. (2013) and the encircled energies in Balog et al. (2014) for extracting fluxes from PACS data, in

agreement with http://herschel.esac.esa.int/Docs/HerschelUG/HUG2web_BA_PACSExtendedSourcePhotometry.pdf

The total emission is measured with a large aperture over the complete dataset. However, resolution matching is necessary due to the large change in PSF with increasing wavelength for the IR datasets. Therefore, I construct the total emission SED using a large aperture extraction region (a $15'' \sim 300$ pc radius) on images convolved to a common resolution (SPIRE $500 \mu\text{m}$ with a PSF of $36''$) using convolution kernels provided by Aniano et al. (2011). The aperture correction for images convolved to the SPIRE $500 \mu\text{m}$ PSF and extracted with the large aperture are found by applying the same photometry procedure to the corresponding PSF and the same extraction apertures, as the region size is sufficiently small enough to approximate a point source at this PSF.

2.7.2 SED of S26

The spectral energy distribution (SED) of S26 is shown in Figure 2.6; the shape and peak result from large amounts of heated dust. For comparison, the expected stellar emission from the STARBURST99 model (see Section 2.8.1.1) of a cluster of similar mass undergoing an instantaneous starburst is also plotted. It is clear that the infrared emission cannot be produced solely by stellar sources. Instead, this emission is produced from a combination of heated dust partially embedding the cluster and Polycyclic Aromatic Hydrocarbon grain (PAHs) emission in the photodissociation region (PDR) surrounding the ionizing stars of the cluster. Strong evidence for PAH emission is observed as an excess from the IRAC 5.8 and $8.0 \mu\text{m}$ —viewed as a bump between the IRAC $4.5 \mu\text{m}$ and MIPS $24 \mu\text{m}$ points. The infrared emission is extracted using two different methods due to the drastic change in resolution at increasing wavelengths, as explained above. Not surprisingly, the SED extracted from the large aperture results in more emission than the SED resulting from the smaller aperture.

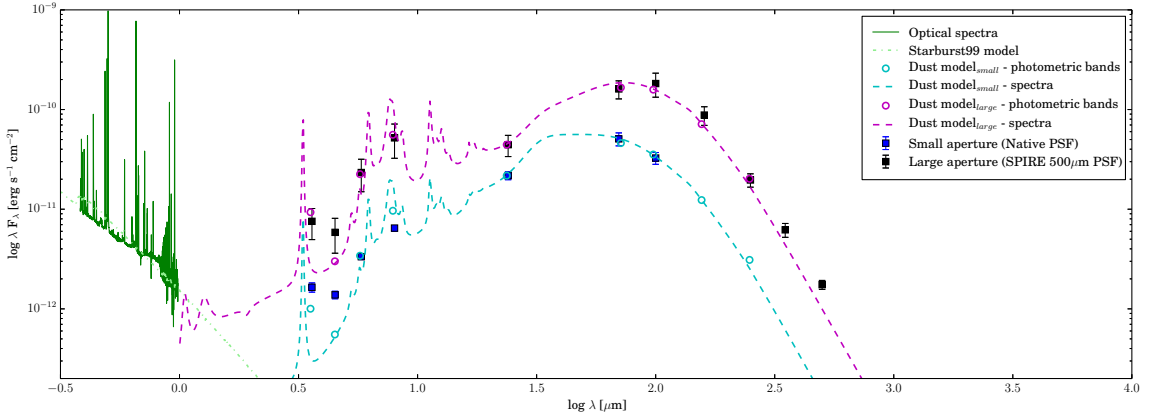


Fig. 2.6.— An SED of the optical to far-IR emission from the massive star cluster S26 with dust and grain models over plotted for comparison. Optical spectra (green line) is from Reines et al. (2010), and a STARBURST99 model (dotted green line) clearly demonstrates an abundance of IR emission to the expected stellar emission. The IR photometry and dust and grain model fitting utilize two apertures, explained in further detail in Section 2.7: A small 5'' aperture (blue squares) used to extract emission from images with native PSFs, and a large 15'' aperture (black squares) used to extract emission from images convolved to the resolution of SPIRE 500 μm . The best fit dust and grain model from Draine & Li (2007) are plotted for the corresponding aperture (large or small), where the dotted line shows the model spectra and the empty circular dots show the photometric fluxes. The SED clearly shows strong PAH features and large amounts of dust surrounding S26. The change in PAH emission in the IRAC bands at 5.8 and 8.0 μm and the shift in the peak IR emission can be seen between the two IR aperture SEDs, plausibly due to increased exciting radiation and destruction of PAHs toward the cluster center.

2.7.3 The Best Fit Dust and Grain Model

SEDs can be quantitatively analyzed to describe the emitting material: to characterize the dust, PAH components, and exciting radiation, I compare dust and grain models of a gas and dust mixture heated by a distribution of starlight intensities from Draine & Li (2007) to the infrared SED of S26. The starlight intensity is given by a scaling factor U such that the energy density per unit frequency is $u_\nu = Uu_\nu^{\text{MMP83}}$, where the interstellar radiation field u_ν^{MMP83} is from Mathis et al. (1983). The fraction of the dust mass that is exposed to a distribution of intensities from U_{min} to U_{max} is described by the parameter γ ; therefore $(1-\gamma)$ is the fraction exposed to U_{min} . The

fraction of the total dust mass that is in PAH particles is q_{PAH} and expected to be low at the low metallicity of NGC 4449.

The best fit models to the S26 SEDs are found via a χ^2 test between the observed photometric data for S26 and a model's photometric flux at corresponding bands. The characteristics of the best fit models are listed in Table 2.3 and the fits are shown in Figure 2.6. The best fit models suggest that the exciting radiation in S26 is strong, with a maximum starlight intensity of $U_{\max} = 10^6$, which is similar to starbursting galaxies. The minimum exciting intensity may increase towards the cluster center, as $U_{\min} = 12.0$ for the best fit model to the large aperture SED and $U_{\min} = 25.0$ for the best fit model to the small aperture SED. Compared to a global estimate of 2% PAH emission in NGC 4449 (Karczewski et al. 2013), the best fit models may additionally indicate this changing environment toward the center of S26. The large aperture SED (extracted from a radius of ≈ 300 pc) best matches a model with high PAH emission (3.19%) and nearer to the center of the cluster, the small aperture SED (extracted from a radius of ≈ 100 pc) best matches a model where the PAH emission is reduced to 1.12%. Thus, the dust grains may be being destroyed due to a higher radiation field.

2.7.4 Dust Mass and Star Formation Efficiency

Dust is an integral component to the natal cluster environment. Understanding the dust mass that is surrounding a region is important in determining the evolutionary stage, providing comparisons of similar regions to formulate an observational picture, and for extrapolating to estimate the gas mass. The ratio of the stellar to gas mass serves an indicator for the degree of removal of natal material. Utilizing results of the dust model fitting and the observed photometric fluxes, the dust mass surrounding the cluster S26 can be estimated. Following the method of Draine & Li (2007), I find a total dust mass of $2.3 \times 10^5 M_{\odot}$ as measured with the large aperture (with uncertainties of 15% due to flux uncertainties alone). Due to the resolution at the long wavelengths necessary for the dust mass estimate, this measurement is only over this spatial scale, which is ~ 300 pc.

Table 2.3. SED of S26: Photometry and Model Parameters

	Small Aperture	Large Aperture
Band	Flux Density (mJy)	Flux Density (mJy)
IRAC 3.6 μm	1.98 (0.21)	9.1 (3.1)
IRAC 4.5 μm	2.07 (0.18)	8.8 (3.4)
IRAC 5.8 μm	6.46 (0.42)	45 (16)
IRAC 8.0 μm	17.24 (0.93)	139 (52)
MIPS 24 μm	174 (17)	355 (88)
PACS 70 μm	1180 (180)	3760 (770)
PACS 100 μm	1090 (150)	6100 (1600)
PACS 170 μm	...	4690 (990)
SPIRE 250 μm	...	1640 (250)
SPIRE 350 μm	...	720 (120)
SPIRE 500 μm	...	290 (30)
U_{\min}	25.0	12.0
U_{\max}	10^6	10^6
γ	0.08	0.03
q_{PAH}	1.12%	3.19%

^a Notes: The upper part of the table presents the flux densities extracted from the corresponding aperture. The lower part of the table presents the parameters determined by the best fit models from Draine & Li (2007), which describe a gas and dust mixture heated by a distribution of starlight intensities, U , where the local starlight intensity is $U = 1$. The fraction of the dust mass exposed to U_{\min} is $1-\gamma$. The emission due to the PAH particles is given as q_{PAH} .

This total dust mass, which is sampled over a large region, is roughly three times the stellar mass estimated by Reines et al. (2010) of $6.5 \times 10^4 M_{\odot}$, which corresponds to a region of $r=3''.3$. However, the stellar mass can be scaled to the same large $15''$ aperture used for the dust mass estimate. I determine this scale factor by comparing the flux measured in an archival *HST* I-band image extracted with the $r=15''$ circle (as above) to the value published in Reines et al. (2010). The scaled stellar mass in S26 over the large aperture is $3.0 \times 10^5 M_{\odot}$. To estimate the total gas mass surrounding the cluster as well, I assume a dust-to-gas ratio suggested by the best fit model from Draine & Li (2007) of $1/130$, which gives a gas mass of $3.0 \times 10^7 M_{\odot}$. The uncertainties are at least 50% based on the range of acceptable models and adopting a dust-to-gas ratio. For comparison to the host galaxy, modeling by Karczewski et al. (2013) found a global value of dust-to-gas ratio equal to $1/190$ in NGC 4449. Regions of higher star formation events such as in LIRGs show average values of the gas to dust ratios of 120 ± 28 (Luminous Infrared Galaxies–LIRGS; Wilson et al. 2008), in excellent agreement with the model value found for S26. By adopting the above total gas mass, the star formation efficiency (SFE) of the entire S26 region can be estimated.

A gas mass this large implies a low *global* SFE of 1% for the region of $r \sim 300$ pc surrounding S26. Typical values for bound clusters are observed to be $\text{SFE} \approx 20\text{-}50\%$ (Ashman & Zepf 2001; Kroupa et al. 2001). However, low SFEs can be observed, such as 5-10% over entire molecular clouds (Williams & McKee 1997), and the size scale over which SFEs are measured can have a major role. Additionally, the extremely low inferred SFE of S26 may result from several factors cannot be discriminated between. The extraction region for the large aperture SED is roughly 35 times the area used to estimate the stellar mass of the cluster, and thus may be including dust and gas beyond the S26 structure. Alternatively, I cannot rule out if S26 is done forming stars or if the massive stars are disrupting or inhibiting further star formation that might be occurring.

2.8 Discussion

It is evident that the massive star cluster S26 in NGC 4449 is emerging from its natal cocoon, as seen through multi-wavelength evidence: 1. thermal radio emission from ionized gas indicative of a young massive star cluster, 2. unique optical features produced by the evolved massive WR stars producing large amounts of mechanical stellar feedback, and 3. strong infrared and PAH emission from a PDR and heated dust surrounding the cluster. Here I investigate physical conditions pertaining to the massive stars within the cluster, which may be driving or contributing to this cluster's emergence from its birth material.

2.8.1 Massive Star Populations of S26 in Context

2.8.1.1 Estimates through STARBURST99

Models and population comparisons may show evolution timescales, metallicity or environmental effects, or deviations from the expected IMF, and thus indicate processes that are affecting the star formation. Using STARBURST99 v7.0.0 (Leitherer et al. 1999), the starburst properties of S26 are modeled by adopting an input metallicity of $Z = 0.008$ (see Section 2.4.2) and simulating an instantaneous burst of star formation. The Geneva evolutionary tracks with high mass loss and Pauldrach/Hillier atmospheres (Smith et al. 2002) are used with a Kroupa IMF. The STARBURST99 models are used to determine the age (Section 2.4.4) and provide an evolutionary comparison for theoretical massive star populations, as shown in Figure 2.7. To produce comparable massive star populations to the observed data, the initial cluster mass is scaled to $6.5 \times 10^4 M_{\odot}$ (Reines et al. 2010) and a mass range in the IMF of 0.1 - $120 M_{\odot}$ is used. The observed WR/O population ratio in the massive star cluster S26 is consistent with these predictions, but is slightly higher than expected, as shown in Figure 2.7. If the age were a little bit larger, this discrepancy would go away. In general, fewer WR stars are expected at low metallicities like S26.

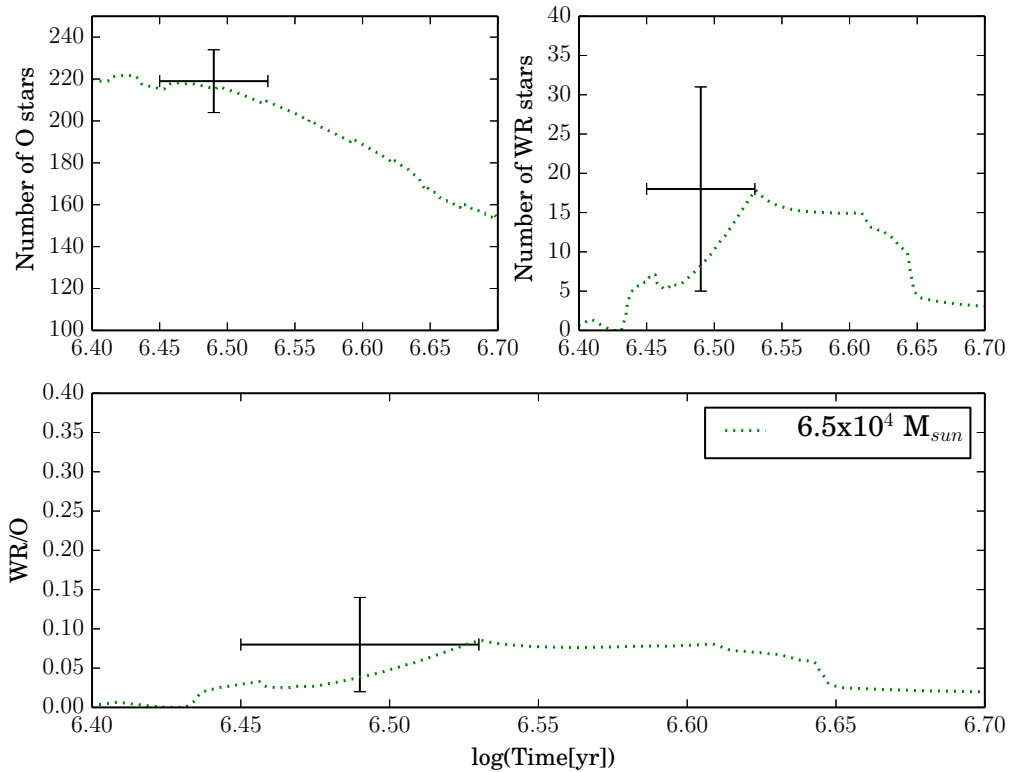


Fig. 2.7.— The estimated age vs. the observed WR and O-star populations, and WR/O population ratio, of the cluster S26 (data points). The evolutionary synthesis model of STARBURST99 (Leitherer 1999), which utilizes a Kroupa IMF with upper and lower limits of $0.1 - 120 M_{\odot}$, is plotted (dotted lines) and further discussed in 2.8.1.1.

2.8.1.2 WR Population Trends with Metallicity

It is necessary to additionally compare the massive star populations of S26 to observations of other regions and models that are in different environments. The number of WR stars, specifically comparisons between the subtype of the WR stars, is heavily dependent on the metallicity. The ratios of WR populations WC/WN and WR/O stars in the local group are observed to roughly decrease with host galaxy metallicity (e.g. Massey 1996). Figure 2.8 shows evolutionary predictions against observational data of nearby galaxies and S26 in NGC 4449. Evolutionary model predictions of the Geneva group are shown, including Meynet & Maeder (2005), for initially rotating

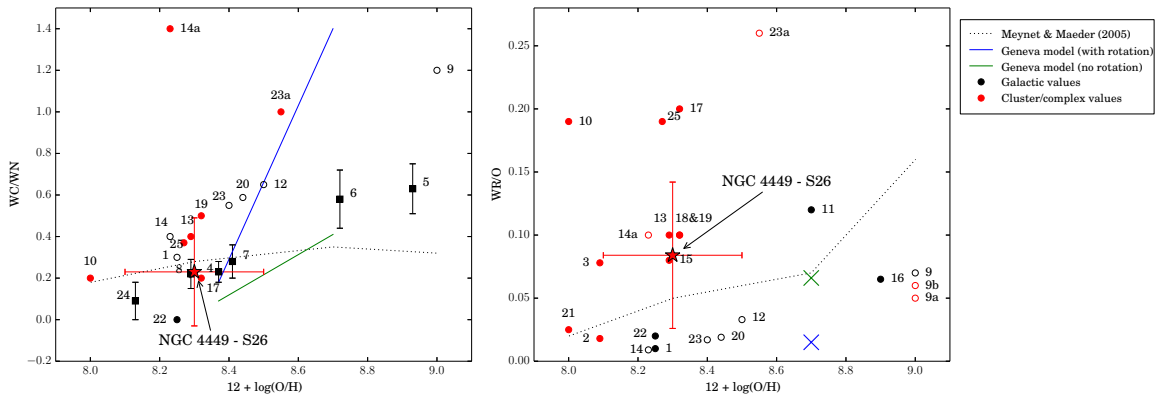


Fig. 2.8.— A compilation of observed population ratios in nearby galaxies compared to different predictions. Star points show the observed ratios in the massive star cluster S26 in NGC 4449. Lines show model predictions of (Meynet & Maeder 2005) (dotted; including stellar rotation) and computed results for new models from the Geneva group (solid) for $Z = 0.006$ (Neugent et al. 2012) and $Z = 0.014$ (Georgy et al. 2012) in blue and green. The symbols roughly indicate the method of determining the populations: squares show individually, spectroscopically resolved populations and circles show ratios similarly measured to this work (open are corrected for completeness). Color version available online. References: 1-IC 10 (Massey & Holmes 2002), 2,3-IC 4662 A1,A2 (Crowther & Bibby 2009), 4-LMC(Neugent et al. 2012), 5-M 31 (Neugent et al. 2012), 6,7,8-M 33 inner, middle, outer (Neugent et al. 2012), 9/9a/9b-M 83/M 83-74/M 83 - 31 (Hadfield & Crowther 2008), 10-Mrk 996 nuclear (Telles et al. 2014), 11-MW (Georgy et al. 2012), 12-NGC 300 (Bibby & Crowther 2010), 13-NGC 1140 (Moll et al. 2007), 14-NGC 1313 (Hadfield & Crowther 2007), 15-NGC 1569 SSCA (González Delgado et al. 1997) (under S26 in WR/O: red filled circle), 16-NGC 3049 (González Delgado et al. 2002), 17,18,19-NGC 3125 A1,A2,B (Hadfield & Crowther 2006), 20-NGC 5068 (Bibby & Crowther 2012), 21-NGC 5253 B (Sidoli et al. 2004), 22-NGC 6822 (Massey & Johnson 1998), 23/23a-NGC 7793/NGC 7793 R34 (Bibby & Crowther 2010), 24-SMC (Neugent et al. 2012), 25-Tol 89 (Sidoli et al. 2006).

single stars, and new results presented in Neugent et al. (2012) for $Z = 0.006$ and Georgy et al. (2012) for $Z = 0.014$, with and without including stellar rotation. Theory predictions are at each metallicity Z to $12+\log(\text{O}/\text{H})$ are converted assuming a simple scaling relation and $12+\log(\text{O}/\text{H})_{\odot} = 8.69$ (Asplund et al. 2009).

Similar plots displaying metallicity trends of WR populations are shown by the surveys from Bibby & Crowther (2010) as well as a very thorough sampling by Neu-

gent & Massey (2011) and Neugent et al. (2012). Here, I compare the inferred stellar populations in S26 to a larger sample of other massive clusters and galaxies found in the literature (references given in the caption of Figure 2.8). In several cases, observational datasets have been evaluated for completeness and/or individual stars have been spectroscopically confirmed as WR stars (e.g. Neugent et al. 2012; Bibby & Crowther 2010).

The inferred subtype WC/WN ratio of S26 roughly agrees with predictions (Fig. 2.8) in the low metallicity cases, especially in the cases that have been corrected for completeness. The observed WC/WN ratio in S26 in NGC 4449 does not appear unusual in comparison to other galaxies.

In contrast to the relatively well-behaved WC/WN ratio, scatter is seen between the WR/O ratio observations and predictions at high WR/O ratios that has received attention in only a few cases. This is rather surprising, as recent comparisons of the observed WR/O ratio to predictions in the solar neighborhood were used to suggest that single star evolution may only account for 60% of WR stars (Georgy et al. 2012). As Figure 2.8 shows, a few observed regions populate an area on the plot of low metallicity yet high WR/O ratios. These values often correspond to SSCs rather than values from integrated regions across galaxies (although the distinction becomes unclear for the smallest galaxies). For instance, points plotted for NGC 3125 and Tol 89 are known intense star-forming regions. There was debate over how high the intensity of the starburst and WR populations in NGC 3125 really are (Schaerer et al. 1999; Chandar et al. 2004; Hadfield & Crowther 2006; Wofford et al. 2014), and in this case the high WR/O ratio was broadly discussed. Tol 89 is one of the brightest known GHRs and has been resolved into individual compact clusters, four of which contain WR clusters (Sidoli et al. 2006). These regions clearly display large WR/O ratios which might then suggest some sort of extreme star formation indicator. Most recently, the unusually high WR/O ratio in NGC 3125-A1 has been interpreted to suggest the upper mass limit of the IMF is $>120 M_{\odot}$ (Wofford et al. 2014). While the massive star cluster S26 in NGC 4449 is observed in the middle of the observed WR/O ratios and within the uncertainties is consistent with predictions, S26 is currently amid regions of intense starburst nature.

2.8.1.3 Additional Considerations

Many assumptions are necessary to estimate massive star populations, each with caveats that could impact the inferred stellar content. First, the O-star and WR estimates would be incorrect if the contamination by Of-stars were underestimated, or if the value of the standard ionizing flux Q_o for any of the subtypes were incorrect or changed. In fact, use of the ionizing flux $Q_o = 10^{48.75}$ from Martins et al. (2005) results in twice the O-star population than that of the canonical value of 10^{49} from Leitherer (1999). Additionally, the age of S26 is important in estimating η_o to correct from an O7V population to the complete O-star population and, even more so, for comparing to the predictions of STARBURST99. Lastly some WR stars can form from binary systems (Georgy et al. 2012), however I compare to models which include only single star evolution tracks as reliable binary tracks are not yet available, which could thus underestimate WR populations at later times. Thus, the inferred populations of both WR and O-stars may be altered with different assumptions, which would alter the interpretation.

While consistent with predictions, Figure 2.7 shows S26 may have a somewhat high WR/O ratio, albeit with large uncertainties. While this discrepancy is not statistically significant, there are many physical scenarios that could explain an offset if real. Firstly, stochastic behavior becomes increasingly important for clusters with masses $< 10^5 M_\odot$ (Fouesneau & Lançon 2010) and S26 is at that limit. A high WR/O ratio could also be produced with a different IMF or a higher upper mass limit than assumed, as in the case of the extreme star formation in NGC 3125 (Wofford et al. 2014). Alternatively, the population ratio could be altered by a multiple burst scenario. Lastly, if S26 has not yet fully emerged from its natal material, some of the stars may be embedded and thus unseen at optical wavelengths. Comparisons of the ionizing flux seen at optical and radio wavelengths show this is unlikely in S26. The optical ionizing flux of S26 is simply estimated through empirical relations from Schaerer & Vacca (1998). Using $H\beta$ at 4861 \AA , the ionizing flux is $Q_0 \sim 180 \times 10^{49}$ photons s^{-1} . The ionizing flux, as measured by the thermal radio emission, can be

determined by

$$Q_{\text{Lyc}} \geq 6.3 \times 10^{52} \left(\frac{T_e}{10^4 K} \right)^{-0.45} \left(\frac{\nu}{\text{GHz}} \right)^{0.1} \frac{L_{\nu, \text{ thermal}}}{10^{27} \text{ erg s}^{-1} \text{ Hz}^{-1}} \text{ s}^{-1}$$

(Condon 1992) is $Q_{\text{Lyc}} \sim (200 \pm 20) \times 10^{49} \text{ s}^{-1}$ at 1.3 cm. The ionizing fluxes agree within the uncertainties, and therefore it is unlikely many O-stars remain embedded.

2.8.2 Impact of the Massive Stars on the Cluster Evolution

2.8.2.1 The Potential Ionized Bipolar Outflow in S26

The morphology of S26 as seen in archival *HST* imaging with narrow band filters centered on the ionized lines of $\text{H}\alpha$, $[\text{N III}]$, and $[\text{O III}]$ suggest that it could be driving an ionized outflow on an intermediate scale, dwarfing individual stellar outflows seen in the Milky Way yet smaller than a galactic outflow. As shown in Figure 2.9, the resolved morphology of the central ionized nebular gas in S26 appears bipolar and is evident in all archival *HST* images taken with ionized gas filters, with a size scale of roughly $1'' \sim 18 \text{ pc}$. The butterfly morphology of S26 most resembles that of bipolar H II regions, which are a type of UCH II according to the modified classification scheme by De Pree et al. (2005). As a class, the kinematics of bipolar H II regions suggest an ionized outflow directed by a central source. S26 appears the most morphologically similar to the Galactic bipolar H II region S106, which is surprising given that S106 spans roughly 0.006-0.009 pc across and is ionized by a single O-star (Churchwell 2002), quite different from the massive stellar populations contributing to the nebula in S26 in NGC 4449. Although vastly different spatial scales, both S26 and S106 display a dark lane that bisects the hourglass nebula. In S106, the dark lane is thought to result from a combination of shadowing and protection of an inner disk and high column-density, warm gas on the edge of the molecular cloud (Simon et al. 2012). However, many factors may contribute to this apparent feature in S26 given its distance and complicated environment.

The intermediate size of possible outflow driven by S26 is quite intriguing if the outflow is confirmed. In the Milky Way, ionized outflows from protostars are com-

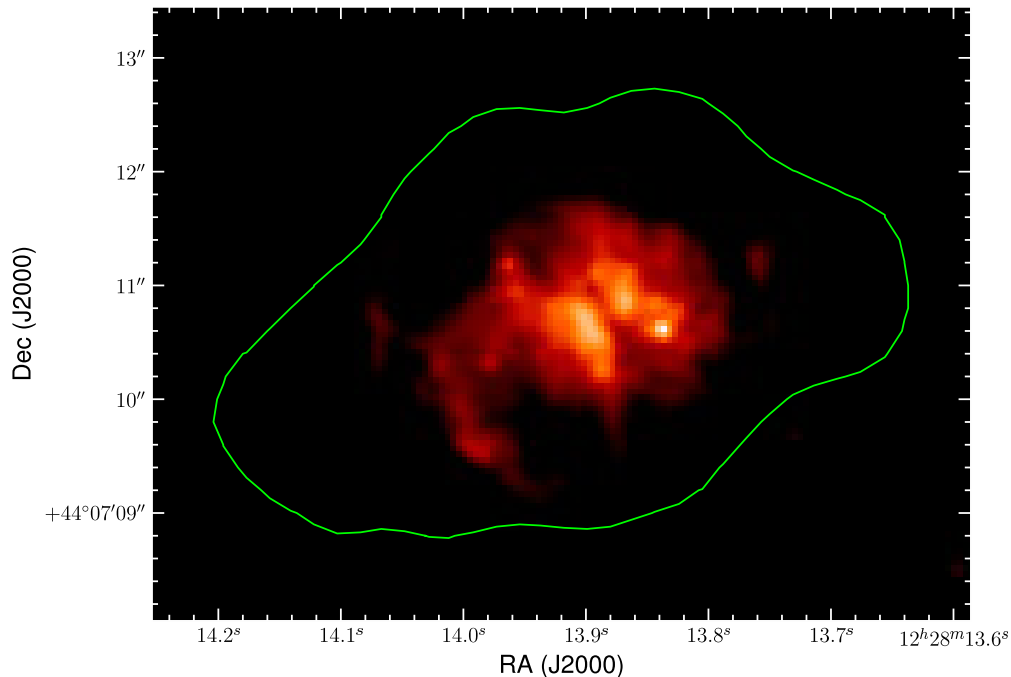


Fig. 2.9.— An *HST* $H\alpha$ image zoomed in on S26, showing the morphology of a bipolar ionized outflow. The green line shows a 3σ contour from 3.6 cm continuum, as in Figure 2.1.

monly on the order of a parsec in size (Bachiller 1996). Alternatively, SSCs may contribute galactic winds or outflows that typically span several kpc yet do not appear as localized as S26. The starburst in NGC 1569, including several SSCs, appears to be driving a (uncollimated) massive outflow seen as diffuse X-ray spurs corresponding to well-known $H\alpha$ filaments with a high-velocity expanding component that is over 2 kpc in size (Heckman et al. 1995). Morphologically, S26 is more similar to the bipolar superwind of M82, possibly driven by dense clustering of SSCs (e.g. Westmoquette et al. 2007), or perhaps the superbubble off the nucleus of NGC 3079 that is 1 kpc in diameter and powered either by an AGN or starburst (Cecil et al. 2001). These outflows are clearly much larger than the ionized region in S26—thus if S26 is a verified bipolar outflow, it may provide insight into potential precursors to, or alternatively failed, galactic winds.

2.8.2.2 The Importance of Winds from Evolved Stars

For some clusters like S26, it may be possible that the mechanical luminosity due to strong stellar winds of an evolved massive star population is the tipping point in the cluster evacuation process. In dense, high-pressure environments, the combination of typical feedback processes from forming stars (such as radiation pressure) may be insufficient to clear a cluster before a supernova. Yet massive stars, on the main sequence and more evolved, could produce the necessary additional mechanical feedback via wind, in combination with the other forms of feedback, to completely clear a cluster prior to a supernova explosion. However to occur before a supernova event, the removal would have to occur over a very short timescale. It is conceivable the enhanced wind phase of evolved stars could drive this evolutionary transition even more efficiently. Thus, perhaps in certain environments, the question is whether the wind mechanical feedback is required, rather than the dominant feedback mechanism, to clear the cluster before a supernova, which will certainly alter the cluster's ability to survive.

Massive stars driving cluster evolution via winds have been observed; Gilbert & Graham (2007) suggest that ELCs are evacuating their surroundings through wind, finding evidence for outflows as the H II gas is not bound. Yet, the extent to which the mechanical luminosity due to stellar winds, particularly those from evolved stars, may contribute has not been fully investigated in the SSC regime, yet it must be substantial. The interaction between the photo-ionized H II region and the stellar wind bubble strongly affect the morphological evolution even in the case of a single massive star (Freyer et al. 2003). Silich & Tenorio-Tagle (2013) show that radiation pressure on a wind-driven shell of a cluster becomes negligible after 3 Myr and highlight the importance of the mechanical feedback.

The first step in answering whether the winds from evolved stars are an essential component in the feedback scheme driving cluster evolution is to investigate if the massive star inhabitants of S26 could fully remove its natal material solely via winds. I compare the binding energy of the initial cluster in S26 and to calculations of the energy input by the massive star population, highlighting the additional boost given

by the evolved WR stars.

I first approximate the binding energy of the cluster as a rough estimate of the energy necessary to remove embedding dust and gas. The region corresponding to the 3.6 cm radio continuum in S26, which includes the nebular emission with the bipolar outflow morphology, is the region being cleared out, called the “core” here. The stellar mass of the core is known (Reines et al. 2010, $6.5 \times 10^4 M_{\odot}$); yet because the dust and gas mass are estimated for S26 over a much larger region, I consider a total core mass produced by a range of SFEs. The total mass in this central region is approximated by including the gas and dust as twice the stellar mass (a roughly 50% SFE) and, closer to what is observed, using a SFE of 5% (Williams & McKee 1997). The resulting binding energy of S26 is $E_{\text{bind}} = 8.8 \times 10^{49}$ erg (10pc/r) to 8.8×10^{51} erg (10pc/r) respectively, where the radius is normalized to a canonical value of 10 pc. Pressure contributions from the outside ISM beyond S26 contribute a negligible energy threshold to overcome when expanding the cluster—however the large surrounding dust and gas mass have not been considered.

The binding energy of the cluster core is compared to the effective energy from the cumulative mechanical luminosity output by the winds from massive stars as $L_{\text{wind}} \sim 0.5 \dot{M} v_{\infty}^2$. A conservative 1% efficiency in the transfer of the mechanical luminosity into the surrounding material, interpreted over integrated O-star lifetimes from simulations of Freyer et al. (2006), is assumed. As S26 is ≈ 3 Myr old and thus the WR phase has likely just begun, a conservative timeframe for the WR phase of S26 is adopted to be the average WR phase of 0.3 Myr for an individual star. I adopt typical O-star characteristics of $\dot{M} = 10^{-6} M_{\odot} \text{ yr}^{-1}$ (Massey 2003) and $v_{\infty} = 2000$ km s $^{-1}$ (Kudritzki & Puls 2000) for an O7V star (along with η_o to estimate the general O-star population, as in Section 2.5.2). Typical WR star mass-loss rates and terminal velocity values of WN7 and WC4 stars from Crowther (2007) are used, and any metallicity effects are treated as in previous sections for the WR stars and as $\dot{M} \propto Z^{0.8}$ for the O-stars (Mokiem et al. 2007).

To first order, assuming a single starburst, S26 may have been completely cleared by the O-star winds alone—although the fact that the cluster is still partially embedded indicates this has not yet happened or suggests the SFE in the core is indeed

low. Over 3.1 Myr, the estimated cluster population of 237 O-stars would contribute 8.8×10^{49} erg through winds. However, 18 of these massive stars have evolved into WR stars, which contribute through much stronger winds. If I account for increased mechanical luminosity for the number of inferred WR stars over the average 0.3 Myr long WR phase of an individual star, the total massive star population would output 9.9×10^{49} erg over the same 3.1 Myr—larger than the binding energy for an initial cluster with a radius of 10 pc with a high SFE. Thus, the massive star population has likely contributed enough mechanical luminosity alone to have fully cleared the cluster, especially when WR contributions are considered. S26 likely has not done so because of the surrounding material or because the SFE is low. I hypothesize the pre-supernova mechanical luminosity is crucial in the evacuation process in this case, especially as the removal is not instantaneous and thus more likely to ensure cluster survival.

2.8.2.3 Describing the Evolutionary Phase of S26

I have examined S26 to investigate this seemingly short-lived yet critical stage in massive/SSC evolution, and I now identify its place among the major classes of H II regions. In Figure 2.10, the observed characteristics of S26 are plotted on the size-density relation of extragalactic H II regions from Hunt & Hirashita (2009). The optically derived density, adopting a size of 50 pc as suggested by the 3σ contour of the 3.6 cm radio continuum that contains the optical cluster, puts S26 among the ELC regions. The two scenarios consistent with the radio data, described in Section 2.6, show that S26 exhibits characteristics similar to both GHRs or UDH IIs, depending on whether the radius is allowed as a free parameter or set at 50 pc. In the context of the evolutionary classification scheme described by Whitmore et al. (2014), S26 lies on the border between Stage 3 (emerging cluster) and Stage 4 (young cluster).

2.8.3 Similarities to 30 Doradus in the LMC

Here, I compare S26 to 30 Doradus in the LMC located at about 50 kpc (Walker 2012), whose dense stellar core R136 is the “prototype” core of a SSC (Massey & Hunter

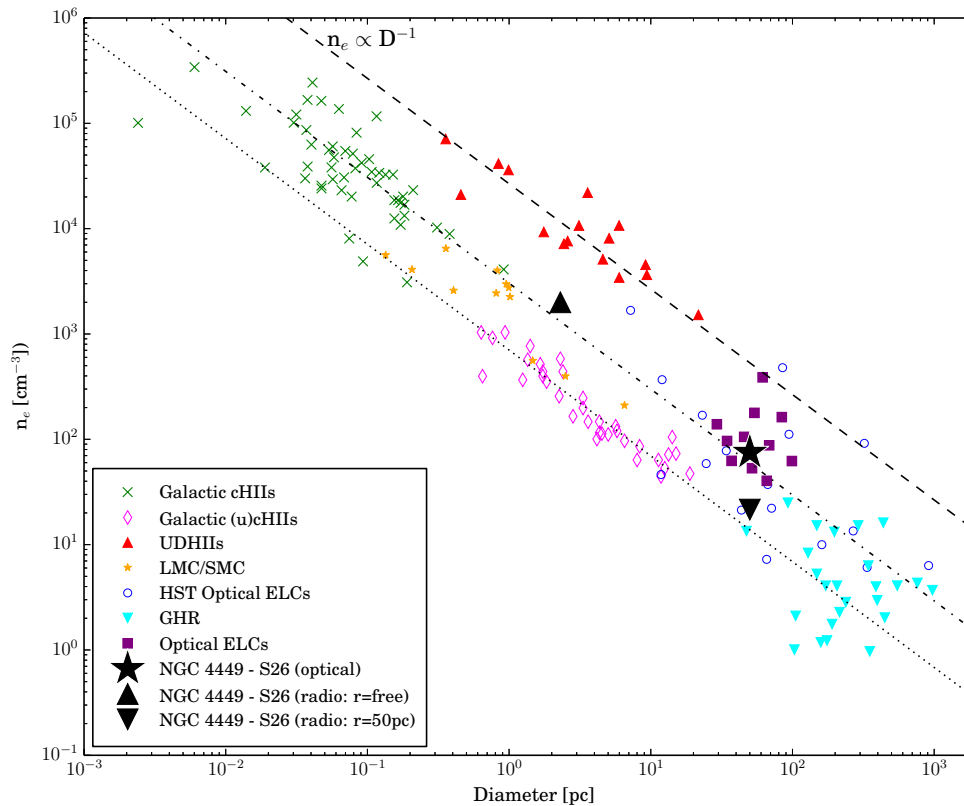


Fig. 2.10.— The optical and radio estimated properties of S26 plotted on the extragalactic H II region size-density relation (Gilbert & Graham 2007; Hunt & Hirashita 2009). As discussed in Section 2.6, the observed radio emission can be modeled with an input radius of 50 pc or with the radius as a free parameter.

1998). In terms of the observed stellar populations, S26 more closely resembles the core R136. The S26 and R136 star-forming regions have almost identical stellar masses ($\approx 6 \times 10^4 M_{\odot}$ Hunter et al. (1995) for R136 and $\approx 6.5 \times 10^4 M_{\odot}$ Reines et al. (2010) for S26). S26 hosts about two times the massive star population: R136 contains ~ 121 massive stars within a 4.7 pc region (Hunter et al. 1995) and S26 hosts 237 massive stars in a region roughly 50 pc in size. Although R136 may be more concentrated, a tight stellar core of S26 may be unresolved (see Figure 2.1). As discussed in Section 2.6, the radio data in S26 are consistent with thermal emission resulting from both a large, low-density region (constraining a spectra fit to a radius of 50pc) or a small,

dense region (2.3 pc; unconstrained radius), and are likely indicative of a low filling factor of high density regions.

However, much of the core of 30 Dor would be unresolved if at the distance of NGC 4449, and thus S26 is compared the entire system as well. Within the total 30 Dor region, the VLT-FLAMES Tarantula Survey found 722 massive stars in a 150 pc radius (of which 500 have been spectroscopically confirmed), resulting in a stellar mass of $1.1 \times 10^5 M_{\odot}$ (Doran et al. 2013) for 30 Dor itself. The scaled stellar mass of S26 is estimated to be $3.0 \times 10^5 M_{\odot}$ in the large 300 pc aperture, which would likewise host ~ 1000 massive stars following the same scaling. Most importantly, 30 Dor contains a remarkably similar gas mass of $(1.3 \pm 0.5) \times 10^7 M_{\odot}$ (Kim et al. 2003) over an aperture of 200 pc, which roughly matches the gas mass of $3 \times 10^7 M_{\odot}$ of S26 with the large aperture of 300 pc.

30 Dor proves an interesting comparison to S26 as it is close enough to resolve individual components and evaluate the impact of the massive star populations on the surrounding environment. Out of the 500 confirmed hot luminous stars in the VLT-FLAMES Tarantula Survey, 31 are WR or Of stars that contribute $\sim 50\%$ of the wind luminosity and $\sim 40\%$ of the ionizing luminosity in the cluster (Doran et al. 2013). This region in 30 Dor roughly corresponds to the size sampled by the small aperture SED of S26 (~ 100 pc), and although the optical spectra were obtained for only the inner 50 pc of S26, the estimated evolved population of 18 WR stars (out of 237 massive stars) is similar. Thus, the wind and ionizing luminosity can be extrapolated from the resolved 30 Dor case and assumed to be just as significant, if not more so, for S26.

Comparing S26 and 30 Dor can shed light on how feedback mechanisms may become relevant, especially later in evolution. Comparisons of the observed pressure due to stellar radiation, shock-heated hot gas, warm ionized gas (H II gas), and dust processed IR radiation indicate that radiation pressure dominates within the central 75 pc region of R136, and H II gas pressure dominates beyond that (Lopez et al. 2011). Another study that paired observations with photoionization models suggests that the hot X-ray gas instead dominates the mechanics of 30 Dor, and that radiation pressure does not currently play a major role in the structure (Pellegrini et al. 2011).

The importance of radiation pressure in at least the initial expansion is clear, however these and many other studies do not directly include mechanical wind feedback from massive stars.

While 30 Dor has undergone a more complicated star formation history and likely undergone multiple bursts of star formation over the last 20 Myr (De Marchi et al. 2011), several parameters of the 30 Dor region parallel those in S26: for one, the gas reservoirs are roughly the same size, stellar feedback is ongoing, and mechanical feedback is largely due to the most massive and evolved stars. The structure of 30 Dor is naturally better defined, with the core hosting 121 massive stars (~ 5 WR stars), with many more in the vicinity, and is consistent with the picture that the most massive stars curtail further star formation (Massey & Hunter 1998). S26 hosts 237 massive stars (18 WR stars) and appears to be undergoing or ending the first star formation event as it is ~ 3 Myr old. Thus, it seems plausible that S26 is a younger version of 30 Dor.

2.9 Summary

I have presented a detailed analysis of the partially embedded massive star cluster S26 in NGC 4449. The main results are as follows:

1. I estimate S26 hosts massive star populations of roughly 18 WR stars and 219 O-stars from optical spectral lines by assuming standard WR optical line fluxes for a single WR star and a typical ionizing flux for an O-star.
2. The massive star population ratio comparing the subtypes WN/WC in S26 is consistent with predictions and other observed clusters and galaxies. The population ratio WR/O is also consistent with predictions. If unavoidably large uncertainties are ignored, S26 is among the high WR/O ratios observed for other individual clusters of intense star formation.
3. Partially embedded by dust, S26 is one of the dominating sources of the IR emission in NGC 4449. The best fit model to the large aperture SED (300 pc

aperture) suggests PAH emission that is stronger than the NGC 4449 galactic value.

4. Dust model fitting to the infrared SED extracted from 100 and 300 pc apertures suggest the exciting radiation increases and PAH emission decreases toward the cluster center. This radial trend suggests the dust grains are being destroyed from within, likely by the massive star feedback.
5. As estimated by the infrared photometry and the best fit model to the large aperture SED, the total dust mass of the S26 structure is $2.3 \times 10^5 M_{\odot}$; by assuming a dust-to-gas ratio of 130, I estimate a gas mass of $3 \times 10^7 M_{\odot}$. This results in a low SFE of 1% over the large 300 pc aperture.
6. I hypothesize that the mechanical luminosity from the evolved stellar winds in S26 may be essential to the emerging process for this cluster, which may ultimately influence future cluster survival. Resolved *HST* images of the ionized gas in S26 display an hourglass nebula, which may suggest a possible bipolar ionized outflow. Simple energy calculations suggest that the winds from massive stars may be sufficient in clearing the cluster (particularly if the SFE is high in the region being cleared). However, as S26 has not been fully evacuated at ~ 3 Myr, the increased feedback contributed by the WR stars may be necessary in clearing out the cluster.
7. The optical characteristics of S26 match those of Emission Line Clusters on the size-density relation of extragalactic H II regions. The radio properties of S26 cannot discriminate between the UDH II and GHR extremes, which may imply a low filling factor of high density regions within a large, low density H II region.
8. Similarities between the S26 cluster and the SSC analog 30 Doradus in the LMC may suggest that S26 is akin to a younger version of 30 Dor.

It is evident that the massive star cluster S26 in NGC 4449 is undergoing an important evolutionary stage in which stellar feedback is particularly important. I propose S26 may be an example of a short-lived, yet important phase in massive and

SSC evolution, during which the complete evacuation of natal material is aided by the mechanical luminosity of the massive stars, particularly evolved WR stars.

Chapter 3

The Prevalence and Impact of Wolf-Rayet Stars in Emerging Massive Star Clusters

3.1 Overview

I investigate Wolf-Rayet (WR) stars as a source of feedback contributing to the removal of natal material in the early evolution of massive star clusters. Despite previous work suggesting that massive star clusters clear out their natal material before the massive stars evolve into the WR phase, WR stars have been detected in several emerging massive star clusters. These detections suggest that the timescale for clusters to emerge can be at least as long as the time required to produce WR stars (a few million years), and could also indicate that WR stars may be providing the tipping point in the combined feedback processes that drive a massive star cluster to emerge. The potential overlap between the emerging phase and the WR phase is explored with an observational survey to search for WR stars in emerging massive star clusters hosting WR stars. Candidate emerging massive star clusters are selected from known radio continuum sources with thermal emission and obtain optical spectra with the 4m Mayall Telescope at Kitt Peak National Observatory and the 6.5m

MMT⁴. I identify 21 sources with significantly detected WR signatures, which are termed “emerging WR clusters.” WR features are detected in $\sim 50\%$ of the radio-selected sample, thus finding that WR stars are commonly present in massive star clusters currently emerging. The observed extinctions and ages suggest that clusters without WR detections remain embedded for longer periods of time, and may indicate that WR stars can aid, and therefore accelerate, the emergence process.

3.2 Background

One of the most stunning early discoveries of the *Hubble Space Telescope* was of star clusters with masses of $10^4 M_{\odot}$ - $10^7 M_{\odot}$, which are quite different than the typical young star clusters in our own Galaxy. These clusters came to be known by a variety of names, including massive star clusters and Super Star Clusters or together they can be also called Young Massive Clusters. Not only can these star clusters dominate the appearance of their host galaxies, but their formation and early evolution can have a significant impact on their environment (Krumholz et al. 2014).

A simple version of the stages of early evolution of a massive star cluster as a scaled up version of a massive star was proposed by Johnson (2002), which starts with the collapse of a massive ($\gtrsim 10^6 M_{\odot}$) molecular cloud, subsequently forming hundreds to thousands of massive stars (e.g., Bonnell et al. 1998; Evans 1999). When star formation begins, the cluster is still heavily obscured and the presence of massive stars is first observable through radio free-free emission arising from ionized gas (e.g., Kobulnicky & Johnson 1999; Turner et al. 2000). The massive stars eventually clear the natal material away from the cluster, enabling the brilliant star cluster to be studied with optical and near-infrared wavelengths.

However, closer inspection of the details in this simplified scheme reveals that both the timescales and the mechanisms at play are not well-constrained. For instance, Sokal et al. (2015a) identified a massive star cluster in NGC 4449 that suggests that the evolution cannot be so cleanly divided into individual stages. This massive star

⁴Observations reported here are obtained at the MMT Observatory, a joint facility of the University of Arizona and the Smithsonian Institution.

cluster, called S26, was originally identified as radio continuum source with a thermal emission component (Reines et al. 2008); yet, surprisingly, was also discovered to host Wolf-Rayet stars (Reines et al. 2010). Wolf-Rayet (WR) stars are the evolved descendants of O-stars ($\gtrsim 25 M_{\odot}$) that have stripped off their outer layers via high mass loss rates (Conti et al. 1983). As only massive stars will become WR stars, the WR phase for a cluster is short, typically occurring at a cluster age of ~ 3 Myr and lasting only a few Myr depending on the stellar populations present. Due to the short WR phase and the feedback nature of the WR stars themselves, the simultaneous presence of the thermal radio emission and the WR stars in S26 in NGC 4449 has important implications for the evolution of young massive star clusters (Sokal et al. 2015a).

One implication is that the lifetime of the thermal radio emission, which typically is observed while a cluster is still embedded in its natal cocoon, may not be as simple and short-lived as expected. Previous work has shown that some of the most massive star clusters can be observed without obscuring natal material or thermal counterparts within a few Myr (e.g., Whitmore & Zhang 2002; Bastian et al. 2014; Hollyhead et al. 2015), which is in agreement with predictions from population studies of embedded thermal sources that suggested a timescale of $\sim 1 - 2$ Myr for emergence (Kobulnicky & Johnson 1999). If the timescales for emergence are indeed as short as a few million years, this would require massive star clusters to typically clear out the embedding natal material before the first supernova has exploded, which for instance should occur at the end of a $60 M_{\odot}$ star's life at 4 Myr (Groh et al. 2014) and at even younger ages for more massive stars. In line with this expectation, WR stars have been observed in a number of optically visible clusters (e.g., Bastian et al. 2014), suggesting the timescale for cluster emergence can be less than ~ 3 Myr. On the other hand, some clusters also in NGC 4449 are observed to stay embedded in natal material for up to 5 Myr (Reines et al. 2008), which could be past the onset of the WR phase. However, S26 in NGC 4449 has provided the first example that, for some massive clusters, there may be a period during which the thermal emission and the WR phase have overlapping timeframes, showing that at least some clusters are not fully emerged by the time the WR stars appear.

Perhaps more importantly, Sokal et al. (2015a) suggest that the WR stars in S26 might be contributing to the evolution of the cluster by helping to clear out embedding material. S26 is in the act of emerging from its natal molecular cloud, with additional evidence for ongoing feedback seen in the infrared spectral energy distribution and optical nebular morphology. However, thus far, the contribution of the additional feedback from WR stars has not been addressed. There are good reasons to suspect that WR stars may be important in how massive star clusters emerge. In general, the relative importance of different feedback mechanisms on the natal material in young massive star clusters and driving the evolution of the H II region is not yet understood (e.g., Lopez et al. 2014). The expansion of the ionized gas likely dominates H II regions driven by single massive stars to massive star clusters, for instance in analytic studies (e.g., Matzner 2002), simulations (e.g., Dale et al. 2005), and observational studies (e.g., in the Large Magellanic Cloud (LMC) by Lopez et al. 2014). However, radiation pressure may also be the dominant feedback mechanism early on (Krumholz & Matzner 2009; Lopez et al. 2011). Stellar winds are thought to be less important energetically in the dynamics of H II regions, as the output energy equivalent to that of a supernova can leak and escape (e.g., Rogers & Pittard 2013). Yet, winds are more efficient than the H II region pressure in removing extremely dense material and in determining the morphology (Dale et al. 2014). In addition, the impact of later supernova is increased by up to a factor of two, if winds have cleared molecular material (Walch & Naab 2015). These details demonstrate that the feedback phase of massive star clusters is complicated, with different mechanisms contributing at different times and interplay between them. It is becoming increasingly clear that stellar winds should not be ignored (Freyer et al. 2003; Calura et al. 2015).

The feedback from many different physical processes may be increased during the WR phase, including these two leading candidates for the dominant feedback process (photoionization and radiation pressure). There might be a slight increase in the luminosity, which would produce more radiation pressure than that from O-stars, during the WR phase for stars with certain initial masses or properties, as follows. The Geneva models at solar metallicity (Ekström et al. 2012) show that non-rotating stars have a higher luminosity during the WNL phase than during their O-star phase

(see Figure 1 in Georgy et al. 2012). If rotating, this only follows for stars with lower initial stellar masses ($\sim 25 M_{\odot}$). At a low metallicity of $z = 0.002$ (Georgy et al. 2013), where a higher initial mass is required to make a WR star through single star evolutionary paths, the stars with initial stellar masses $> 85 M_{\odot}$ exhibit higher luminosities during the WR phase compared to the earlier stages. Observationally, this is hard to test and the findings may not be in agreement with the predictions; as shown in HR diagrams, WC stars in the MW appear below the previously predicted tracks (Sander et al. 2012), and WN stars in the LMC and M31 fall across and below evolutionary tracks (Hainich et al. 2014; Sander et al. 2014). Regardless of the luminosity, the WR winds can cause chemical enrichment (Kehrig et al. 2013), which can lead to greater opacities and a corresponding increase in radiation pressure.

Additionally, the ionizing flux for stars with an initial mass of $60 M_{\odot}$ is increased by an order of magnitude, and more for stars with initial masses less than $60 M_{\odot}$, when they have evolved into the WR phase (at solar metallicity; see Figure 6 in Topping & Shull 2015). Higher ionizing photon rates from WR stars can result in more photoionization in comparison to that produced by O-stars, and thus result in higher ionized gas pressure.

Lastly, WR winds will input roughly ten times the instantaneous energy than O-star winds. But, it is the short lifespan of the WR stars, which is roughly a tenth of the O-stars' lifetime, that has likely led to somewhat ignoring the WR star contributions to the feedback: after all, the integrated energy input by the winds is similar over the lifetime of the O-stars and the WR stars. Yet if there is an increase in feedback during the WR phase, the influence on the environment may be different than that of the previous O-star phase particularly because of the carved out cavities due to the winds. In the same way that the impact of supernova is increased if the region was previously cleared out, the impact of the WR feedback should be increased after the O-star feedback has (very slowly) done its work. Clearly, there is much work to be done to understand the interplay amongst the different feedback mechanisms (Calura et al. 2015), including the WR contributions.

In addition to these possibilities, an inspection of the literature reveals additional massive star clusters other than S26 in NGC 4449 may simultaneously exhibit thermal

radio emission and WR signatures. For example, the irregular blue compact dwarf galaxy NGC 3125 is dominated by two bright star formation regions. The eastern lobe hosts a compact thermal radio source (Aversa et al. 2011), and also shows WR signatures (e.g., Hadfield & Crowther 2006). The unusual supernebulae in NGC 5253, a site of dust enrichment and high star formation efficiency, may be coincident with known WR features as well (Turner et al. 2015). Therefore, these objects may be currently undergoing the same short-lived evolutionary transition as S26 in NGC 4449, and suggest that S26 is not an unique massive star cluster, but in fact may be common.

Here, I follow up the in-depth investigation of S26 with an observational survey to search for WR stars in emerging massive star clusters to assess the role of WR stars in this evolutionary process. WR stars produce high ionization stellar emission lines that are relatively unique to WR stars. Large populations of WR stars produce a broad, integrated spectral features in the optical spectrum known as WR “bumps.” The “blue bump” includes He II at λ 4686 Å and N III/C III at λ 4640/4650 Å, and the “red bump” is due to C IV at λ 5808 Å. I use a novel method to identify emerging massive star clusters, explained in Section 3.3 and obtained optical spectra to look for the WR bumps. The observations are presented in Section 3.4. The sources are classified by presence or absence of a WR bump observed in the optical spectra in Section 3.5, and the environments are characterized in Section 3.6, including nebular properties and massive star populations. The frequency of WR detections in my sample and other results are discussed Section 3.7. Finally, a discussion of timescales and an indication that WR stars may accelerate the emergence of massive star clusters is presented in Section 3.8.

3.3 The Sample Selection: Emerging Massive Star Clusters

In order to ascertain if there are many other massive star clusters that are emerging from their natal material and display WR features, similar to NGC 4449’s S26 (Sokal

et al. 2015a), I select a sample of 45 radio sources in six nearby galaxies known to be starbursts or have high star formation rates. Such galaxies are likely hosts to massive star clusters, and the sample includes both dwarfs and spirals. These galaxies all have previously known radio continuum detections with thermal emission, as indicated by a radio spectral index $\alpha \geq -0.1$. Optically thin thermal free-free emission results in $\alpha = -0.1$, which increases with density (n_e) and can become positive in dense enough conditions. A cutoff of $\alpha > -0.3$ including the uncertainties is used (e.g., Maddox et al. 2007), which allows for the unavoidable large uncertainties in the measured values for α in extragalactic sources; this cut-off will include mixed sources, where thermal free-free emission is contributing but is not necessarily the sole emission mechanism. It is also important to note that while WR stars are known to produce free-free emission in their winds (Wright & Barlow 1975), this emission is not significant in comparison to the H II region. For example Sokal et al. (2015a) shows in the case of S26 with ~ 20 WR stars, any WR contributions to the observed radio emission are negligible.

The properties of the host galaxies, consisting of NGC 2366, NGC 4214, NGC 4449, NGC 6946, and M 51, are listed in Table 3.1. The targets in NGC 2366 and NGC 4214 are selected from Chomiuk & Wilcots (2009), a study originally intended to identify supernova remnants. Using the Very Large Array (VLA), Chomiuk & Wilcots (2009) produce maps at 20, 6, and 3.6 cm with synthesized beams of $3''.7 \times 3''.7$ ($\sim 60 \times 60$ pc) for NGC 2366 and $1''.35 \times 1''.35$ ($\sim 19 \times 19$ pc) for NGC 4214. All discrete radio sources with flux measurements greater than 3σ at 20 cm are identified and cataloged. In total, 3 sources in NGC 2366 and 5 sources in NGC 4214 are included in this sample. Targets in NGC 4449 are from the work of Reines et al. (2008). Reines et al. (2008) mapped NGC 4449 with the VLA at 1.3, 3.6, and 6.0 cm and convolved all data to a synthesized beam $1''.3 \times 1''.3$ ($\sim 24 \times 24$ pc). Radio

Table 3.1. Target Host Galaxies

Galaxy	Morphological Type ^a	SFR ($M_{\odot} \text{ yr}^{-1}$)	Distance (Mpc)	Distance References
NGC 2366	IB(s)m	0.11	3.34	Tully et al. (2013)
NGC 4214	IAB(s)m	0.16	2.93	Tully et al. (2013)
NGC 4449	IBm	0.66	3.82	Annibali et al. (2008)
NGC 6946	SAB(rs)cd	5.65	5.5	Tully (1988)
M 51	SAbc	4.48	7.62	Ciardullo et al. (2002)

Note. — An overview of the basic properties of the host galaxies in this sample. The given distances are used throughout this work. The star formation rates (SFR) are estimated using $H\alpha$ and are from Lee et al. (2009).

^aFrom NED

sources are identified using requirement of a 3σ detection (local rms) minimum in the 3.6 cm image. Of these radio sources, 7 are included in this sample. The studies of Hyman et al. (2000) and Maddox et al. (2007) provide my targets in NGC 6946 and M 51, respectively. Hyman et al. (2000) re-evaluate high resolution ($2''$, roughly 53 pc) observations of NGC 6946 at 6 and 20 cm with the VLA by Lacey et al. (1997). These radio continuum maps reach sensitivities of 16 and 20 $\mu\text{Jy beam}^{-1}$ at 6 and 20 cm. Maddox et al. (2007) produced high resolution images of M 51 with the VLA at 6 and 20 cm. The 6 cm map, with an rms = 11.7 $\mu\text{Jy beam}^{-1}$ has a deconvolved beam of $1''.47 \times 1''.13$ ($\sim 54 \times 42$); the 20 cm map has a deconvolved beam measuring $1''.50 \times 1''.21$ ($\sim 55 \times 45$) and an rms of 22.5 $\mu\text{Jy beam}^{-1}$. From these observations, compact radio sources are identified via a detection algorithm and visual checks. I include 6 sources in NGC 6946 and 24 sources in M 51 in this sample. Although a heterogeneous dataset composed of different catalogs is used to select my targets, all selected studies include a measurement at 6 cm. From here on, I adopt a naming convention based on the original numbered identifications from these published radio catalogs and use Galaxy - Object “ID number” for all sources.

3.4 Observations

Optical spectra of the targets is obtained with the 4m Mayall Telescope at the Kitt Peak National Observatory (National Optical Astronomical Observatory) and the 6.5m MMT at the Fred Lawrence Whipple Observatory to search for WR emission as well as characterize their environments. Target selection is heavily constrained in the observing process by weather, airmass, slit angle, and fiber placement. Only the sources whose signal-to-noise ratio (S/N) in the optical continuum is observed to be ≥ 15 per pixel are included in this sample. An example of the optical spectra of several sources is shown in Figure 3.1. A summary of the spectral observations is presented in the Appendix in Table A1, as well as the spectra of the rest of the sources in the sample that are shown in Figures A1 - A4.

Additionally, archival imaging is used to provide the total V-band flux from each source. Not all observing is photometric while obtaining the optical spectra, but the

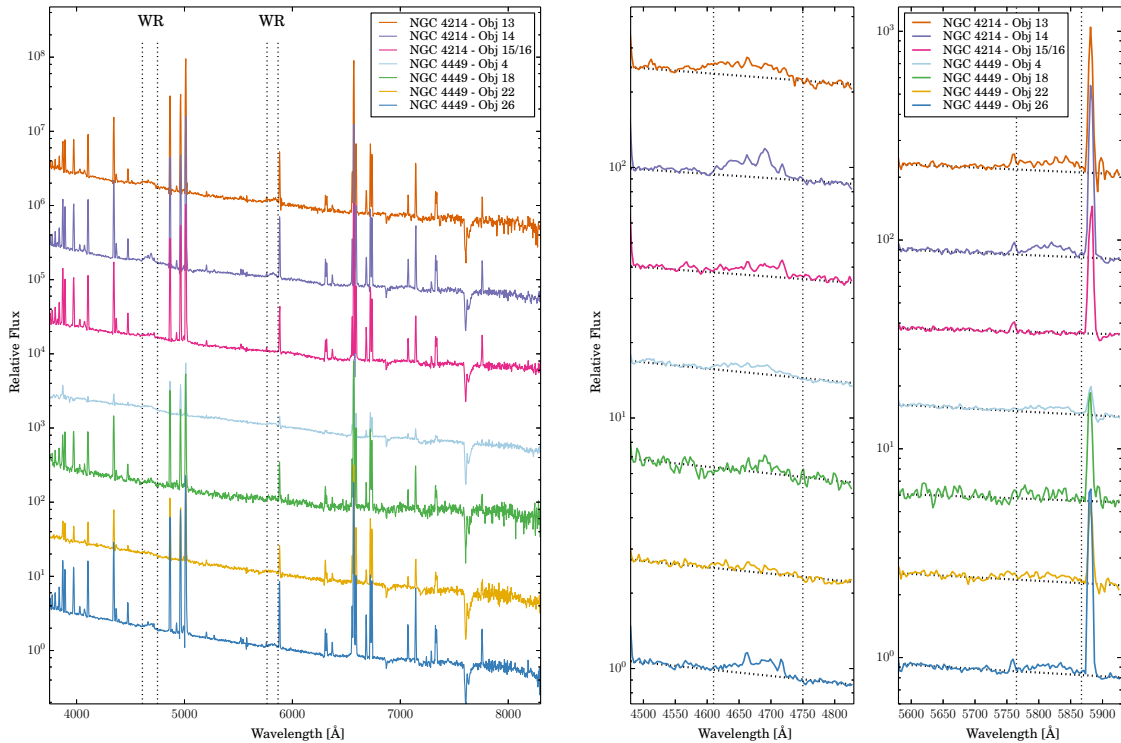


Fig. 3.1.— Optical spectra observed with the 4m Mayall Telescope at KPNO of a subset of the WR clusters. Dashed lines indicate the location of the broad WR bumps, and a zoom in on the WR bumps is shown in the figure on the right, where a roughly traced continuum guides the eye. For ease of visual comparisons, individual spectra are normalized by the average value of the continuum at λ (which is given in Table A3) then offset. The spectra of the rest of the sources in the sample are included in the Appendix.

spectral flux in Section 3.6.2 is corrected using the photometric V-band fluxes.

3.4.1 Optical Spectra

Targets in NGC 2366, NGC 4214, and NGC 4449 are observed with the 4m Mayall Telescope in April 2013; details are presented in Table A1 in the Appendix. Only the optically brightest targets are observed, as the guider was not functioning which led to hand guiding. Each source is observed with a $1''.3 \times 5''.4$ slit aligned at the parallactic

angle and seeing varied from $0''.7$ to $2''.5$. Use of the R-C CCD spectrograph with the KPC-10A grating provides spectra with a resolution of $\sim 6 \text{ \AA}$ over a wavelength range of $3800\text{-}8000 \text{ \AA}$ (with $\approx 0''.69$ per pixel). Exposure times vary for each source, yielding a range of S/N per pixel in the continua of 15 - 40. The data are reduced using standard IRAF routines. Spectra are extracted with a 10 pixel window ($= 6''.9$ on sky), except for NGC 4214 - Object 15/16. The spectra of the targets Object 15 and Object 16 in NGC 4214 can not be separated and thus a wider extraction window of 20 pixels is adopted to get the emission from the combined source (Object 15/16). Spectra are obtained for the spectroscopic standard stars Feige 66, Feige 67, Hilter 600, HZ 44, and Wolf 1346 for flux calibrations.

Targets in M 51 and NGC 6946 are observed with the 6.5m MMT in April 2013 using the multi-object spectrograph Hectospec (Fabricant et al. 2005); details are presented in Table A1 in the Appendix. Individual targets are observed by individual fibers that subtend a diameter of $1''.5$ on the sky, pointed at the coordinates of the observed radio continuum source. Target selection is constrained by fiber positioning, resulting in a random sampling. A 270 line mm^{-1} grating blazed at 5200 \AA resulted in spectra with $\sim 5 \text{ \AA}$ resolution over a wavelength range of $3700\text{-}9000 \text{ \AA}$. A problem with an LED in the instrument led to contamination of many spectra in the $8430\text{-}8445 \text{ \AA}$ region, and thus any of the spectra redwards of 8000 \AA is not included in the analysis. Since there is no blocking filter, light redwards of 8000 \AA is expected to be contaminated by second-order blue light in any event. Optical spectra obtained with Hectospec are reduced using the new version of IDL Hectospec pipeline SPECROAD (Mink et al. 2007), which produced sky-subtracted, variance-weighted co-added spectra. Using IRAF procedures, flux calibration is done with spectra of the standard star HD 192281. To increase the signal consistently, all MMT spectra are smoothed with a box car of 5 pixels to a resolution of $\sim 6\text{-}7 \text{ \AA}$, resulting in S/N per pixel in the continua of 15-50 after smoothing (individual S/N values are listed in Table 3.2).

3.4.2 Optical Archival Imaging

Broad-band and narrow-band images are available for NGC 2366, NGC 4214, NGC 4449, and M 51 in the *Hubble Space Telescope (HST)* archive.¹ These observations, although taken with various instruments for different programs, provide well-resolved comparisons. The sources in this sample in NGC 6946 are not captured in available archival *HST* images, and therefore archival data from the Kitt Peak National Observatory 2.1m Telescope with the CFIM imager originally obtained as ancillary data for the SINGS survey (Kennicutt et al. 2003) are used, in which similar filters are available with lower spatial resolution. Color images (B, I, and $H\alpha$) of the regions surrounding a subset of the sources targeted in this sample are shown Figure 3.2; the rest of the sources of the sample are shown in the Appendix in Figures A5-A6. The V-band observations, used for photometry in this work, are described in the Appendix in Table A2.

3.5 Detecting WR Emission

3.5.1 Identifying the WR Bump

Using the optical spectra, I determine whether a given source exhibits a significant WR feature, and if it is not present, I estimate limits. For all spectra with any excess emission near $\lambda 4686\text{\AA}$ the equivalent width (EW) is measured with the IRAF SPLOT package after subtracting any superimposed nebular features such as nebular He II 4686 \AA or [Fe III] 4658 \AA . The SPLOT task fits with a gaussian, and a single broad bump measurement is used unless the WR bump could be deblended into $\lambda 4640/4650\text{\AA}$ and $\lambda 4686\text{\AA}$ components. Uncertainties are determined through IRAF, which performs a Monte-Carlo simulation of 100 trials resulting in an error estimation including the input rms of the spectrum (measured via SPLOT in several line-free regions of the continuum), and then added in quadrature with an additional

¹ Based on observations made with the NASA/ESA *Hubble Space Telescope*, and obtained from the Hubble Legacy Archive, which is a collaboration between the Space Telescope Science Institute (STScI/NASA), the Space Telescope European Coordinating Facility (ST-ECF/ESA) and the Canadian Astronomy Data Centre (CADM/NRC/CSA).

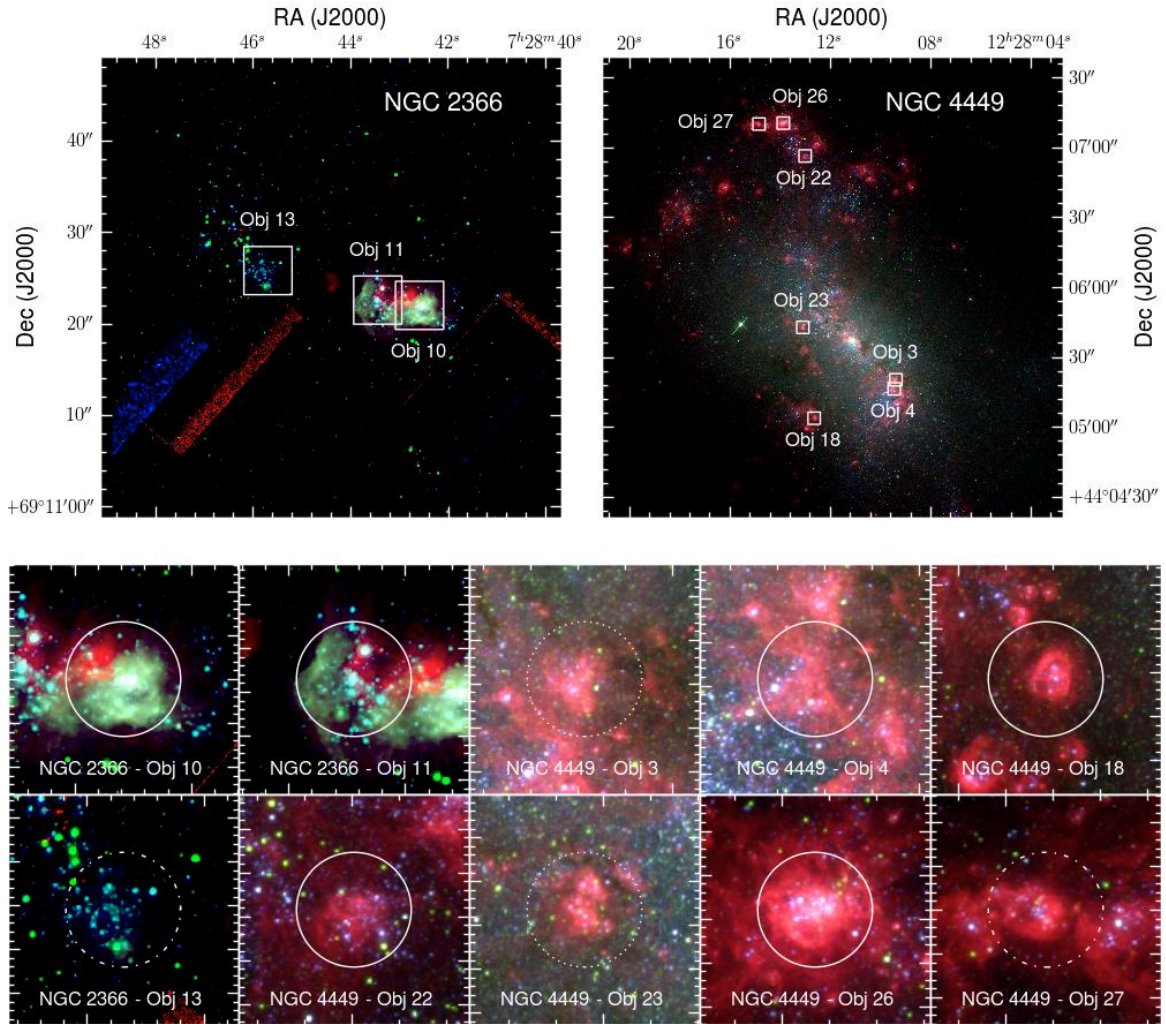


Fig. 3.2.— Archival *HST* images ($H\alpha$, B, I) of the target galaxies NGC 2366 and NGC 4449. Insets are zoomed in on sample sources, with the corresponding region overlaid on the host galaxy image with a white square for ease of comparison. White circles ($2''.5$) are overlaid and show the extraction regions used for photometry. The line style of this overlaid circle indicates the source's classification: solid for WR clusters, dotted-dashed for Candidate clusters, and dotted for Non-WR clusters. Images of the rest of the images in the sample are included in the Appendix.

measurement uncertainty introduced by estimating the continuum. A source is considered to have a significant detection of the WR bump if the S/N_{bump} is ≥ 5 for a single broad bump, or both deblended λ 4640/4650 Å and λ 4686 Å bumps are $S/N_{\text{bump}} \geq 3$.

For sources without a clear detection of the WR bump, an upper limit of the WR emission is found using the measured S/N in the optical continuum. This limit can be estimated as

$$EW_{\text{bump}} < \frac{S/N_{\text{bump}}}{S/N_{\text{cont}}} \times (2 \times \text{RES} \times \text{FWHM}_{\text{bump}})^{0.5}$$

where RES is the spectral resolution and the label “bump” refers to the WR bump. The requirement that $S/N_{\text{bump}} \sim 3$ as above is input, as well as used a $\text{FWHM}_{\text{bump}}$ equal to the minimum value observed in this sample such that $\text{FWHM}_{\text{bump}} \sim 18$ Å. For comparison, nebular lines are observed to have $\text{FWHM} \sim 6$ Å (the same as the spectral resolution). The observed S/N_{cont} is plotted versus EW_{bump} in Figure 3.3 and shows both the data points for the WR clusters and the resulting detection limit. In this figure, the detection limit that would be obtained if the weighted average FWHM for all of the WR clusters is used instead is also plotted. This comparison helps to illustrate that if a given source were to have a bump similar to the sources in the sample that are significantly detected, the expected EW would be even larger than the adopted upper limit. The upper limits and WR emission line measurements are presented for the sample in Table 3.2.

Table 3.2. Classification and the WR Features

Source Name ^a	S/N _{cont}	F(4650 Å)/F(Hβ)	F(4686 Å)/F(Hβ)	F(5808 Å)/F(Hβ)	-EW(4686 Å)	Classification
NGC 2366 - Object 10	45	0.49 (0.25)	0.30 (0.36)	...	1.3 (0.5)	WR
NGC 2366 - Object 11	35	4.37 (0.18)	2.54 (0.29)	1.95 (0.26)	4.6 (1.5)	WR
NGC 2366 - Object 13	35	<1.3	Candidate
NGC 4214 - Object 13	30	9.52 (0.28)	6.31 (0.30)	6.58 (0.26)	8.4 (2.8)	WR
NGC 4214 - Object 14	35	3.35 (0.20)	3.17 (0.15)	2.20 (0.24)	6.3 (1.1)	WR
NGC 4214 - Object 15/16	35	4.22 (0.29)	2.77 (0.26)	...	4.9 (1.3)	WR
NGC 4449 - Object 3	15	<2.9	Non-WR
NGC 4449 - Object 4	30	24.58 (0.24)	33.72 (0.20)	18.09 (0.22)	4.5 (0.9)	WR
NGC 4449 - Object 18	15	5.04 (0.34)	9.05 (0.24)	0.59 (0.40)	13.2 (3.3)	WR
NGC 4449 - Object 22	35	...	13.83 (0.14)	25.16 (0.10)	5.9 (0.9)	WR
NGC 4449 - Object 23	15	<2.9	Non-WR
NGC 4449 - Object 26	30	2.62 (0.09)	1.82 (0.10)	2.17 (0.10)	4.3 (0.5)	WR
NGC 4449 - Object 27	20	<2.2	Candidate
NGC 6946 - Object 13	20	...	9.56 (0.10)	...	17.0 (2.1)	WR
NGC 6946 - Object 37	25	<1.8	Non-WR
NGC 6946 - Object 48	25	...	10.91 (0.15)	...	10.6 (1.7)	WR
NGC 6946 - Object 110	30	3.68 (0.16)	3.36 (0.19)	6.68 (0.17)	4.4 (0.9)	WR
NGC 6946 - Object 115	15	6.25 (0.17)	3.46 (0.17)	6.92 (0.22)	2.5 (0.5)	WR
NGC 6946 - Object 117	35	2.44 (0.10)	8.29 (0.08)	6.79 (0.09)	3.7 (0.4)	WR
M 51 - Object 5	20	<2.2	Candidate
M 51 - Object 6	25	<1.8	Non-WR
M 51 - Object 11	35	<1.3	Non-WR
M 51 - Object 34	30	<1.5	Non-WR
M 51 - Object 39	25	<1.8	Non-WR
M 51 - Object 44	25	<1.8	Non-WR
M 51 - Object 46	55	4.20 (0.10)	2.48 (0.11)	3.26 (0.19)	1.7 (0.2)	WR
M 51 - Object 57	40	1.63 (0.12)	2.90 (0.13)	...	2.8 (0.4)	WR
M 51 - Object 60	25	<1.8	Non-WR
M 51 - Object 63	30	<1.5	Non-WR
M 51 - Object 67	35	<1.3	Non-WR
M 51 - Object 73	35	6.82 (0.18)	7.17 (0.14)	2.20 (0.81)	2.6 (0.4)	WR
M 51 - Object 88	20	<2.2	Non-WR
M 51 - Object 90	25	<1.8	Non-WR
M 51 - Object 92	30	<1.5	Non-WR
M 51 - Object 93	30	<1.5	Non-WR
M 51 - Object 94	35	4.80 (0.09)	5.85 (0.09)	...	4.7 (0.5)	WR

Table 3.2—Continued

Source Name ^a	S/N _{cont}	F(4650 Å)/F(Hβ)	F(4686 Å)/F(Hβ)	F(5808 Å)/F(Hβ)	-EW(4686 Å)	Classification
M 51 - Object 96	25	<1.8	Non-WR
M 51 - Object 97	20	<2.2	Non-WR
M 51 - Object 100	45	6.21 (0.08)	4.92 (0.09)	2.12 (0.19)	3.0 (0.3)	WR
M 51 - Object 101	35	3.09 (0.11)	4.99 (0.10)	3.75 (0.17)	3.1 (0.4)	WR
M 51 - Object 103	35	1.63 (0.20)	3.93 (0.11)	...	3.3 (0.4)	WR
M 51 - Object 105	20	<2.2	Candidate

Note. — A table presenting the source name, the S/N in the continuum of the spectra, the measured or estimated upper limit of the equivalent width (EW; in units of Å) of the WR feature at 4686 Å, and the source classification. If there is insufficient signal to decompose the bump, or for the upper limit estimation, the EW is given for the entire broad bump and listed as 4686 Å.

^aNGC 4214 - Object 3, NGC 4214 - Object 17, and M51 - Object 87 belong in the “Other” class, and not listed further .

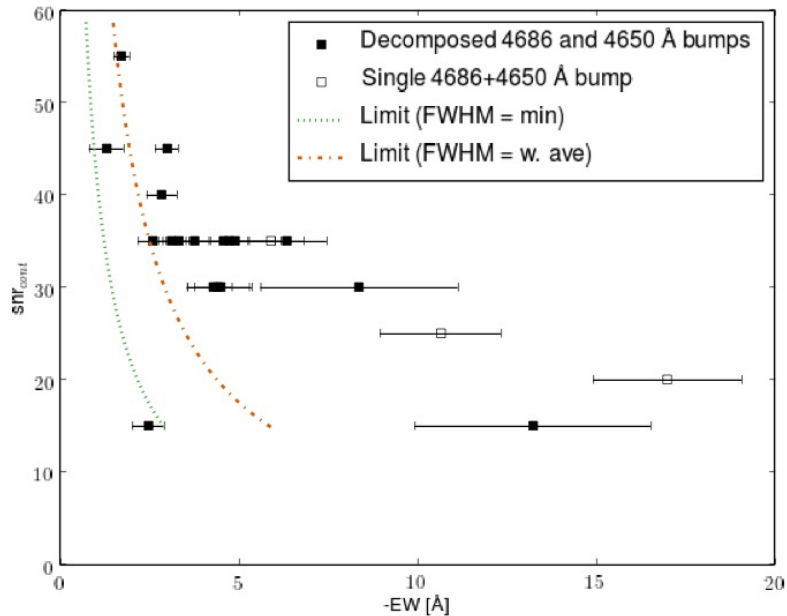


Fig. 3.3.— A scatter plot showing the sensitivity to identifying a significantly detected WR feature. The colored lines are estimated detection limits adopting an observed FWHM of the WR feature from the sample (as indicated in the legend of either the minimum or weighted average) and requiring a 3σ detection.

3.5.2 Classifications According to Observed WR Emission

I classify the sources in this sample according to the detection of the WR bump. The first category is for sources in which the WR bump is significantly detected. As these sources are emerging massive star clusters that clearly host WR stars, similar to S26, I term them “emerging WR clusters” (frequently referred to as “WR clusters” for brevity). For all other sources, I broadly call them “no-bump” sources. Any spectra that are clearly different (not H II regions) or are background objects fall into an “Other” class. “Other” sources are not included further in this work outside of discussing the targeted sample in Figure 3.4. The rest of the no-bump sources appear to be H II regions and thus assumed to be indeed emerging massive star clusters, termed “emerging Non-WR” clusters (similarly, called “Non-WR clusters” throughout). Non-WR clusters include a handful of sources I designate as “Candidate” sources, which appear to have marginal WR bump detections by eye (yet $S/N_{bump} \leq 5$). Applying

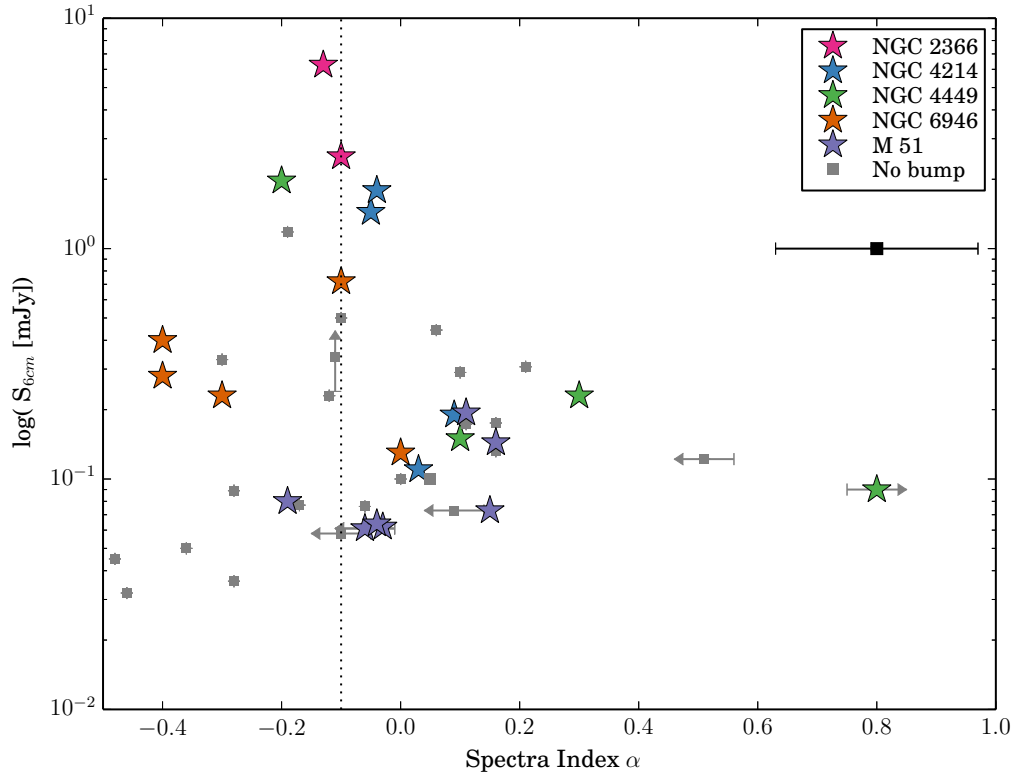


Fig. 3.4.— The radio spectral index α plotted vs. the 6 cm flux density. WR clusters are the star markers color-coded by host galaxy and “No-bump” sources are the gray squares (both Non-WR clusters and Other classes included here). Typical uncertainties are shown by the black marker below the legend box. It is clear that the “No-bump” and WR clusters sample the same parameter space.

this classification scheme, the sample consists of 21 WR clusters, 21 Non-WR clusters (including 4 Candidates), and 3 Other. The classification of individual sources is given in Table 3.2.

3.6 Characterizing the Environments

3.6.1 Photometry

Optical images are used to obtain a total V-band flux measurement of each source, which help characterize the sample and to calibrate the optical spectra. To limit nebular emission contributions, a medium-width filter, such as F550M, is used whenever available. In choosing the extraction apertures, it is apparent that the sources generally reside in complex environments that rarely display a clear boundary, as can be seen in Figure 3.2 and in the Appendix in Figures A5-A6. I adopt a circular aperture with a radius of $2''.5$ centered at the coordinates of the target's radio continuum position, except for NGC 4214 - Object 15/16, which is extracted with a $4''.0$ radius. Aperture photometry is performed with the IDL procedure SURPHOT (Reines et al. 2008), where several background annuli are used and the resistant mean and mode are taken to estimate the background value. The uncertainties are dominated by background subtraction and are found by the standard deviation of fluxes calculated using these different background estimates. The raw luminosities are presented in the Appendix in Table A3. I find the WR clusters and the Non-WR clusters have similar raw luminosity distributions (see Figure 3.5).

3.6.2 Nebular Emission Line Measurements and Corrections

The emission line strengths of the nebular lines are measured in order to determine the interstellar extinction, the optical ionizing flux, and the metallicity. Emission line measurements are obtained using the IRAF SPLOT package and are presented in the Appendix in Tables A4 and A5. Reddening corrections are determined with interstellar extinctions derived from the Balmer line ratios (discussed in Section 3.6.3.1). In addition to the measurement uncertainties (as in Section 3.5.1), uncertainties in the flux are estimated by including the uncertainty in the flux calibration fit and the uncertainty in the reddening correction. High extinctions limited the measurement of the nebular emission lines for many of the Non-WR sources, and thus I do not present measurements for these objects. Zero-point flux corrections, accounting for

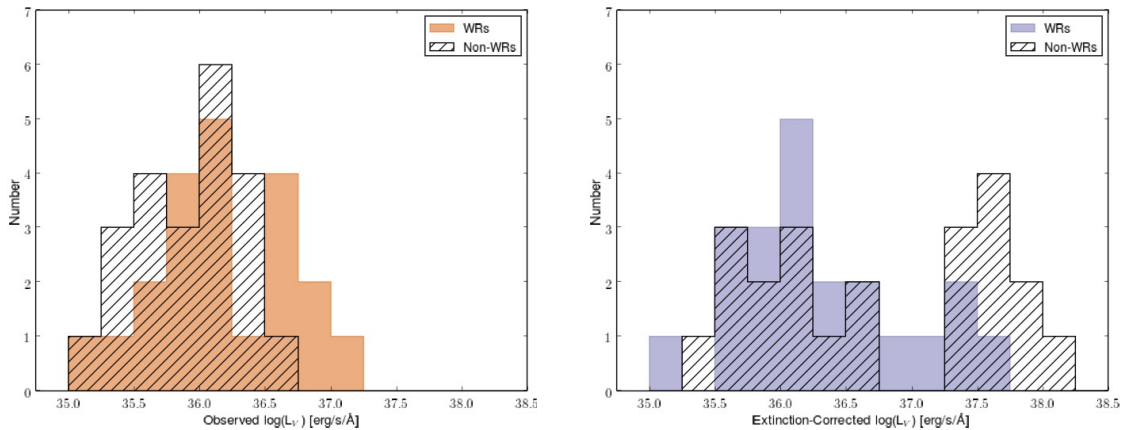


Fig. 3.5.— Histograms of the V-band photometric luminosity of the sample. Colors indicate the WR cluster class, and the black hatches indicate the Non-WR clusters. Left: the raw (observed) luminosity distribution of both classes is similar. Right: the extinction-corrected (intrinsic) luminosity distribution shows some differences between sources with and without WR stars, highlighting that some of the Non-WR clusters exhibit higher extinctions and thus are intrinsically brighter.

non-photometric conditions as well as slit corrections, are made by comparing the V-band flux (see Section 3.6.1) to the total spectral flux in the relevant filter band-pass and listed in Table A3 (in the Appendix). Many sources do not require a flux correction or only minimal adjustment is necessary.

3.6.3 Nebular Properties

3.6.3.1 Interstellar Extinction

Measuring the interstellar extinction for a source provides not only a way to correct the raw flux measurements, but also is a valuable intrinsic property of the environment of the source as well. The interstellar extinction of individual sources are determined using the optical nebular Balmer line ratios of $H\alpha$, $H\beta$, $H\gamma$, and $H\delta$. The observed Balmer decrement is converted to A_V via the extinction curve for the SSC analog 30 Doradus of the LMC (Misselt et al. 1999; Fitzpatrick 1985), and the average weighted A_V is adopted for each source. The use of a Milky Way extinction curve produces similar results, and as these extinction curves are roughly parallel over the

optical regime (De Marchi & Panagia 2014), reddening corrections applied to the measured emission lines follow the same wavelength dependence. Additionally, the extinctions measured with the 30 Doradus extinction curve are, on average, roughly 0.9 times the extinctions derived with the Milky Way extinction curve, and thus the extinctions adopted in this work may be slightly underestimated. However, the results and interpretation of this work are robust to a moderate increase in extinction. For example, the line ratios remain the same (as the extinction curve for the 30 Dor extinction curve and the Milky Way extinction curve are parallel). The line fluxes, and properties derived from the line fluxes, may be increased by up to 5% for $A_V \leq 0.5$, 10% for $A_V \leq 1.0$, and 20% for $A_V \leq 2.0$, which would result in higher inferred ionization fluxes, and therefore also larger cluster masses. However, the conclusions of this work are relatively unaffected by the choice of extinction curve. If the extinction is measured to be negative, the adopted extinction is zero. The available Balmer lines are used in the case that a source is without the complete Balmer series suite. The derived interstellar extinctions are given in Table 3.3.

3.6.3.2 Ionized Gas Density and Temperature

The ionized gas conditions of WR sources are determined using the nebular emission line ratios. To determine the electron density and temperatures in the ionized gas, I utilize the NEBULAR package in IRAF, which uses the five-level atom model (De Robertis et al. 1987). The electron density is estimated using the S II line ratio $6716\lambda/6731\lambda$. The electron temperatures are given by: O⁺ electron temperature (T(O II)) is measured using the [O II] ratio $(3727\lambda/(7319\lambda+7330\lambda))$, and O⁺⁺ electron temperature (T(O III)) is measured using the [O III] ratio $(4959\lambda+5007\lambda)/4363\lambda$. The results are presented in Table 3.4; the densities and temperatures of the WR clusters are typical for extragalactic H II regions (Hunt & Hirashita 2009).

3.6.3.3 Metallicity

Massive stellar evolution is sensitive to metallicity, in part due to the dependence of mass-loss on metallicity (Vink & de Koter 2005; Crowther & Hadfield 2006; Hainich

Table 3.3. Source Properties

Source	A_V mag	Age Myr	$Q_o(H\beta)$ 10^{49} photons s^{-1}	$Q_o(\text{Radio})$ 10^{49} photons s^{-1}	$L_{V,i}$ erg s^{-1}	Mass M_\odot
NGC 2366 - Object 10	0.0	2.0 (0.6)	165.8 (14.2)	505.5 (50.7)	1.7e+36 (2.9e+34)	4.1e+04
NGC 2366 - Object 11	0.1	3.2 (0.7)	63.3 (7.9)	210.3 (21.8)	9.3e+35 (2.3e+34)	1.2e+04
NGC 2366 - Object 13	0.0	4.2 (0.2)	9.8 (0.8)	22.8 (3.0)	2.3e+35 (3.3e+34)	5.0e+03
NGC 4214 - Object 13	0.0	3.3 (0.6)	17.5 (2.2)	8.3 (2.4)	3.6e+35 (4.7e+34)	5.8e+03
NGC 4214 - Object 14	0.0	2.9 (0.5)	28.9 (4.1)	105.2 (12.4)	3.6e+35 (4.5e+34)	4.8e+03
NGC 4214 - Object 15/16	0.0	2.8 (0.0)	41.9 (4.2)	69.5 (8.5)	9.7e+35 (1.3e+35)	1.3e+04
NGC 4449 - Object 3	0.1	3.7 (0.5)	15.2 (5.6)	42.8 (6.7)	4.9e+35 (1.6e+35)	8.6e+03
NGC 4449 - Object 4	0.2	8.0 (0.3)	12.5 (2.4)	22.3 (4.5)	1.8e+36 (1.8e+35)	5.4e+04
NGC 4449 - Object 18	0.0	3.4 (0.3)	11.3 (1.1)	10.4 (1.0)	1.4e+35 (3.5e+34)	2.4e+03
NGC 4449 - Object 22	0.1	5.3 (0.2)	8.8 (1.7)	14.2 (4.0)	7.6e+35 (8.5e+34)	1.4e+04
NGC 4449 - Object 23	0.2	10.0 (0.0)	0.5 (0.1)	64.8 (10.1)	6.1e+35 (2.9e+35)	3.1e+04
NGC 4449 - Object 26	0.1	3.0 (0.4)	106.3 (9.2)	258.8 (26.4)	1.6e+36 (7.3e+34)	3.1e+04
NGC 4449 - Object 27	0.0	4.5 (0.1)	7.8 (7.6)	37.6 (6.4)	3.6e+35 (1.2e+34)	9.6e+03
NGC 6946 - Object 13	0.7	2.8 (0.3)	14.5 (4.3)	123.8 (22.3)	3.3e+37 (7.6e+35)	6.8e+05
NGC 6946 - Object 37	1.2	4.4 (0.3)	4.8 (2.5)	26.9 (6.0)	2.0e+37 (1.4e+35)	5.9e+05
NGC 6946 - Object 48	0.5	2.9 (0.7)	9.6 (2.9)	38.9 (5.7)	1.4e+37 (2.7e+35)	2.8e+05
NGC 6946 - Object 110	0.3	2.3 (0.2)	22.0 (6.4)	187.6 (28.0)	1.9e+37 (8.9e+35)	4.0e+05
NGC 6946 - Object 115	0.1	3.1 (0.2)	11.0 (2.0)	48.3 (13.5)	6.8e+36 (3.2e+35)	1.4e+05
NGC 6946 - Object 117	0.2	5.0 (0.1)	15.1 (3.5)	25.6 (10.2)	2.1e+37 (8.0e+35)	6.1e+05
M 51 - Object 5	0.0	2.9 (0.2)	17.3 (1.6)	37.6 (9.5)	1.1e+36 (2.4e+34)	2.3e+04
M 51 - Object 6	0.8	4.2 (0.1)	16.7 (4.0)	16.5 (6.9)	5.4e+36 (5.8e+35)	1.2e+05
M 51 - Object 11	0.0	4.3 (0.2)	9.8 (0.8)	31.4 (7.4)	1.2e+36 (1.4e+35)	3.2e+04
M 51 - Object 34	1.2	6.4 (0.0)	11.7 (5.1)	62.9 (8.1)	3.9e+37 (1.8e+36)	1.2e+06
M 51 - Object 39	1.2	6.4 (0.0)	38.4 (19.4)	68.1 (8.9)	6.8e+37 (3.4e+36)	2.2e+06
M 51 - Object 44	0.6	2.9 (0.8)	26.9 (9.0)	89.2 (10.6)	7.9e+35 (1.1e+35)	1.6e+04
M 51 - Object 46	0.0	2.9 (0.0)	103.4 (9.2)	46.7 (9.5)	4.0e+36 (3.0e+35)	8.2e+04
M 51 - Object 57	0.3	2.8 (0.2)	10.5 (2.5)	24.8 (5.8)	4.1e+35 (1.6e+35)	8.3e+03
M 51 - Object 60	1.2	6.5 (0.0)	9.1 (1.3)	23.2 (6.1)	3.4e+37 (1.6e+36)	1.1e+06
M 51 - Object 63	1.7	6.5 (0.0)	38.9 (9.8)	18.6 (5.5)	1.4e+38 (2.4e+36)	4.5e+06
M 51 - Object 67	1.8	6.5 (0.0)	16.5 (3.2)	45.9 (6.9)	7.2e+37 (2.9e+35)	2.3e+06
M 51 - Object 73	0.0	4.2 (0.1)	20.7 (8.6)	29.5 (6.6)	2.1e+36 (8.6e+34)	4.8e+04
M 51 - Object 88	1.5	6.3 (0.0)	10.4 (2.7)	39.7 (6.9)	2.0e+37 (4.7e+35)	1.2e+06
M 51 - Object 90	1.8	6.3 (0.0)	18.2 (4.8)	158.3 (17.0)	2.8e+37 (3.4e+35)	9.2e+05
M 51 - Object 92	0.1	4.3 (0.3)	14.9 (3.3)	39.2 (7.8)	2.1e+36 (1.2e+35)	5.9e+04
M 51 - Object 93	0.7	5.0 (0.2)	11.2 (2.3)	29.9 (6.4)	4.8e+36 (6.4e+34)	1.2e+05
M 51 - Object 94	0.0	2.8 (0.1)	25.9 (7.9)	23.1 (4.7)	1.1e+36 (1.6e+34)	2.2e+04
M 51 - Object 96	1.9	10.0 (0.4)	1.4 (0.3)	25.8 (6.2)	2.3e+37 (2.4e+35)	1.7e+06
M 51 - Object 97	1.2	4.2 (0.1)	77.1 (28.5)	228.4 (23.7)	4.4e+37 (9.2e+35)	1.0e+06
M 51 - Object 100	0.0	3.0 (0.1)	303.1 (23.6)	68.9 (8.3)	4.2e+36 (1.1e+35)	8.5e+04
M 51 - Object 101	0.0	3.0 (0.1)	18.3 (1.5)	17.2 (3.9)	1.6e+36 (1.5e+35)	3.2e+04
M 51 - Object 103	0.2	3.0 (0.2)	12.8 (3.0)	47.8 (8.5)	1.1e+36 (2.0e+35)	2.2e+04
M 51 - Object 105	0.7	2.2 (0.1)	9.6 (4.0)	90.2 (11.9)	5.0e+35 (3.2e+34)	9.8e+03

Note. — For each emerging massive star cluster in this table the following is listed: the interstellar extinction as measured by Balmer lines, the age estimated by the equivalent width of $H\beta$, the ionizing flux as inferred from $H\beta$ and thermal radio emission, the intrinsic extinction-corrected luminosity, and the stellar mass.

Table 3.4. Nebular Properties of the WR Clusters

Source	n_e cm^{-3}	T([O II]) 10^4 K	T([O III]) 10^4 K	12+log(O/H)	z
NGC 2366 - Object 10	512 (264)	1.3 (0.3)	1.6 (0.1)	7.9 (0.1)	0.002
NGC 2366 - Object 11	32 (300)	1.7 (0.1)	1.4 (0.1)	7.9 (0.1)	0.003
NGC 4214 - Object 13	76 (134)	1.1 (0.1)	1.0 (0.1)	8.4 (0.2)	0.008
NGC 4214 - Object 14	111 (158)	1.2 (0.2)	1.1 (0.1)	8.2 (0.2)	0.005
NGC 4214 - Object 15/16	50 (66)	1.2 (0.1)	1.2 (0.1)	8.2 (0.1)	0.005
NGC 4449 - Object 4	75 (355)	1.5 (0.3)	1.9 (0.3)	7.9 (0.3)	0.002
NGC 4449 - Object 18	50 (27)	1.0 (0.1)	1.3 (0.1)	8.5 (0.2)	0.009
NGC 4449 - Object 22	22 (128)	1.2 (0.2)	2.0 (0.3)	8.3 (0.4)	0.006
NGC 4449 - Object 26	157 (131)	1.1 (0.1)	1.0 (0.0)	8.5 (0.1)	0.008
NGC 6946 - Object 13	49 (270)	1.5 (0.4)	0.7 (0.1)	9.0 (0.2)	0.032
NGC 6946 - Object 48	557 (1070)	1.9 (0.0)	4.3 (4.1)	9.3 (0.2)	0.062
NGC 6946 - Object 110	101 (332)	1.8 (0.2)	1.1 (0.1)	9.1 (0.2)	0.039
NGC 6946 - Object 115	15 (249)	1.3 (0.3)	1.7 (0.2)	9.1 (0.1)	0.035
NGC 6946 - Object 117	496 (771)	1.1 (0.7)	2.0 (0.4)	8.9 (0.1)	0.023
M 51 - Object 46	129 (107)	1.0 (0.1)	0.4 (0.0)	9.1 (0.4) ^a	0.040 ^a
M 51 - Object 57	152 (285)	1.0 (0.3)	1.7 (0.3)	9.1 (0.1)	0.037
M 51 - Object 73	115 (711)	0.9 (0.4)	2.1 (1.2)	9.2 (0.2)	0.043
M 51 - Object 94	44 (282)	0.7 (0.1)	3.0 (1.6)	9.4 (0.2)	0.066
M 51 - Object 100	149 (90)	0.9 (0.1)	2.3 (0.1)	9.5 (0.1)	0.092
M 51 - Object 101	89 (90)	0.7 (0.1)	4.3 (0.7)	9.3 (0.1)	0.060
M 51 - Object 103	60 (176)	1.0 (0.2)	2.7 (0.8)	9.1 (0.1)	0.039

Note. — This table presents the electron density, electron temperatures, and metallicity measured for the WR clusters.

^aAn approximate metallicity adopted for this source.

et al. 2015). This results in a well-known trend for a decrease in the ratio of WN to WCs with decreasing metallicity. Therefore determining the metallicity is crucial for understanding these sources, especially as this sample spanned a wide range of environments. Because certain oxygen lines become faint at high metallicity, different methods are necessary to estimate the metallicity of each source throughout the sample.

The most accurate method, known as the T_e or “direct method,” is used for all WR sources in the galaxies NGC 2366, NGC 4214, and NGC 4449 (low to moderate metallicity environments). The T_e method used two distinct temperature zones in the photoionized H II region using the O^+ and O^{++} electron temperatures (Izotov et al. 1994, 1997). The IRAF package NEBULAR is used to measure ionic abundances, with the appropriate electron temperature. The O^+ ionic abundance is measured with ionic abundances of 3727λ and the doublet $7319/7330\lambda$, and O^{2+} ionic abundance is determined using ionic abundances for the lines 4363λ , 4959λ , and 5007λ . The total oxygen abundance is then derived by $O/H = O^+/H^+ + O^{++}/H^+$.

For WR sources in galaxies NGC 6946 and M 51, which lied on the so-called “upper branch” where $\log([N II]/[O II]) > -0.8$ (van Zee et al. 1998), a strong line method is adopted. Certain strong nebular emission lines are easily observed and used to find the parameters

$$R3 = \frac{[O III] 4959 \text{ \AA} + [O III] 5007\text{\AA}}{H\beta}$$

and

$$R2 = \frac{([O II] 3727 \text{ \AA} + [O II] 3729 \text{ \AA})}{H\beta}.$$

To estimate the metallicity using the R3 and R2 parameters, I adopted the method of Kobulnicky & Kewley (2004) (often called the KK04 method) in which the oxygen abundance is found iteratively. The metallicity (z) is found using the variables $x = \log(R2+R3)$ and $y = \log(\frac{R3}{R2})$ and the relations

$$\log(q) = \frac{32.81 - 1.153y^2 + z \times (-3.396 - 0.025y + 0.1444y^2)}{4.603 - 0.3119y - 0.163y^2 + z \times (-0.48 - 0.0271y + 0.02037y^2)}$$

and

$$z = 9.72 - 0.777x - 0.951x^2 - 0.072x^3 - 0.811x^4 - \log(q) \times (0.0737 - 0.0713x - 0.141x^2 + 0.0373x^3 - 0.058x^4)$$

(Kobulnicky & Kewley 2004).

Conversely, the purpose of identifying approximate metallicities of the Non-WR clusters is for later comparisons to STARBURST99 models. Additionally, the necessary nebular emission lines to measure the metallicity are not observed for many of the Non-WR clusters. As such, I choose the best match of available metallicity models as approximately averaged by the WR clusters in the same host galaxy. This approximate metallicity is also adopted for one WR source, M 51 - Object 46, as the derived metallicity is unphysical, which is attributed to relatively weak oxygen line emission.

All derived and adopted metallicities are listed in Table 3.4. For both methods, I convert between metallicity z and $12+\log(\text{O}/\text{H})$ by assuming a simple scaling relation and the solar metallicity value $12+\log(\text{O}/\text{H})_{\odot} = 8.69$ (Asplund et al. 2009).

3.6.4 Estimating the Ionizing Flux

Ionizing photons are produced by the massive stars that are harbored in the clusters in the sample. If it is assumed that all ionizing (Lyman) photons are absorbed by hydrogen atoms, the so-called Case B approximation, then every ionization results in a recombination that produces a Balmer photon. Thus with the Case B assumption, the measured $\text{H}\beta$ flux can be used to infer the ionizing flux. However, this optical light can be obscured, causing the inferred ionizing flux to be underestimated. The ionizing flux can also be inferred from radio free-free emission, which would be unaffected by such extinction. While the optical interstellar extinction is measured in Section 3.6.3.1 and is an important component to understanding the nebular environment of the source, using nebular lines has the caveat that it only measures extinction toward gas that is not very heavily extinguished. As such, characterizing the ionizing flux

inferred from both the radio and the optical data provides the opportunity to reveal optically obscured ionized gas, which could not be identified with optical spectra alone; therefore, I calculate the ionizing flux estimated from both radio and optical methods.

The ionizing flux inferred from the optical emission is estimated through the empirical relations presented in Schaerer & Vacca (1998) using the emission line flux of $H\beta$ as

$$Q_{\text{o, H}\beta} \sim L_{H\beta}/4.76^{-13} \text{ phot s}^{-1}.$$

The ionizing flux inferred from radio wavelengths can be found by

$$Q_{\text{o, radio}} \geq 6.3 \times 10^{52} \left(\frac{T_e}{10^4 K}\right)^{-0.45} \left(\frac{\nu}{\text{GHz}}\right)^{0.1} \frac{L_{\nu, \text{thermal}}}{10^{27} \text{ erg s}^{-1} \text{ Hz}^{-1}} \text{ s}^{-1} \text{ (Condon 1992)}.$$

As a radio flux measurement at 6 cm is available for the entire sample, it is used here although higher frequencies will include less non-thermal contributions if they are available. I input the O^{++} temperatures derived for the WR clusters (see Section 3.6.3.2) and an effective temperature of 10^4 K, the approximate average of the estimated temperatures, for the Non-WR cluster class. Of note, both the radio and optical inferred ionizing fluxes are typically considered to be lower limits if dust is absorbing ionizing photons or there is ionizing photon leakage. I list the ionizing flux inferred from both the optical and radio data in Table 3.3.

3.6.5 Fundamental Properties and STARBURST99 Models

I present here both the fundamental properties of intrinsic luminosity, stellar mass, and age of the sample as well as stellar population synthesis models of STARBURST99 (Leitherer et al. 1999, 2014). These properties provide the basis for much of the analysis in this study, and the age and mass are found using the predictions of the STARBURST99 models at a given metallicity.

The intrinsic V-band luminosities are determined by correcting the observed raw V-band photometry for the optical extinction (Section 3.6.3.1); these are presented in Table 3.3. Figure 3.5 shows that extinction-corrected luminosity distributions are

not the same for the WR and Non-WR classes, in contrast to the observed luminosity distributions. Several of the Non-WR clusters have high extinctions that result in higher intrinsic luminosity compared to similar observed luminosity.

To estimate the age of each cluster, I use predictions from the stellar population synthesis models of STARBURST99 (Leitherer et al. 1999, 2014), which simulate a simple starburst of a given metallicity. The presence of thermal radio emission suggests that these sources are quite young, and therefore it is assumed that there is an instantaneous burst of star formation. STARBURST99 v7.0.0 (Leitherer et al. 2014) is run for the four different metallicity tracks ($z = 0.004, 0.008, 0.020,$ and 0.040) that most closely matches the metallicity of the host galaxies of the sample—these are also the metallicities that are adopted for the Non-WR clusters as described in Section 3.6.3.3. I adopt a Kroupa IMF (Kroupa 2001) with mass limits of $0.1 - 120 M_{\odot}$, using Geneva evolutionary tracks (single-star tracks) with high mass loss and Pauldrach (WM-Basic)/Hillier (CMFGEN) atmospheres (Pauldrach et al. 1998; Hillier & Miller 1998, 1999; Smith et al. 2002) for each STARBURST99 run.

The age of each source is estimated by comparing the measured equivalent width of $H\beta$ to that predicted by the STARBURST99 model with the appropriate metallicity track. Uncertainties are from the uncertainty of the measured equivalent width. In Figure 3.6, the resulting ages are plotted against the STARBURST99 predictions. Throughout this work, the appropriate STARBURST99 model for each individual source is identified with this estimated age and metallicity track. Because it is more realistic to assume that there may be binary stars within each cluster, it is important to note that the use of binary evolution tracks would systematically increase the age estimates made here (see Figure 6 in Eldridge & Stanway 2009).

The stellar mass of each cluster is then estimated by scaling the intrinsic V-band luminosity to the predicted luminosity from STARBURST99 models. The predicted luminosity is obtained by passing the synthetic spectra produced by STARBURST99, of the appropriate metallicity and age for each source, through the bandpass describing the observed V-band image (i.e. F550M or the KP 2.1m V-band filters). The stellar masses of the clusters are presented in Table 3.3. Figure 3.7 shows the cluster mass distributions of the sample, the shape of which somewhat reflect the distribution

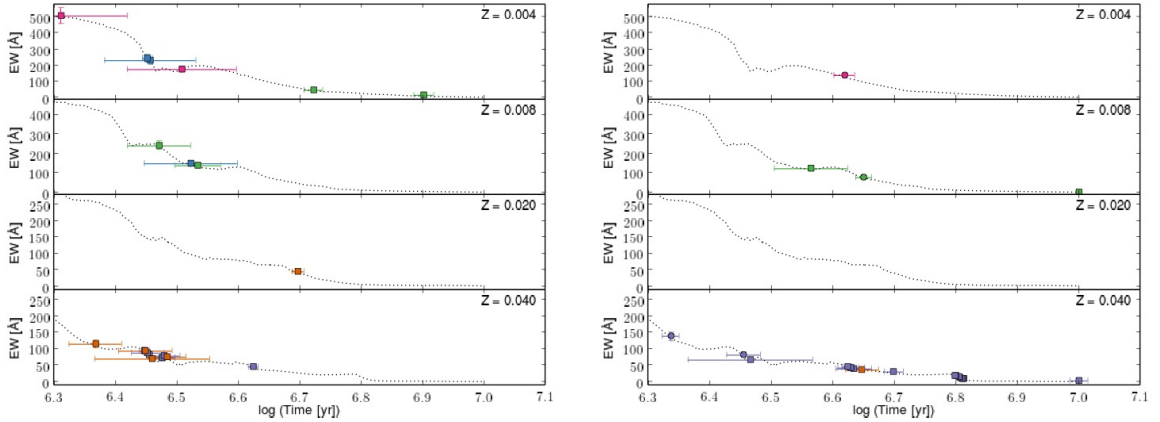


Fig. 3.6.— Ages of the sources in the sample (with WR clusters on the left, and Non-WR clusters on the right) as estimated by the measured equivalent width (EW) of $H\beta$ and predictions from STARBURST99 models, with the appropriate metallicity track plotted as separate panels. Sources are color-coded by host galaxy, as in Figure 3.4.

of the intrinsic luminosities. Overall, the estimated cluster masses fall in the general range for massive star clusters to SSCs ($>10^4 M_{\odot}$), with most WR clusters at typical massive star cluster masses.

3.6.6 Determining the Massive Star Populations

Assessing the massive star populations in individual sources enables the comparison to both simulations and to observations of other regions. I estimate the number of WR stars and O-stars in each emerging WR cluster using the optical spectral observations by following the methods of Schaerer & Vacca (1998) and Guseva et al. (2000). The resulting WR and O-star populations, as well as population ratios, are given in Table 3.5 for the emerging WR clusters.

The WR bumps are used here not only confirm the presence of WR stars, but to estimate the WR populations directly. The number of WR stars is found from $N_{\text{WR}} = L_{\text{WR}}/L_{\text{o,WR}}$, where $L_{\text{o,WR}}$ is the typical luminosity of the WR feature produced by a single WR star and L_{WR} is the observed luminosity of the same feature from the source. The WC subtypes dominate the C IV λ 5808 Å emission

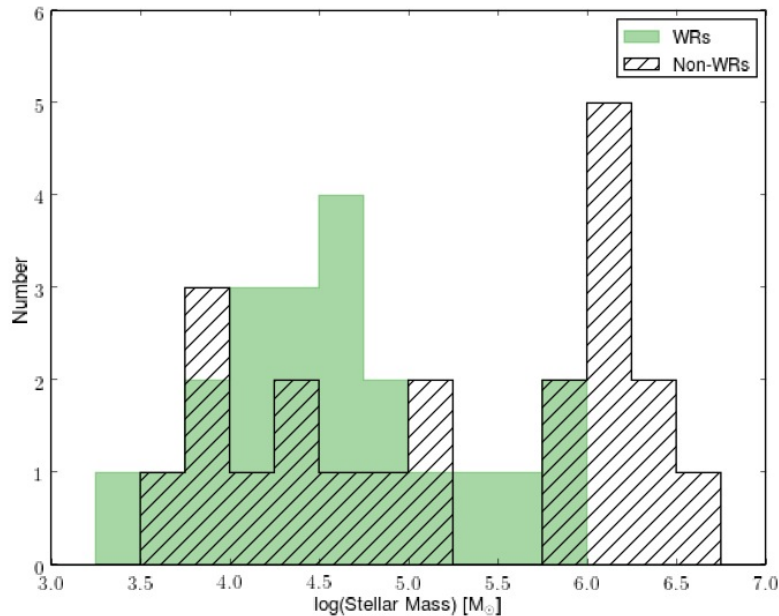


Fig. 3.7.— The distributions of the stellar cluster mass, obtained by scaling the V-band photometry to STARBURST99 models, of the sample.

bump. Therefore, the WC population is found using the approximation of $N_{\text{WC}} = L(5808 \text{ \AA})/L_{\text{WC4}}(5808 \text{ \AA})$, assuming that WC4 stars are representative and have a typical luminosity at 5808 \AA is $3.0 \times 10^{36} \text{ erg s}^{-1}$ as measured in the LMC (Schaerer & Vacca 1998).

The blue WR bump is produced by both WN and WC subtypes. Therefore, the population of WN stars is estimated from the blue WR bump after subtracting off the WCs' contribution. The WCs' contribution to the blue bump feature can be estimated using the luminosity of the red bump with the coefficient

$k = L_{\text{WC4}}(4650 \text{ \AA})/L_{\text{WC4}}(5808 \text{ \AA})$ (Guseva et al. 2000); the adopted value of k is $k=1.71 \pm 0.53$ (Schaerer & Vacca 1998; Guseva et al. 2000). The WN population is then found from the remaining observed emission in this WR feature and by assuming that a WN7 is representative and have a luminosity of $2.0 \times 10^{36} \text{ erg s}^{-1}$ in the blue bump ($4650 + 4686 \text{ \AA}$; Guseva et al. 2000) as in the LMC to Milky Way environments. While O supergiants (Of-type stars) also produce $\text{He II } \lambda 4686 \text{ \AA}$ emission, it is quite

weak compared to that of WNs. Very massive unevolved stars will resemble hydrogen-rich WN stars; the WR stars in the R136 supercluster are such objects (Massey & Hunter 1998). However, the presence of the C IV λ 5808 Å feature in some of my sources shows that, in those cases at least, I am dealing with an evolved massive star population, as this line must be due to WC stars.

Similarly to determining the WR populations, the ionizing flux inferred from the optical Balmer lines can be used to approximate the population of O-stars. The number of O7V stars can be simply estimated by subtracting the ionizing flux produced by the WR stars and assuming an ionizing flux produced by a typical O7V star. I adopt ionizing flux values of $Q_{o,O7V} \sim 10^{48.75} \text{ s}^{-1}$ from an O7V star (Martins et al. 2005) and $Q_{o,WR} \sim 10^{49} \text{ s}^{-1}$ for a WR star (Guseva et al. 2000; Schaerer et al. 1999). To estimate the total O-star population, it is necessary to account for the fact that different subtypes of O-stars produce different ionizing flux values. I account for the different O-star subtypes, which are produced by an IMF, with the parameter $\eta_o = N_{O7V}/N_O$. Thus, the number of O-stars is then found by

$$N_O = (Q_o - N_{WR}Q_{o,WR})/(\eta_o Q_{o,O7V})$$

(Guseva et al. 2000). O-star population uncertainties are estimated by accounting for the measured flux uncertainty in, estimated uncertainties on η_o , and uncertainties for the subtracted WR populations.

3.7 Results

3.7.1 The Commonality of WR Stars in Radio-selected Emerging Clusters

Definitions of “emerging” and “embedded” can vary, the following are used for the purposes of this paper, based on observables: fully embedded—no optical emission is observed; partially embedded—the optical extinction $A_v > 1$ or the ionizing flux inferred from the radio compared to the optical such that $Q_{o, \text{radio}}/Q_{o, H\beta} > 1$; emerged—

Table 3.5. Massive Star Populations in the WR Clusters

Source	O7V	O	WN	WC	WR _{total}	WC/WN	WR/O7V	WR/O
NGC 2366 - Object 10	272 (26)	239 (23)	3 (2)	...	3 (2)	...	0.011 (0.008)	0.013 (0.008)
NGC 2366 - Object 11	92 (17)	75 (16)	6 (5)	2 (1)	8 (5)	0.333 (0.139)	0.087 (0.066)	0.107 (0.070)
NGC 4214 - Object 13	24 (6)	23 (6)	2 (2)	2 (1)	4 (2)	1.000 (0.500)	0.167 (0.118)	0.174 (0.098)
NGC 4214 - Object 14	46 (8)	51 (14)	2 (2)	1 (1)	3 (2)	0.500 (0.500)	0.065 (0.051)	0.059 (0.042)
NGC 4214 - Object 15/16	62 (13)	68 (38)	7 (6)	...	7 (6)	...	0.113 (0.110)	0.103 (0.105)
NGC 4449 - Object 4	3 (16)	...	10 (9)	4 (2)	14 (9)	0.400 (0.180)	4.667 (11.187)	...
NGC 4449 - Object 18	14 (5)	15 (8)	4 (3)	0 (1)	4 (3)	0.030 (0.029)	0.286 (0.274)	0.267 (0.245)
NGC 4449 - Object 22	9 (4)	46 (22)	...	4 (2)	4 (2)	...	0.444 (0.370)	0.087 (0.060)
NGC 4449 - Object 26	179 (17)	142 (32)	2 (2)	4 (1)	6 (2)	2.000 (0.500)	0.034 (0.015)	0.042 (0.017)
NGC 6946 - Object 13	10 (11)	21 (24)	5 (4)	...	5 (4)	...	0.500 (0.660)	0.238 (0.332)
NGC 6946 - Object 48	10 (8)	18 (17)	4 (3)	...	4 (3)	...	0.400 (0.467)	0.222 (0.268)
NGC 6946 - Object 110	34 (12)	42 (15)	...	3 (1)	3 (1)	...	0.088 (0.060)	0.071 (0.035)
NGC 6946 - Object 115	13 (4)	18 (5)	...	1 (1)	1 (1)	...	0.077 (0.088)	0.056 (0.058)
NGC 6946 - Object 117	22 (6)	22 (7)	...	2 (1)	2 (1)	...	0.091 (0.066)	0.091 (0.054)
M 51 - Object 46	169 (18)	317 (127)	3 (3)	5 (2)	8 (4)	1.667 (0.667)	0.047 (0.028)	0.025 (0.016)
M 51 - Object 57	16 (5)	30 (15)	2 (1)	...	2 (1)	...	0.125 (0.094)	0.067 (0.047)
M 51 - Object 73	26 (17)	26 (8)	5 (5)	1 (1)	6 (5)	0.200 (0.200)	0.231 (0.268)	0.231 (0.205)
M 51 - Object 94	34 (17)	69 (42)	7 (5)	...	7 (5)	...	0.206 (0.207)	0.101 (0.095)
M 51 - Object 100	424 (86)	590 (128)	54 (42)	10 (4)	65 (42)	0.185 (0.058)	0.153 (0.121)	0.110 (0.075)
M 51 - Object 101	29 (3)	41 (5)	1 (1)	1 (1)	2 (1)	1.000 (1.000)	0.069 (0.041)	0.049 (0.025)
M 51 - Object 103	19 (6)	26 (9)	2 (2)	...	2 (2)	...	0.105 (0.121)	0.077 (0.081)

Note. — By using the strength of the measured WR bump and the H β flux, I estimate the massive star populations in the individual WR clusters, as well as calculate the population ratios (e.g. WC/WN and WR/O). Both population estimates for O7V stars, directly estimated from the H β flux after subtracting the WR contributions, as well as for all O-stars, which requires an additional estimation of η_o to account for the IMF across the O-star populations, are presented.

not fully emerged and can be partially embedded or have less extinction; and fully emerged—no nebular emission is observed. All of the WR and Non-WR clusters in my study are therefore considered to be emerging, and 39 of the 45 sources are partially embedded.

The emerging massive star clusters of my sample span a wide range of estimated ages; these ages are more diverse than expected based on previous work on thermal radio emission timescales. Thus, it is important to investigate the temporal behavior of the WR emission across those ages to understand if these emerging massive star clusters could or should be in the WR phase at some level. I turn to the predictions of the STARBURST99 models, and find that the WR bump can be produced throughout much of the time that is spanned by the sources in this sample. However, the strength of the WR bump varies greatly with time, shown in Figure 3.9 in which the STARBURST99 predicted EW of the WR bump at 4686 \AA is plotted versus time. In fact, if only the behavior of the strength of the WR emission is considered over time, which rises and falls—appearing to turn on and off without any defined oscillation period, it is clear that one should not expect to detect WR emission throughout the duration of the WR phase for an entire cluster. Many clusters could happen to be observed at a time in between WR emission peaks. The minimum EW observed could be altered by the mass of the cluster, metallicity, and other star formation parameters, and could even result in no WR emission in many cases, especially where stochasticity is at play.

These STARBURST99 predictions above show that the EW of the WR bump can vary in time, and therefore over the ages spanned by the emerging massive star clusters in this sample, a detection of the WR bump could be quite rare. For instance for a $10^6 M_{\odot}$ mass cluster at a metallicity of $z = 0.020$, the EW of the WR bump is expected to be above a detection limit of 2 \AA only $\sim 35\%$ of the time from ~ 1 to 6 Myr. In spite of these expectations, I have found $\sim 50\%$ of the sources in my radio-selected sample show significant detections of the WR bump in their optical spectra (see Figure 3.8). Unfortunately due to the different observing constraints imposed when obtaining optical spectra with different instruments (namely fiber placement using the MMT versus hand-guiding at the Mayall Telescope), the completeness of

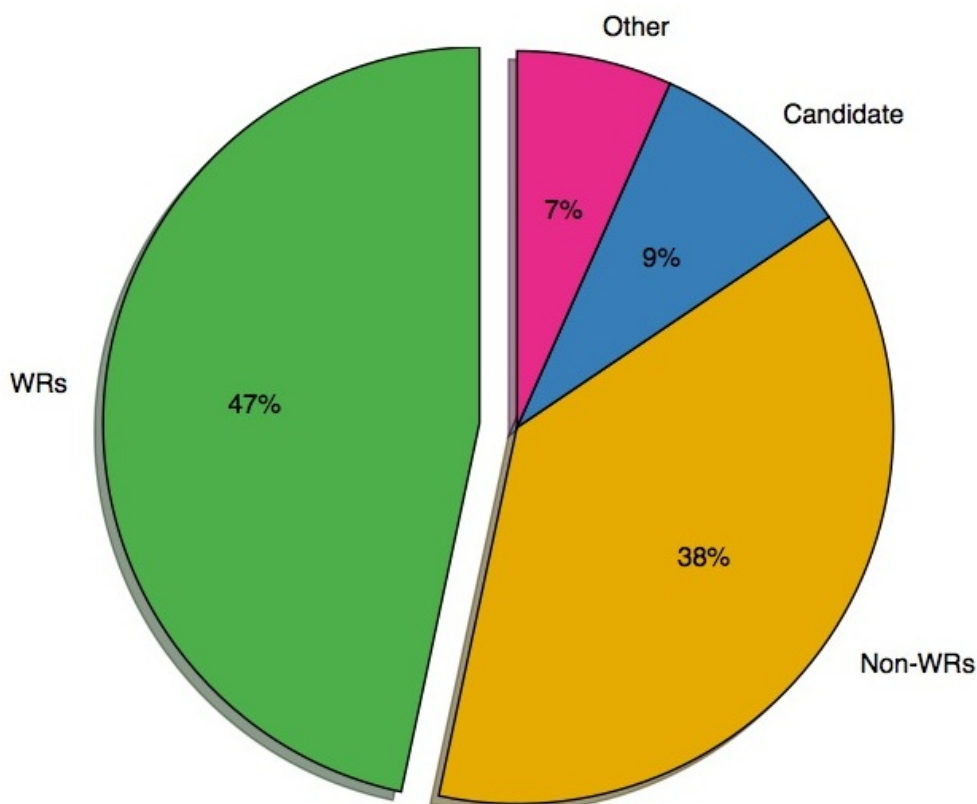


Fig. 3.8.— A pie chart clearly shows the distribution of the classes observed in my sample, with emerging WR clusters as the most common and making up $\sim 50\%$ of the sample. From (Sokal et al. 2015b).

this sample cannot be reliably evaluated. Regardless, I do not think that this high percentage is due to preferentially selecting or observing sources with WR stars; the source selection is based on targets chosen from radio continuum studies and the quality of obtained optical spectra of these targets. I show that all types of sources in the sample, whether a WR bump is detected or not, span roughly the same parameter space of the radio properties from which they are chosen, as in Figure 3.4 where the flux density at 6 cm $F_{\lambda,6cm}$ is plotted versus the radio spectral index α . I adopted a S/N requirement of 15 in the observed spectra, rather than an optical brightness cutoff, that allowed for different exposure times and observing conditions. Sources with or without a bump do not appear to be more limited by this choice. Figure 3.5

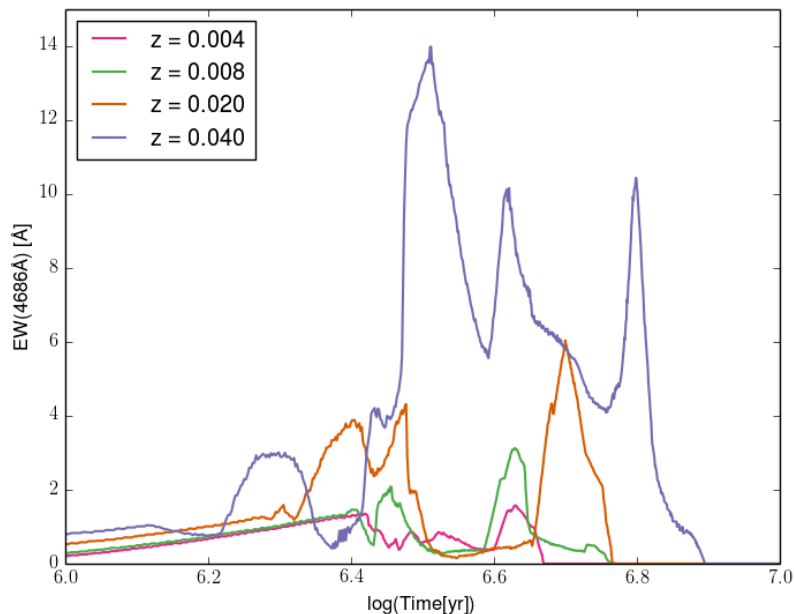


Fig. 3.9.— STARBURST99 (Leitherer et al. 1999) predictions for the behavior of the equivalent width of the WR emission at 4686 Å for all relevant metallicity tracks. It is clear that the WR emission is not constant over the WR phase.

shows the distribution of the observed raw V-band luminosities of the WR clusters is roughly the same as for the Non-WR clusters, although the brightest sources do have WR detections. Because the sample does not appear to be biased toward WR detections due to my source selection process, the sheer number of emerging WR clusters observed in this sample is quite meaningful. The high percentage of WR detections for sources in this sample indicates that WR stars may commonly be present in massive star clusters that are emerging. Overall, this work has shown that it can no longer be assumed that all massive star clusters emerge before their massive star inhabitants begin to evolve off of the main sequence.

3.7.2 Comparing the Massive Star Populations

Plotting the ratio of the massive star populations, meaning the number of WCs compared to WNs or WR stars to O-stars, is an informative tool that can test evo-

lutionary models but also put the observations in context to understand individual sources or general trends. I plot the observed WR/O ratio versus time in comparison to STARBURST99 models for this sample (Figure 3.10). This plot is useful to see what WR/O populations could be expected for a coeval population that fully samples the IMF. The emerging WR clusters are consistent with these predictions, although occasionally somewhat higher. As noted in Section 3.6.5, the STARBURST99 models include only single stars. If binary evolution is considered, the expected WR/O ratio is higher at any given metallicity (see Figure 5 in Eldridge et al. 2008). As these clusters realistically include some binaries, it is no surprise that the WR/O ratio thus is occasionally higher than that expected from STARBURST99. I also plot the WR/O ratio versus metallicity (Figure 3.11) to compare to observations of other star-forming regions, which are overplotted. Uncertainties dominate this plot, but again the WR/O estimates for these sources appear typical. One source, NGC 4449 - Object 4, is quite unusual compared to the rest of the sample. With an estimated WR/O ~ 5 and age of ~ 8 Myr, this source is not shown in either of these plots. The optical spectra show much weaker nebular lines than any other source (see Fig. 3.1). Perhaps this source can be explained by few O-stars remaining un-evolved and much of the ionized gas leaking out, possibly due to increased feedback within this specific cluster.

Shown in Figure 3.11, the WC/WN ratio typically decreases with decreasing metallicity. Discussed in Section 3.6.3.3, this is a direct result of changes in the WR winds in these environments. Thus, the WC/WN ratio is regarded as one of the best observables to compare to stellar evolution models, but is also useful to check my population estimates. The best agreement between models and observations has been at low metallicity, but there has been much improvement at the higher metallicity with the most recent evolutionary models, particularly from the Geneva group that are shown at the solid and dashed lines in the plot. I find that my sources display normal WC/WN values compared to the other plotted regions and in line with the model predictions, although they are fairly loosely constrained in this sample.

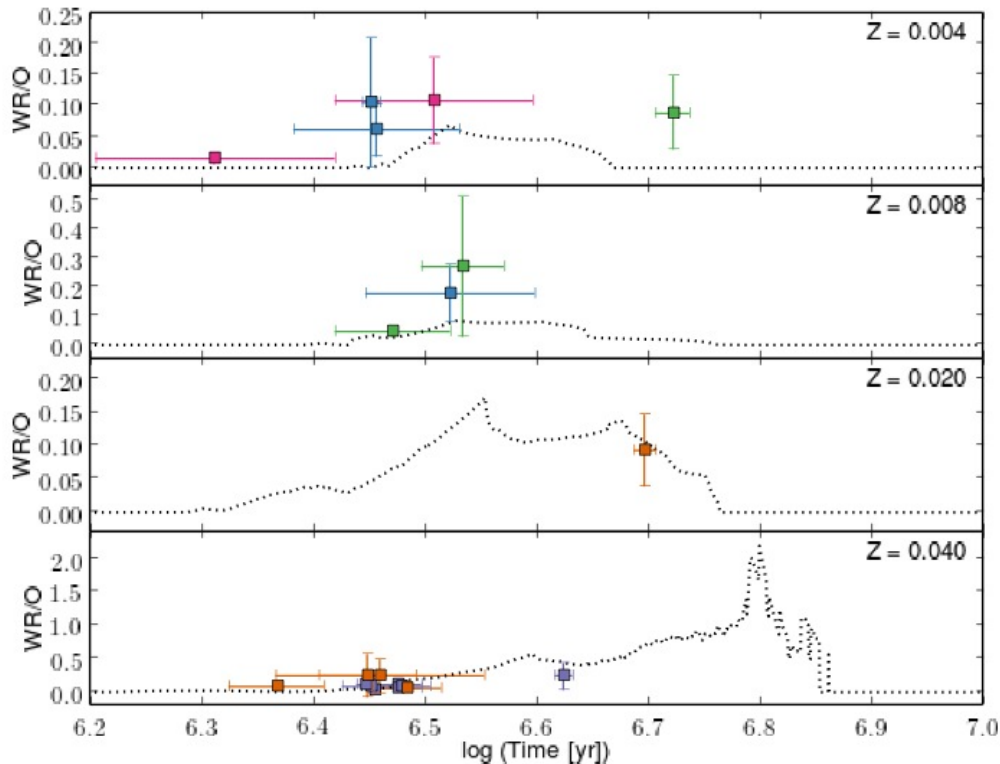


Fig. 3.10.— The estimated ratio of the number of WR stars to O-stars plotted with STARBURST99 predictions (dotted line). Data points are for the emerging WR clusters, colors are the same as in Figure 3.4. NGC 4449 - Object 4 is not shown, which has an observed $WR/O \sim 5$, and is discussed in Section 3.7.2. The estimated populations ratios of sources in this sample are generally consistent with the STARBURST99 models, occasionally somewhat higher.

3.7.3 Evaluating Whether the Sources are Still Embedded

It is evident that the ionizing flux values estimated from the radio emission are much higher than from the optical. Plotting the optically inferred ionizing flux versus the radio inferred ionizing flux on log-log scale in Figure 3.12, the majority of the sample lies below a 1:1 ratio. While the radio flux density at 6 cm may have some non-thermal contributions and thus imply a higher ionizing flux, many of the sources have such large radio inferred ionizing fluxes that major non-thermal contributions ($> 50\%$ or more) would be necessary to explain the observed trend. This observed

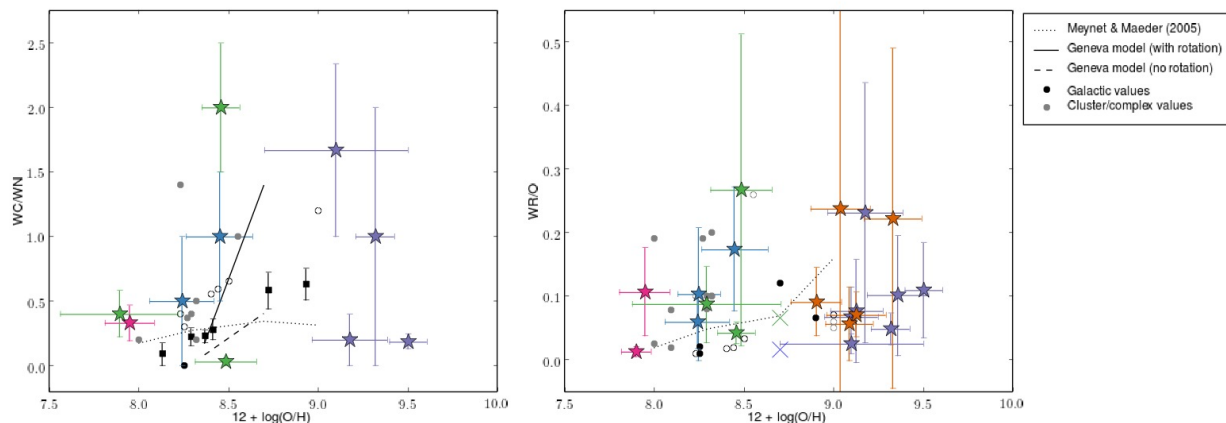


Fig. 3.11.— Populations ratios estimated for these sources in comparison to their metallicity (left: WC/WN, right: WR/O). Observations of other regions, both individual star-forming regions and averaged galactic areas, are overplotted; references can be found in Sokal et al. (2015a). NGC 4449 - Object 4 is not shown, which has an observed WR/O ~ 5 . Uncertainties clutter the plot, but it is clear that the population ratios are similar to predictions and other regions.

trend suggests that most of these massive star clusters are still partially embedded, as more ionizing flux is inferred from the radio, and thus are not fully emerged.

3.7.4 The Excitation of the Sample

To gauge how extreme the star formation environments of the emerging massive star clusters may be, I utilize the Baldwin, Phillips, & Terlevich (BPT) diagram as an optical diagnostic (Baldwin et al. 1981). As shown in Figure 3.13, this is typically a plot of the ratio of the nebular lines of $[\text{N II}]/\text{H}\alpha$ versus $[\text{O III}]/\text{H}\beta$ and is used to evaluate the mechanisms exciting the nebular emission. This is useful to identify if nebular lines are being excited by star formation alone; the theoretical and empirical limits (Kewley et al. 2001; Kauffmann et al. 2003) are overplotted as dashed and dotted-dashed lines. Incontestably, most star-forming galaxies lie well below this star formation limit, as shown by the dotted line that shows the average of Sloan Digital Sky Survey galaxies (Brinchmann et al. 2008). If sources lie above or to the right of these limits, there must be some other contribution providing excitation, such as from shocks or an active galactic nucleus (AGN). Therefore, the BPT diagram is most

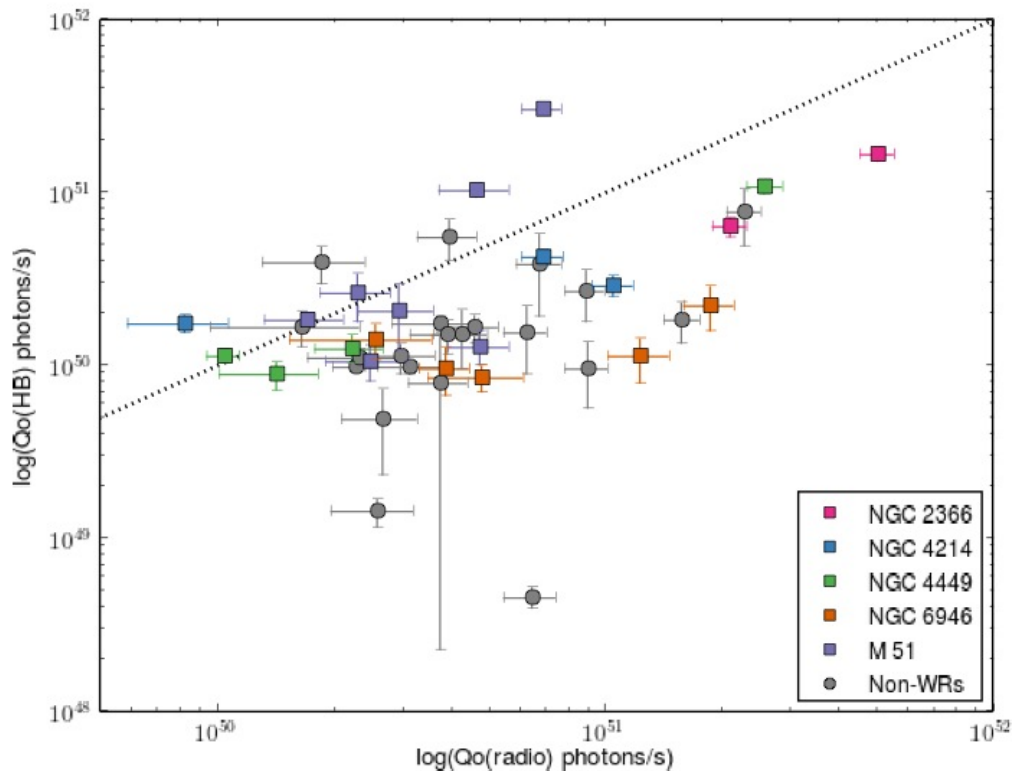


Fig. 3.12.— A plot comparing the ionized flux inferred from thermal radio emission to that inferred from optical nebular $H\beta$ emission. The colors are the same as Figure 3.4. Most sources show a higher ionizing flux inferred from the radio than from the optical observations, suggestive that the sources are still partially embedded.

commonly used to distinguish between star-forming galaxies and AGNs, although it also can indicate the strength of the ionization parameter U and the excitation parameter q for a given metallicity.

The emerging massive star clusters in this sample span the BPT diagram, reflective of the range of metallicities. There does not appear to be any obvious differences in the location of sources with and without WR stars. Most sources lie above the average star-forming galaxy track and appear to border the star formation limit. The direction of this displacement indicates that the emerging massive star clusters have higher ionization and/or excitation parameters than typical $H\ II$ regions, especially the sources in the spiral galaxies M 51 and NGC 6946 with higher metallicity (right

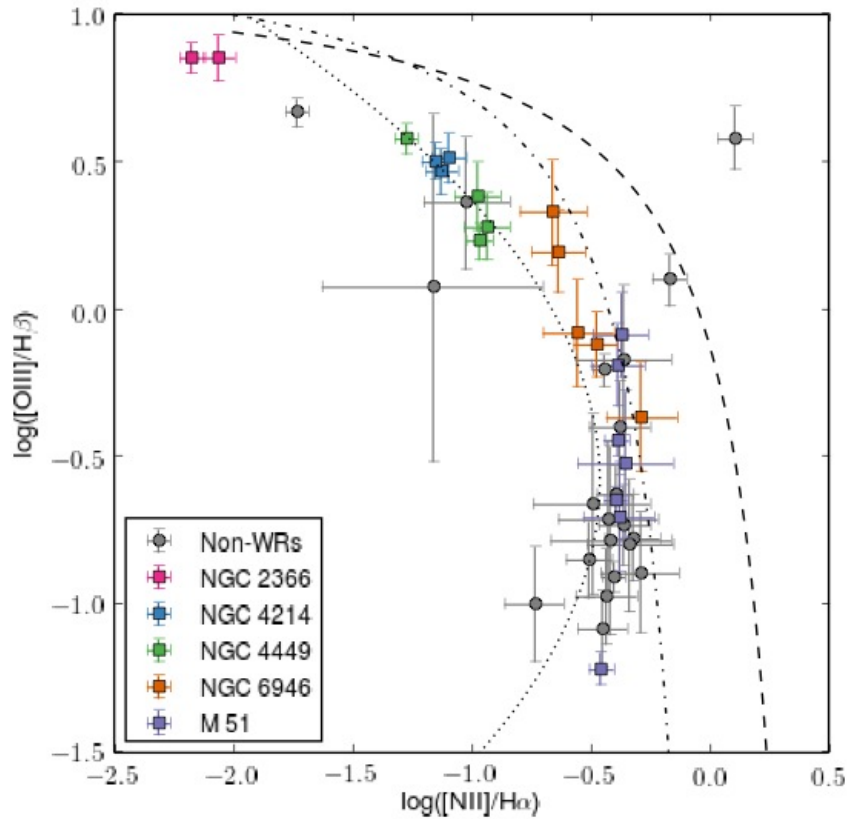


Fig. 3.13.— The BPT diagram (Baldwin et al. 1981) used to evaluate the excitation mechanisms. This full sample spans across the diagram. Generally, the sample is also above where average SDSS star-forming galaxies lie shown by the dotted line (Brinchmann et al. 2008) and borders the theoretical and empirical limits that are produced by star formation along that are shown as dashed and dotted-dashed lines (Kewley et al. 2001; Kauffmann et al. 2003).

side of the plot).

The sources on the left side of this plot are also interesting. Low values of $[\text{N II}]/\text{H}\alpha$ (< -1.0) host low metallicity sources, which often serve as analogs for understanding star formation at high redshift. The sources in NGC 4214 and NGC 4449 roughly lie with the average star-forming galaxies in the BPT diagram at these metallicities. This is also the same area as Green Pea galaxies, which are local extreme galaxies known for high ionization parameters and high $[\text{O III}]/[\text{O II}]$ ratios (Jaskot & Oey 2013),

conditions similar to high redshift star-forming galaxies that may be responsible for reionization (Nakajima & Ouchi 2014). Furthermore, most published BPT diagrams do not extend to ratios < -1.50 and the models shown may not be valid here, yet all of the sources in NGC 2366 fall in this category, which has not yet been well characterized and likely very similar to high redshift objects. Thus, these sources at low metallicity may represent modes of star formation similar to that in the early Universe.

3.7.5 A Different Population: Non-WR Clusters

I have presented many similarities between the WR clusters and the Non-WR clusters thus far, other than the fact that only the WR clusters exhibit the WR bump. However, I have found that the Non-WR clusters are also distinct in their extinctions and ages. The age is plotted versus extinction in Figure 3.14. As the upper and side panels show, the distributions of both of these properties are markedly different between these classes. Moreover, when both properties are examined (the main plot), the sources with the highest extinctions are evidently older and do not contain detectable WR features. A similar effect is seen in Figure 3.15, in which the age is plotted against the ratio of ionizing fluxes as estimated from the radio and from optical emission lines, as in Section 3.7.3. Although the distinction between the two classes is less clear in this plot, most Non-WR clusters are found at higher extinctions.

To further examine this trend, I perform the Kolmogorov-Smirnov (KS) test and the Anderson-Darling (AD) test on the distribution of the extinctions (see Figure 3.16). The KS and AD tests can be used to find confidence limits, where an output p -value less than 0.05 would reject the null hypothesis that the samples come from the same distribution. The extinction of the sources in the two classes (WR and Non-WR clusters) are statistically different with a p -value of 0.0003 from the KS test and a p -value of 0.0009 from the AD test, indicating that do not come from the same underlying extinction distribution. Similarly, the ages of the WR and Non-WR clusters do not come from the same underlying distribution, with p -values of 0.001 (KS test) and 0.006 (AD test). This plot shown in Figure 3.16 indicates that there is

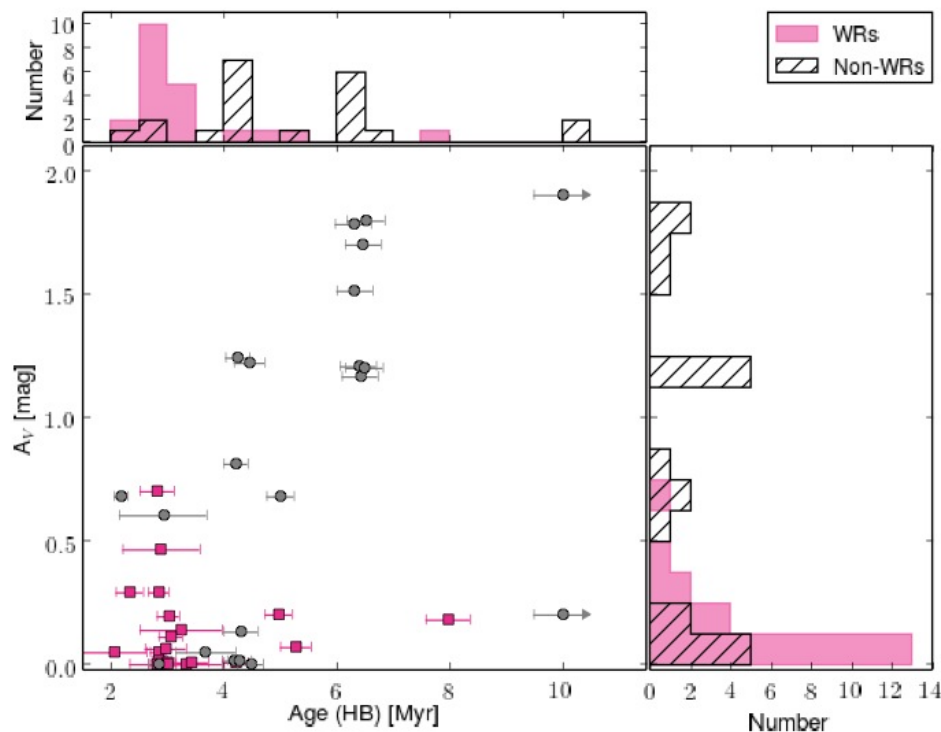


Fig. 3.14.— A look into the ages and extinctions of the sources in the sample. The top/right panel shows a histogram of ages/extinctions and the distribution of these properties are markedly different between the two classes of emerging massive star clusters (WR clusters in pink, non-WR clusters in gray). The main figure shows these properties in comparison as extinction versus age. The most highly extinguished sources do not have detected WR features and tend to have larger ages.

a population of Non-WR clusters that is quite different from the rest of the emerging massive star clusters. This anomalous population of Non-WR clusters tend to be older, extinguished, and do not show signs of WR stars.

Although the KS and AD tests indicate different populations, the massive star clusters in the sample are very messy environments that make proving any evolutionary scenario rather difficult. The subset of Non-WR clusters presented here that are (1) old, (2) have high extinction, and (3) do not currently have WR stars may form the most curious result from this project. Most of these anomalous Non-WR clusters have stellar masses that should be able to produce WR stars, especially as many are

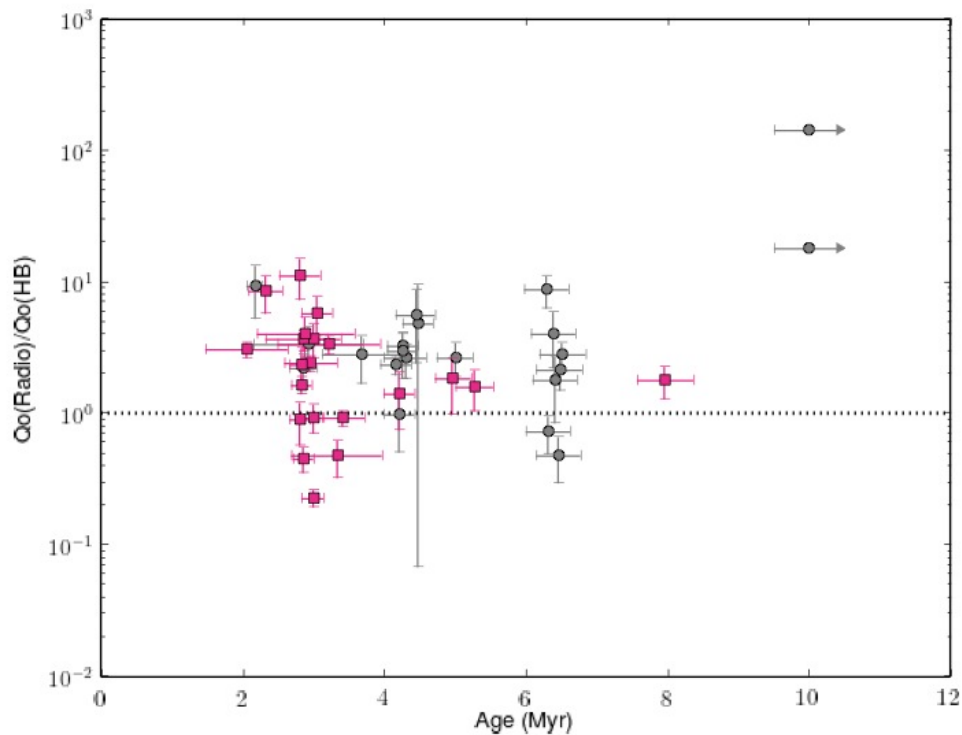


Fig. 3.15.— Similar to Figure 3.14, the age versus the ratio of the ionizing flux estimated from radio to that from $H\beta$, which serves as an extinction measure as well. The Non-WR clusters tend to occupy the upper right side of the plot in comparison to the WR clusters.

at high metallicities. Given the mass and metallicity of the clusters, it is challenging to understand why *all* of these Non-WR clusters exhibit these three characteristics and appear distinct from the rest of the sample (as in Figure 3.14). If these Non-WR clusters are in fact old, highly extinguished, WR-free massive star clusters, then what could they be? The most obvious explanation may be that they did host WR stars at an earlier time and they no longer exist.

In this case, it would be expected that any previous WR stars must have exploded as supernova, which is why they are no longer producing WR bumps. Supernova remnants (SNRs) produce radio emission with a negative spectral index that can dominate over the thermal radio emission. Supernova remnants can inject high energy particles that will give rise to synchrotron emission for up to 1 Gyr (Heesen et al. 2015), and

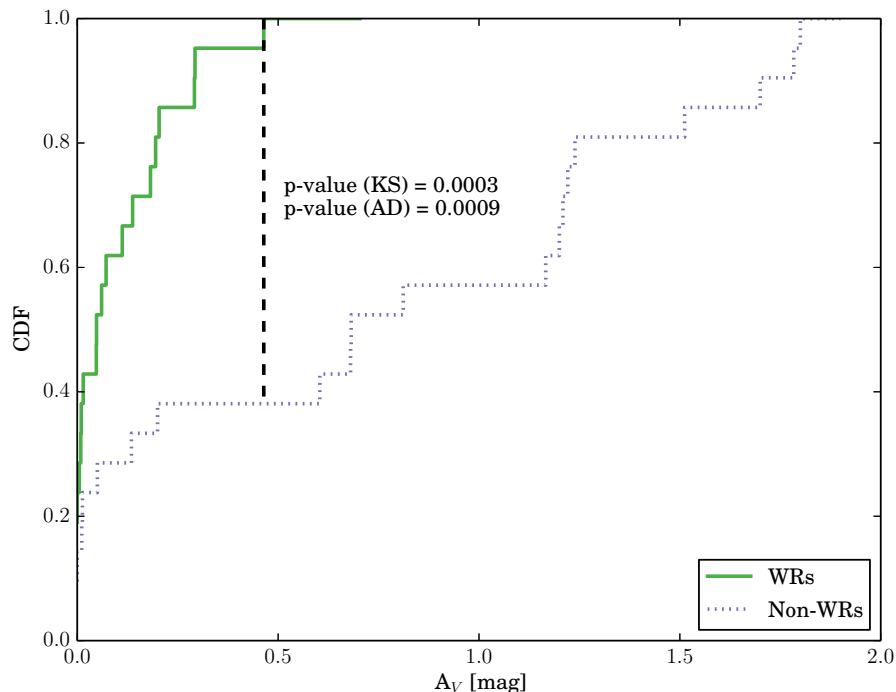


Fig. 3.16.— A plot showing the cumulative distribution functions (CDF) of the extinctions of the WR and Non-WR clusters. I perform the Kolmogorov-Smirnov (KS) test and the Anderson-Darling (AD) test on the distributions of the ages and extinctions. For the extinction distributions, p -values of 0.0003 (KS test) and 0.0009 (AD test) were found, showing that the extinction distributions of the two classes are statistically different. The age distributions are similarly statistically different.

thus the thermal radio-selection of these sources makes this scenario unlikely. S26 can be used as a test case: in Chapter 2 Section 2.6, the observed radio emission is decomposed into thermal and non-thermal components, both leaving the radius as a free variable and set to the optical size of $r=50\text{pc}$. The number of supernova remnants required to reproduce the non-thermal emission can be found using the well-studied galactic supernova remnant Cas A. Cas A has a radio flux density of 2720 Jy (Green 1998) and is at a distance of 3.4 kpc (Reed et al. 1995); at the distance of NGC 4449 it would have a flux density of 2.15 mJy at 20 cm. Adopting Cas A as a typical SNR, then the non-thermal radio emission in S26 is consistent with \sim a single SNR, specifically, 0.6 using a model with $r=50\text{pc}$ or 1. using the model with the radius

unconstrained. Alternatively, the number of SNRs needed to change the observed radio spectral index from $\alpha = -0.2$ to something dominated by non-thermal emission to $\alpha = -0.5$ (still including the observed thermal emission) would be ~ 3.7 for both models. Thus, from these simple estimates, it is clear that S26 may have one or two SNR, but any more would change the observed radio spectral index. Additionally, the clusters would have needed to be in unusually dense environments to remain partially embedded if supernova explosions had occurred. Thus, this scenario may not be viable.

However, the stellar death throes of massive stars are not yet a solved problem—perhaps the endpoints of massive stellar evolution are the answer here. While the common assumption is that they will explode as supernova, there is a possibility that massive stars instead may directly collapse into a black hole. Fryer (1999) found that stars with masses greater than $40 M_{\odot}$ may form a black hole without a supernova explosion (although they may undergo gamma ray bursts if rotating). An archival search for supernova progenitors found none came from massive stars above $18 M_{\odot}$, which can be explained by either the WR phase that is too faint just before the point of core-collapse or that massive stars produce failed supernova and black holes instead (Smartt 2015). There has additionally been an identification of one possible progenitor of a failed supernova as the disappearance of a $25\text{--}30 M_{\odot}$ yellow supergiant (Reynolds et al. 2015). Thus the subsample of old, highly extincted Non-WR clusters can be explained if most stars that are massive enough to become WR stars do not explode as supernova, but instead directly and quietly collapse into black holes. In the case that these clusters had WR stars but they have all died, there would be no indications of either WR stars or supernova in the subsample of Non-WR clusters. One caveat to this scenario is the age: while these Non-WR clusters are past the onset of the WR phase, the majority are less than 8 Myr old and thus not all of the massive stars should have perished and the stars from initial masses of $\sim 25 M_{\odot}$ could be in the WR phase (Eldridge & Stanway 2009). To offer other possible explanations, I discuss here how any of the three derived characteristics (age, extinction, WR detection) could be inaccurate, and the implications (of course combinations are possible as well):

1. Could the anomalous Non-WR clusters be *young* instead?: I estimate the cluster ages using the observed equivalent width of $H\beta$ and STARBURST99 predictions. In addition to uncertainties in the method, there are a few potential scenarios that may result in an overestimation of ages.
 - (a) If ionizing photons were to leak out of the H II region, the cluster could appear older than it actually is. However, the equivalent width would need to be reduced from roughly 100-50 Å to the observed ~ 10 Å in many cases. It is difficult to justify why only the high extinction sources would have leaked such large amounts of their ionizing photons.
 - (b) Similarly, the right distribution of dust in or surrounding the clusters may be responsible for low equivalent width measurements and the resulting derived older ages. If there is a clumpy screen of dust, then the stellar continuum can suffer less extinction due to dust than nebular emission lines (Calzetti et al. 1994), and thus this extinction may reduce the equivalent width of the Balmer lines. However, in the scenario described by Calzetti et al. (1994), the optical continuum is produced by an older stellar population than the emission lines. Thus for this scenario to be considered a feasible explanation, there would need to be both a dust shield and distinct spatial distributions between the WR stars (and young ionizing stars) versus the older stars producing the observed continuum without the WR bump.
 - (c) Another possibility is that the Non-WR clusters are not producing massive enough stars to produce the equivalent widths of $H\beta$ that are expected for young massive star clusters, and thus appearing older than they are. This can occur through several mechanisms. Stochasticity may be affecting these massive star clusters, which becomes important for clusters with masses $\sim 10^5 M_{\odot}$ and less (Fouesneau & Lançon 2010). Thus, the cluster may not produce stars with stellar masses that fully sample the upper end of the IMF. However, this should be extremely rare. Monte Carlo simulations stochastically populating an IMF rarely, if ever, result in mas-

sive clusters $> 10^4 M_{\odot}$ with the maximum mass star being $< 40 M_{\odot}$ (e.g. Krumholz et al. 2015). Yet, most stars $> 25 M_{\odot}$ should evolve into WR stars, especially at the metallicity of M 51. The probability that the most massive star in a $\sim 10^5 M_{\odot}$ cluster is $\sim 25 M_{\odot}$ is clearly less than 5% (see Figs 2 and 3 in Cerviño et al. 2013). Furthermore, some such as Weidner et al. (2010) believe that there is a physical relationship between the mass of a cluster and its most massive star (in opposition to an IMF that is populated stochastically), in which case, the probability would be even further reduced. More likely, an irregular bottom heavy IMF may be able to justify how a population of stars can be formed without massive stars that become WR stars. If these sources were made up of several star clusters, rather than a single massive star cluster that should fully sample the IMF, then the combined stellar populations may only be composed of stars with low mass. At extragalactic distances, the possibility of several densely packed low mass clusters is hard to rule out.

2. Could the anomalous Non-WR clusters have low internal *extinction* instead?: This could be explained by foreground extinction in the host galaxy that results in measurements of high extinction for these sources. As many of these Non-WR clusters lie in the spiral arms of M 51, foreground extinction from the host galaxy likely does contribute on some level. However, if the measured high values are solely due to foreground extinction from the host galaxy rather than internal extinction in the clusters themselves, then why does this foreground extinction only effect the old clusters without WR detections requires a resolution.
3. Could the anomalous Non-WR clusters actually have *WR stars* that are not detected by these observations?: While the Non-WR clusters have high extinctions, and it might seem appealing to assume that these extinctions are diminishing the WR signal, this cannot explain non-detections of the WR bump. Since the WR bump is due to stellar features, the WR bump and the continuum should be affected by extinction in the same way. The non-detections could result instead from various scenarios when additional light from other massive

stars washes out the WR bump, such as the following possibilities:

- (a) One scenario is if the WR stars are weak-lined WR stars. The weakest WR stars can have an $\lambda 4686\text{\AA}$ equivalent width a factor of one hundred less than other WR stars (Crowther 2007). However, weaker lined WR stars are more prevalent at lower metallicities (Crowther & Hadfield 2006), and as the majority of the Non-WR clusters are found in high metallicity environments, this explanation is unlikely.
- (b) Another possibility is aperture-like effects; Kehrig et al. (2013) showed that aperture size can effect a potential WR detection, where the WR signal can be unknowingly wiped out depending on the distribution of WR stars and aperture choice. In my observations, the WR signal could be diluted by including additional light from beyond the cluster. Yet, the sources in each galaxy are treated uniformly, and thus this effect should be present in the entire sample and therefore does not reasonably explain why the Non-WR clusters are different.
- (c) If the star formation were not coeval, then a population of newly formed O-stars could wash out the WR bump produced by still present WR stars formed in an earlier wave of star formation. Yet, the ages of the Non-WR clusters, which are estimated from nebular observations that reflect the most recent star formation, are typically past the onset of the WR phase instead of before. Thus the estimated ages of this sample are not in line with this scenario.
- (d) If the IMF of the cluster differed from the typical Salpeter IMF, there could be more O-stars produced relative to WR stars than expected (or less massive stars in total). If this were the case, then the detection of the WR bump would be more difficult because the light from additional O-stars may dilute the WR feature. For instance, a slightly steeper IMF is observed in M31 that could suggest that the number of massive stars ($> 8 M_{\odot}$) is 25% less than expected with a Kroupa IMF (Weisz et al. 2015). However, little variation has been observed in the IMF universally

(Bastian et al. 2010; Massey 2011), making this explanation difficult to justify.

- (e) As shown by the STARBURST99 predictions shown in Figure 3.9, the strength of the integrated WR features can vary over time. Thus, some of the sources without WR detections could have been observed during one of the low points (appearing “off”) of the duty cycle of the WR features. However, there is no reason that this should correlate with age or extinction, as in Figure 3.14.

3.8 Conclusions and Discussion

To investigate the potential evolutionary role of WR stars in clearing surrounding natal material from massive star clusters, I obtain optical spectra of 42 emerging massive star clusters to search for WR detections. Targets are identified from sources that exhibit thermal radio emission in radio continuum studies of the star-forming galaxies NGC 2366, NGC 4214, NGC 4449, NGC 6946, and M 51. The observed properties of the sources in the sample indicate that these massive star clusters are intense regions of star formation that have not yet completely cleared their natal material. Most sources in the sample, with or without WR stars, exhibit less ionizing flux inferred from the optical emission lines than would be inferred from the thermal radio emission; this suggests that some light is being blocked and thus that these sources are still partially embedded. I also find that the observed nebular line ratios tend to border what can be produced by star formation alone, shown by the BPT diagram in Figure 3.13, suggesting the presence of a hard radiation field.

I find that 50% of the sample exhibited significant detections of the WR bump, and have constrained their nebular environments. The observed ages and high number of WR detections show that the thermal radio emission does not dissipate before WR stars start to appear. Thus, I have not observed a period during which there is thermal radio emission concurrent with optical emission before the WR phase for the cluster begins, as may have been expected.

Overall, these observations of the emerging WR clusters are consistent with the

hypothesis that WR stars may be contributing to the removal of natal material during the cluster emergence. In particular, the interstellar extinction in the emerging WR clusters is found to be lower than most of the non-WR clusters. Moreover, the observed differences between the ages and extinctions of the WR cluster and the Non-WR cluster classes have important evolutionary implications. Naively, if it is assumed that WR stars are partly responsible for clearing a cluster, then clusters without WR stars should have higher extinctions, which is exactly what is seen. Comparing both the ages and extinctions of the sources, I find that some emerging massive star clusters appear to remain embedded for longer, and that these clusters do not show detections of the WR bump; many Non-WR clusters with high extinction are ~ 5 Myr older than most WR clusters (see Figure 3.14). Thus if sources without WR stars stay embedded longer than sources with WR stars, the WR stars could actually be helping these clusters to emerge. This may suggest that WR stars make the emerging process more efficient or accelerated, and possibly necessary in some cases, for clusters to clear obscuring natal material.

While alternative scenarios to the observed ages, extinctions, or WR detections are offered, and it is clear that many unknowns may hamper my interpretation of this data, my observations of relatively cleared out WR clusters and extincted, old clusters that do not exhibit WR features are quite compelling and indicative of the importance of the WR stars. Thus, further optical spectral observations of additional massive star clusters exhibiting thermal radio emission are needed. An expanded sample will greatly expand our understanding of emerging massive star clusters and SSCs and provide further constraints to some of the suggested scenarios. I suspect that the radio selection process is an important component in this study, as it identifies clusters that still have gaseous material but are not subject to extinction. This method is different than typical observed collections of extragalactic H II regions, which are mostly found through optical brightness criteria, and may explain why sources like the Non-WR clusters have not been previously scrutinized. While radio continuum surveys to obtain high enough sensitivities to detect these extragalactic H II regions are expensive, the new capabilities of the Karl G. Jansky Very Large Array have increased continuum sensitivities by more than an order of magnitude.

New radio continuum studies are already coming out, such as the Star Formation in Radio Survey that has resolved thermal radio sources (Murphy et al. 2012), and show there is hope for this field to rapidly advance.

To truly confirm the role of the WR stars in how massive star clusters emerge, complex simulations are needed that not only model massive star clusters but also specifically include the WR phase and incorporate different feedback mechanisms. Current technology cannot reach these massive and SSC mass scales with the resolutions needed that also include feedback processes, and it is not reliable to simply scale from lower mass systems (Banerjee & Kroupa 2015). Fortunately, we are already witnessing advancements in capabilities. For instance, SSC mass scales have been reached by recent simulation of radiation feedback on a nascent SSC (Skinner & Ostriker 2015). Thus, with increased radio telescope sensitivities and the continued improvements toward complex simulations, we will soon be able to disentangle the physical effects of WR stars in massive star cluster evolution.

Appendix A: Source Spectra and Images

We present the optical spectra obtained for this study of the sources in our sample and archival images of these interesting objects. In addition to the spectra shown in Figure 3.1, additional spectra for the WR class are shown throughout Figures A1-A2, and the full sample throughout Figures A1-A4. In the same fashion, an example image showing a subset of these regions was presented in Figure 3.2; the rest of the sample is presented here in Figures A5-A6. We also include tables describing the observations (Tables A1-A2) and various measured properties of the sources, such as optical characteristics (Table A3) and line fluxes (Tables A4-A5).

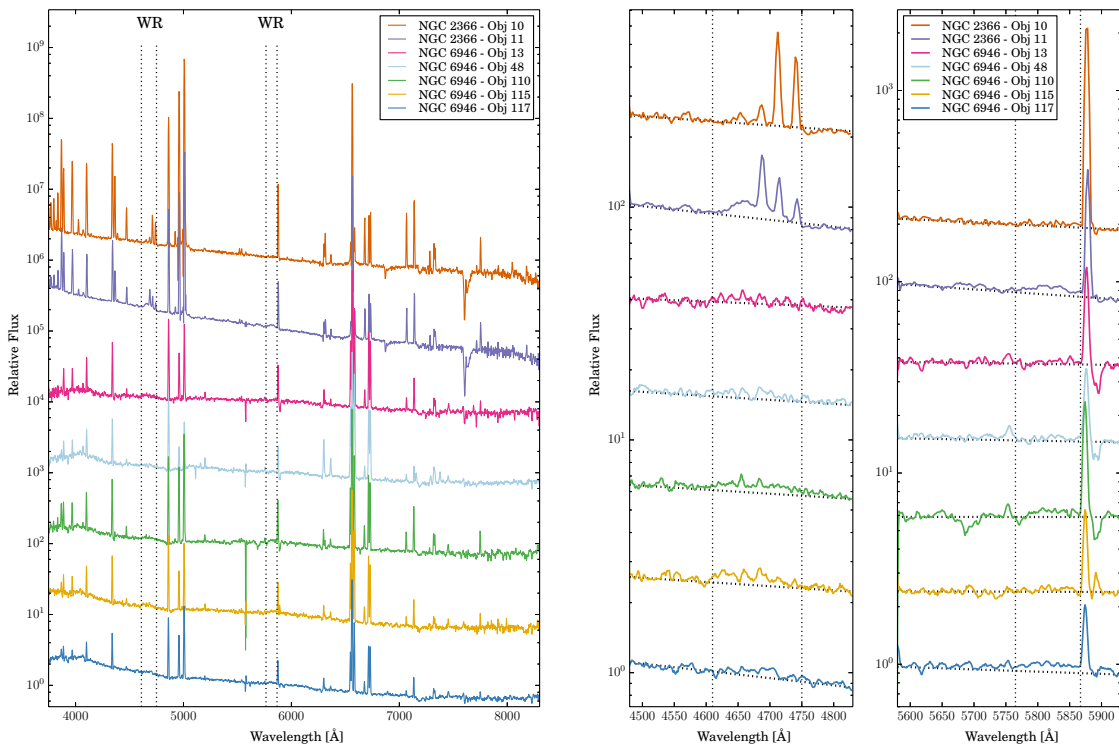


Fig. A1.— Optical spectra observed with the 4m Mayall Telescope at KPNO and the 6.5m MMT of another subset of the WR clusters, otherwise the same as Figure 3.1.

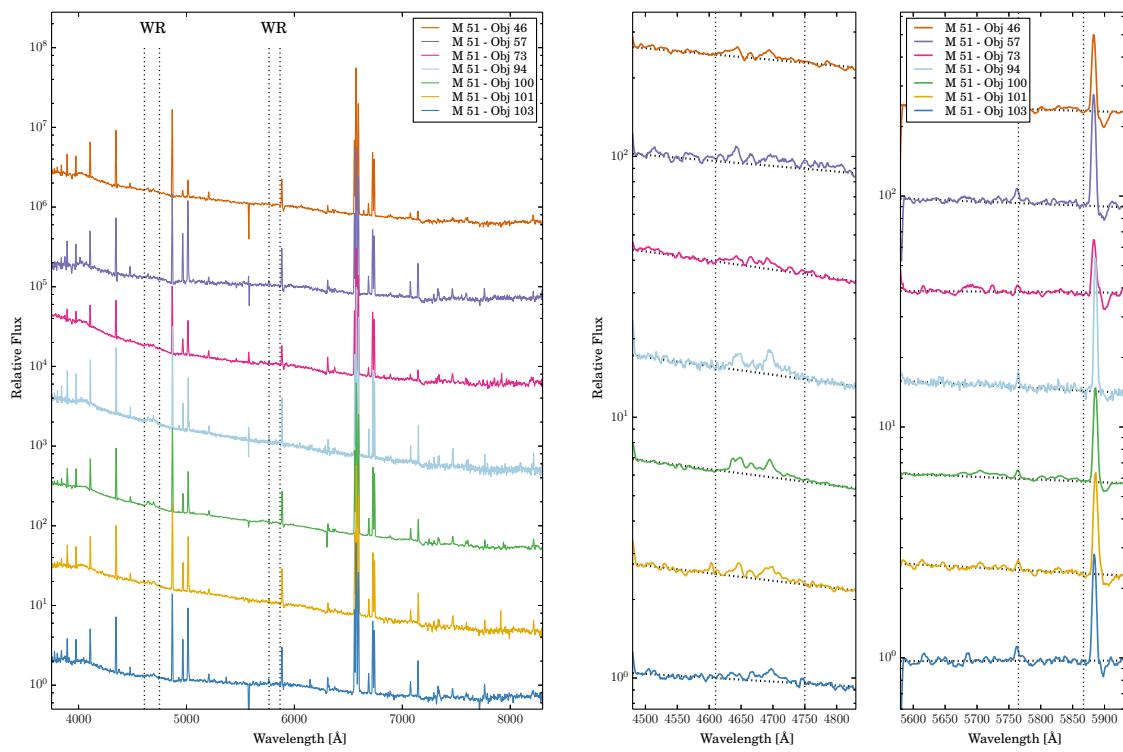


Fig. A2.— Optical spectra observed with the 6.5m MMT of the rest of the WR clusters, otherwise the same as Figure 3.1.

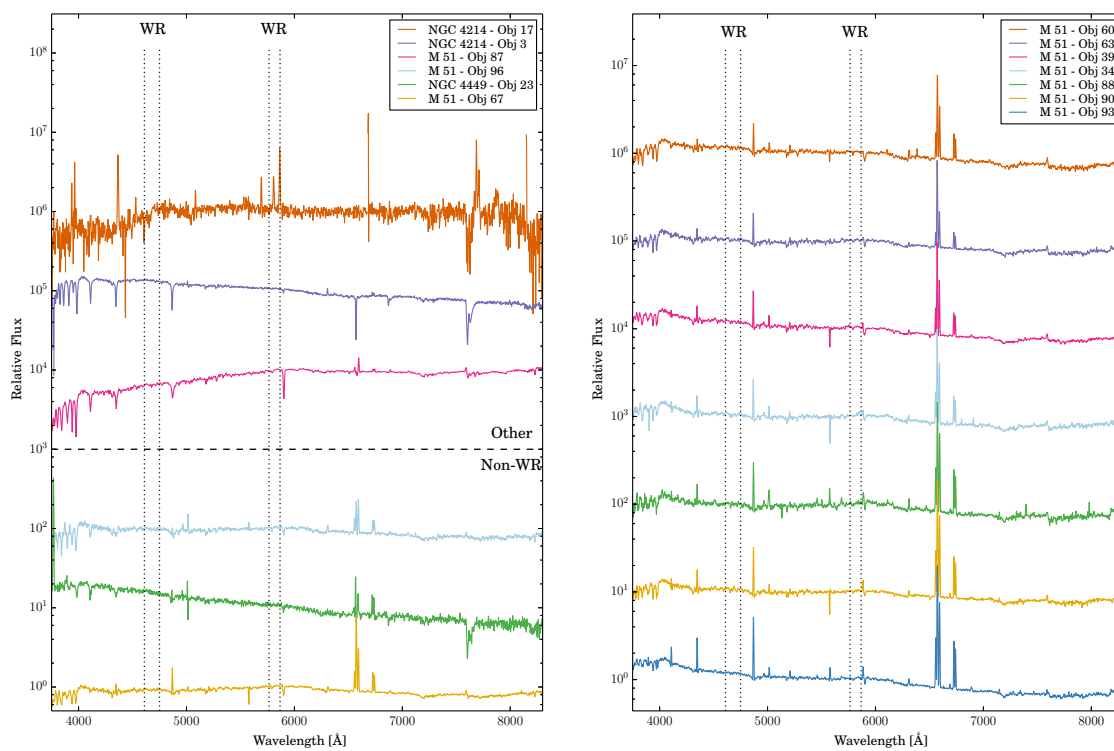


Fig. A3.— Optical spectra observed with the 4m Mayall Telescope at KPNO and the 6.5m MMT of a subset of the ‘no-bump’ sources, otherwise the same as Figure 3.1 without the zoom-in panels of WR feature regions.

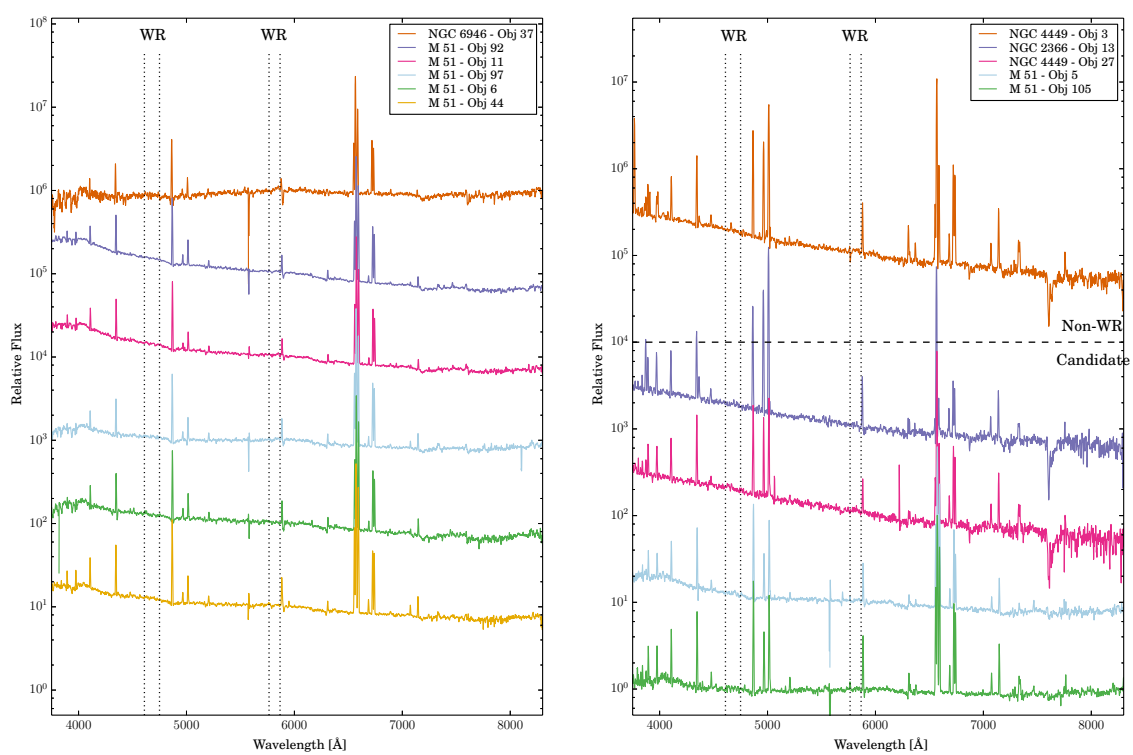


Fig. A4.— Optical spectra observed with the 6.5m MMT of the rest of the ‘no-bump’ sources, otherwise the same as Figure A3.

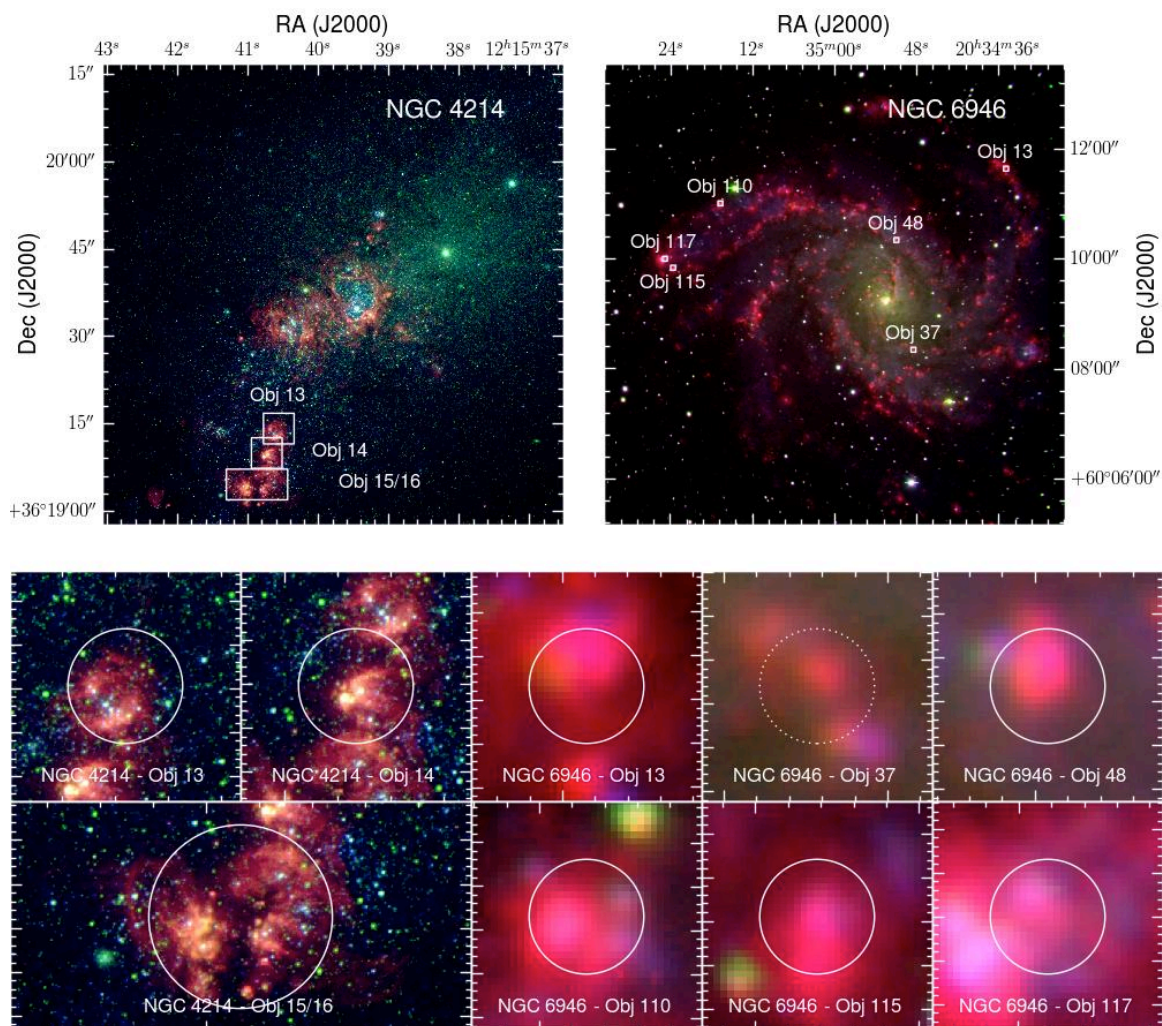


Fig. A5.— Archival *HST* and KP 2.1m images ($H\alpha$, B, I) of the target galaxies NGC 4214 and NGC 6946. Insets and overlaid regions are the same as 3.2 with the exception that the extracted region and corresponding overlaid circle on source NGC 4214 - Object 15/16 is $4''$.

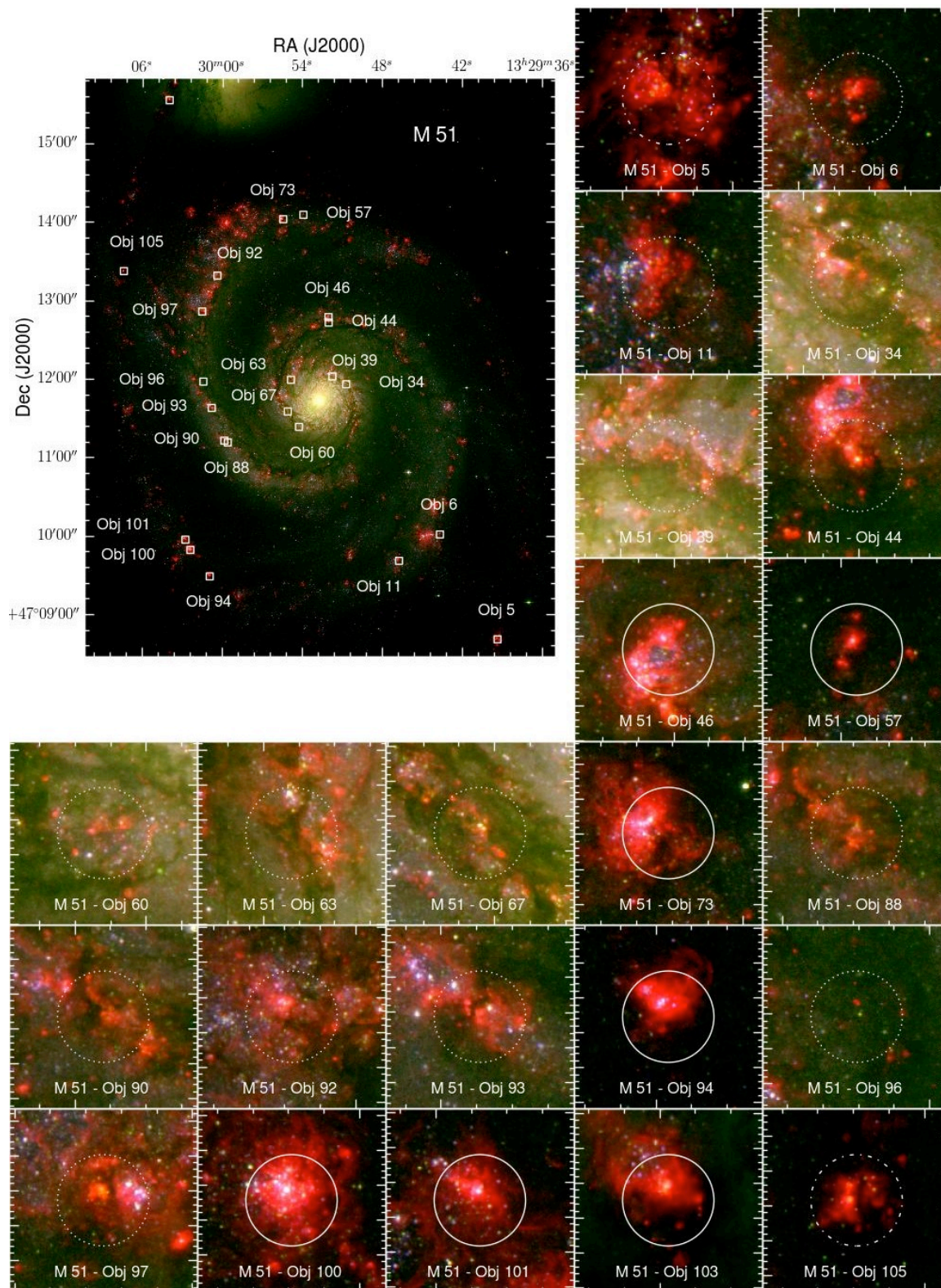


Fig. A6.— Archival *HST* images ($H\alpha$, B, I) of the target galaxy M51. Insets and overlaid regions are the same as Figure 3.2.

Table A1. Optical Spectral Observations

Source	Right Ascension α	Declination δ	Exposure Time (s)	Date Observed ^a
NGC 2366 - Object 10	7:28:42.58	+69:11:22.0	2400	2013-04-12
NGC 2366 - Object 11	7:28:43.71	+69:11:22.4	1800	2013-04-15 ^b
NGC 2366 - Object 13	7:28:45.69	+69:11:25.8	1800	2013-04-13
			1800	2013-04-15
NGC 4214 - Object 3	12:15:38.18	+36:19:44.9	1200	2013-04-12
			900	2013-04-14
			900	2013-04-15
NGC 4214 - Object 13	12:15:40.56	+36:19:14.1	2100	2013-04-12 ^c
			900	2013-04-14
			1800	2013-04-15 ^d
NGC 4214 - Object 14	12:15:40.73	+36:19:09.9	1800	2013-04-14
			900	2013-04-15
NGC 4214 - Object 15/16 ^e	12:15:40.87 ^e	+36:19:04.4 ^e	1800	2013-04-12
			2700	2013-04-14
			600	2013-04-15
NGC 4214 - Object 17	12:15:41.36	+36:21:14.1	2700	2013-04-14
			1800	2013-04-15
NGC 4449 - Object 3	12:28:09.37	+44:05:20.2	1200	2013-04-13
			2700	2013-04-14
			900	2013-04-15
NGC 4449 - Object 4	12:28:09.44	+44:05:16.3	1800	2013-04-13
NGC 4449 - Object 18	12:28:12.63	+44:05:03.7	1800	2013-04-13
			1800	2013-04-14
NGC 4449 - Object 22	12:28:12.99	+44:06:56.3	1800	2013-04-13
			1800	2013-04-14
NGC 4449 - Object 23	12:28:13.08	+44:05:42.7	1800	2013-04-13
NGC 4449 - Object 26	12:28:13.86	+44:07:10.4	1800	2013-04-13
NGC 4449 - Object 27	12:28:14.83	+44:07:10.0	1800	2013-04-13
			1800	2013-04-15
NGC 6946 - Object 13	20:34:34.85	+60:11:38.6	3600.	2013-04-08
NGC 6946 - Object 37	20:34:48.43	+60:08:20.8	3600.	2013-04-07
NGC 6946 - Object 48	20:34:50.92	+60:10:20.7	3600.	2013-04-07
NGC 6946 - Object 110	20:35:16.71	+60:11:00.6	3600.	2013-04-07
			3600.	2013-04-08
NGC 6946 - Object 115	20:35:23.62	+60:09:50.2	3600.	2013-04-08
NGC 6946 - Object 117	20:35:24.82	+60:10:00.0	3600.	2013-04-07
M 51 - Object 5	13:29:39.36	+47:08:40.7	6300.	2013-04-02
			6300.	2013-04-06
M 51 - Object 6	13:29:43.67	+47:10:01.0	6300.	2013-04-02
			6300.	2013-04-06
M 51 - Object 11	13:29:46.74	+47:09:40.8	6300.	2013-04-02
			12600.	2013-04-06
M 51 - Object 34	13:29:50.70	+47:11:55.9	6300.	2013-04-06
M 51 - Object 39	13:29:51.73	+47:12:01.9	6300.	2013-04-02
			6300.	2013-04-06
M 51 - Object 44	13:29:52.01	+47:12:42.9	6300.	2013-04-02
M 51 - Object 46	13:29:52.03	+47:12:47.2	6300.	2013-04-06
M 51 - Object 57	13:29:53.91	+47:14:05.4	6300.	2013-04-06
M 51 - Object 60	13:29:54.24	+47:11:23.2	6300.	2013-04-02
M 51 - Object 63	13:29:54.84	+47:11:59.2	6300.	2013-04-02
			6300.	2013-04-06
M 51 - Object 67	13:29:55.08	+47:11:35.0	6300.	2013-04-06
M 51 - Object 73	13:29:55.42	+47:14:02.1	6300.	2013-04-02

Table A1—Continued

Source	Right Ascension α	Declination δ	Exposure Time (s)	Date Observed ^a
			6300.	2013-04-06
M 51 - Object 87	13:29:59.53	+47:15:58.3	6300.	2013-04-06
M 51 - Object 88	13:29:59.58	+47:11:11.3	6300.	2013-04-06
M 51 - Object 90	13:29:59.84	+47:11:12.7	6300.	2013-04-02
			6300.	2013-04-06
M 51 - Object 92	13:30:00.36	+47:13:18.9	6300.	2013-04-02
			12600.	2013-04-06
M 51 - Object 93	13:30:00.78	+47:11:37.7	6300.	2013-04-02
			6300.	2013-04-06
M 51 - Object 94	13:30:00.93	+47:09:28.9	6300.	2013-04-02
			6300.	2013-04-06
M 51 - Object 96	13:30:01.41	+47:11:57.8	6300.	2013-04-06
M 51 - Object 97	13:30:01.50	+47:12:51.4	6300.	2013-04-02
			6300.	2013-04-06
M 51 - Object 100	13:30:02.38	+47:09:49.1	6300.	2013-04-06
M 51 - Object 101	13:30:02.75	+47:09:56.9	6300.	2013-04-02
M 51 - Object 103	13:30:03.95	+47:15:33.0	6300.	2013-04-02
			6300.	2013-04-06
M 51 - Object 105	13:30:07.38	+47:13:22.3	6300.	2013-04-02
			12600.	2013-04-06

Note. — This table presents the observations obtaining the optical spectra, by source, with the 4m Mayall Telescope at KPNO and the 6.5m MMT. We determine flux corrections (see Section 3.6.2) to account for any non-ideal observing conditions.

^ayyyy-mm-dd

^bat wind limit

^csome clouds

^dbad seeing

^eThe targets NGC 4214 - Obj 15 and NGC 4214 - Obj 16 could not be separated. Therefore, the combined spectrum is used and the averaged positions of Object 15 (12:15:40.76 +36:19:04.5) and Object 16 (12:15:40.98 +36:19:04.3) is presented.

Table A2. Archival V-Band Imaging Observations

Galaxy	Telescope	Filter	Description	Instrument	Date Observed	Proposal ID	PI
NGC 2366	<i>HST</i>	F547M	V	WFPC2	1996-01-08	6096	L. Drissen
NGC 4214	<i>HST</i>	F547M	V	WFC3(UVIS)	2009-12-23	11360	R. O'Connell
NGC 4449	<i>HST</i>	F550M	V	ACS(WFC)	2005-11-18	10522	D. Calzetti
NGC 6946	KP ^a	V	V	CFIM(t2ka)	2001-11-08	...	K. Gordon ^b
M 51	<i>HST</i>	F555W	wide-V	ACS(WFC)	2005-01-20	10452	S. Beckwith

Note. — Observing information for archival optical images with medium and broad V-band filters.

^aKP= Kitt Peak National Observatory 2.1m Telescope.

^bPrimary observer.

Table A3. Optical Characteristics of the Sample

Source	$F_{\text{cont}, 6000 \text{ \AA}}$ ergs cm ⁻² s ⁻¹	Flux Correction	-EW(H β) \AA	$L_{V,o}$ erg s ⁻¹
NGC 2366 - Object 10	7.88e-16	1.0	505.0 (50.5)	1.48e+36 (2.908e+34)
NGC 2366 - Object 11	6.23e-16	1.0	176.1 (17.6)	6.74e+35 (2.348e+34)
NGC 2366 - Object 13	1.70e-16	1.0	134.9 (13.5)	2.27e+35 (3.291e+34)
NGC 4214 - Object 13	3.45e-16	1.0	148.0 (14.8)	3.58e+35 (4.652e+34)
NGC 4214 - Object 14	3.81e-16	1.0	226.9 (22.7)	3.61e+35 (4.547e+34)
NGC 4214 - Object 15/16	6.74e-16	1.1	241.7 (24.2)	8.69e+35 (1.254e+35)
NGC 4449 - Object 3	2.01e-16	1.2	123.5 (12.3)	4.41e+35 (1.644e+35)
NGC 4449 - Object 4	1.43e-15	1.0	13.0 (1.3)	1.21e+36 (1.837e+35)
NGC 4449 - Object 18	1.28e-16	1.0	138.0 (13.8)	1.38e+35 (3.473e+34)
NGC 4449 - Object 22	2.90e-16	1.0	45.1 (4.5)	6.45e+35 (8.496e+34)
NGC 4449 - Object 23	3.49e-16	1.0	2.5 (0.3)	3.87e+35 (2.918e+35)
NGC 4449 - Object 26	6.20e-16	1.4	241.2 (24.1)	1.38e+36 (7.294e+34)
NGC 4449 - Object 27	1.65e-16	1.5	78.1 (7.8)	3.59e+35 (1.175e+34)
NGC 6946 - Object 13	7.34e-17	1.0	92.6 (9.3)	6.46e+36 (7.571e+35)
NGC 6946 - Object 37	6.52e-17	1.0	36.4 (3.7)	1.23e+36 (1.354e+35)
NGC 6946 - Object 48	1.07e-16	1.0	69.5 (7.0)	4.67e+36 (2.705e+35)
NGC 6946 - Object 110	1.97e-16	2.9	114.2 (11.4)	9.75e+36 (8.923e+35)
NGC 6946 - Object 115	1.22e-16	1.6	73.2 (7.3)	5.29e+36 (3.233e+35)
NGC 6946 - Object 117	2.77e-16	2.4	43.9 (4.4)	1.33e+37 (7.997e+35)
M 51 - Object 5	1.36e-16	3.4	81.9 (8.2)	1.12e+36 (2.362e+34)
M 51 - Object 6	1.07e-16	2.1	43.8 (4.4)	8.33e+35 (5.775e+35)
M 51 - Object 11	1.40e-16	2.2	40.1 (4.0)	1.12e+36 (1.359e+35)
M 51 - Object 34	2.28e-16	1.6	13.1 (1.3)	2.38e+36 (1.789e+36)
M 51 - Object 39	6.21e-16	2.8	11.3 (1.2)	4.65e+36 (3.351e+36)
M 51 - Object 44	1.44e-16	1.5	65.5 (6.6)	1.98e+35 (1.081e+35)
M 51 - Object 46	6.60e-16	4.5	79.3 (7.9)	3.89e+36 (2.997e+35)
M 51 - Object 57	5.89e-17	1.0	87.1 (8.7)	2.07e+35 (1.553e+35)
M 51 - Object 60	2.32e-16	1.2	8.8 (0.9)	2.16e+36 (1.620e+36)
M 51 - Object 63	4.12e-16	3.4	9.2 (0.9)	2.84e+36 (2.411e+36)
M 51 - Object 67	1.98e-16	1.0	7.6 (0.8)	1.15e+36 (2.859e+35)
M 51 - Object 73	2.29e-16	2.7	43.6 (4.4)	2.03e+36 (8.617e+34)
M 51 - Object 88	4.35e-16	5.3	17.1 (1.7)	6.23e+35 (4.672e+35)
M 51 - Object 90	8.71e-17	1.0	18.0 (1.8)	4.60e+35 (3.448e+35)
M 51 - Object 92	1.88e-16	1.6	38.5 (3.9)	1.57e+36 (1.169e+35)
M 51 - Object 93	1.33e-16	1.1	27.9 (2.8)	9.97e+35 (6.381e+34)
M 51 - Object 94	1.12e-16	1.1	94.2 (9.4)	1.10e+36 (1.592e+34)
M 51 - Object 96	8.07e-17	1.0	1.4 (0.2)	2.91e+35 (2.413e+35)
M 51 - Object 97	3.44e-16	4.1	41.0 (4.1)	2.52e+36 (9.240e+35)
M 51 - Object 100	1.95e-15	6.0	70.9 (7.1)	4.15e+36 (1.101e+35)
M 51 - Object 101	1.11e-16	1.0	71.0 (7.1)	1.59e+36 (1.463e+35)
M 51 - Object 103	8.33e-17	1.5	78.5 (7.9)	6.92e+35 (1.984e+35)
M 51 - Object 105	2.80e-17	1.0	137.7 (13.8)	1.04e+35 (3.161e+34)

Note. — A table presenting various optical characteristics used throughout this paper. Specifically, the spectra shown in Figures 3.1 - A4 are normalized to the average continuum values presented in this table, as well as the following for “Other” sources (not listed above): M 51 - Object 87: $F_{\text{cont}, 6000 \text{ \AA}} = 6.33\text{e-}15$ ergs cm⁻² s⁻¹, NGC 4214 - Object 3: $F_{\text{cont}, 6000 \text{ \AA}} = 1.07\text{e-}15$ ergs cm⁻² s⁻¹, and NGC 4214 - Object 17: $F_{\text{cont}, 6000 \text{ \AA}} = 6.44\text{e-}17$ ergs cm⁻² s⁻¹. The Flux Correction is determined from the V-band photometry and is discussed in Section 3.6.2.

Table A4. Emission Line Fluxes for WR Clusters^a

Source	[O II] 3727 Å	H δ 4102 Å	H γ 4341 Å	[O III] 4363 Å	[O III] 4959 Å	[O III] 5007 Å	[N II] 6548 Å	H α 6563 Å	[N II] 6584 Å	[S II] 6717 Å	[S II] 6732 Å	[O II] 7319 Å	[O II] 7330 Å	H β ^a 4861 Å
N2366 - Obj 10	45 (4)	23 (2)	46 (4)	15 (1)	238 (20)	705 (60)	0.8 (0.1)	292 (24)	2.0 (0.2)	3.6 (0.3)	3.4 (0.3)	1.0 (0.1)	0.8 (0.1)	590 (50)
N2366 - Obj 11	69 (10)	23 (3)	39 (5)	12 (2)	205 (25)	707 (87)	1.1 (0.2)	305 (33)	2.6 (0.3)	5.2 (0.6)	3.9 (0.5)	1.1 (0.3)	1.5 (0.5)	225 (28)
N4214 - Obj 13	277 (41)	22 (3)	46 (6)	2.0 (0.4)	97 (12)	292 (36)	7.2 (0.8)	274 (30)	20 (2)	19 (2)	14 (2)	3.0 (0.5)	2.6 (0.5)	80.8 (10.2)
N4214 - Obj 14	219 (37)	23 (4)	45 (7)	2.8 (0.5)	108 (15)	326 (45)	6.1 (0.7)	245 (29)	20 (2)	18 (2)	14 (2)	2.9 (0.4)	2.8 (0.4)	133 (19)
N4214 - Obj 15/16	248 (27)	30 (3)	46 (5)	3.8 (0.4)	145 (14)	316 (31)	6.1 (0.6)	296 (27)	21 (2)	20 (2)	14 (1)	2.8 (0.3)	3.2 (0.4)	194 (19)
N4449 - Obj 4	327 (77)	16 (4)	34 (7)	7 (2)	92 (17)	240 (45)	13 (2)	312 (49)	33 (5)	34 (6)	26 (4)	11 (3)	...	34.1 (6.6)
N4449 - Obj 18	316 (36)	26 (3)	48 (5)	2.2 (0.3)	54 (5)	170 (17)	10.2 (1.0)	268 (25)	29 (3)	27 (3)	18 (2)	2.8 (0.5)	2.8 (0.6)	30.7 (3.1)
N4449 - Obj 22	417 (96)	29 (6)	57 (12)	6 (1)	69 (13)	190 (35)	10 (2)	304 (47)	35 (5)	51 (8)	36 (5)	6 (1)	3.6 (0.7)	24.0 (4.5)
N4449 - Obj 26	204 (19)	24 (2)	46 (4)	2.1 (0.2)	126 (11)	376 (32)	5.3 (0.4)	294 (24)	16 (1)	16 (1)	12 (1)	2.4 (0.2)	2.1 (0.2)	289 (25)
N6946 - Obj 13	195 (73)	22 (7)	43 (14)	...	28 (8)	84 (24)	41 (10)	457 (109)	128 (31)	57 (13)	41 (10)	3.4 (0.8)	2.8 (0.7)	14.6 (4.4)
N6946 - Obj 48	129 (49)	23 (8)	42 (14)	3 (1)	13 (4)	43 (13)	75 (18)	452 (110)	232 (56)	67 (16)	68 (16)	7 (2)	5 (1)	12.6 (3.9)
N6946 - Obj 110	197 (71)	24 (8)	43 (14)	1.6 (0.6)	69 (20)	212 (60)	35 (8)	486 (113)	107 (25)	52 (12)	40 (9)	4.2 (1.0)	4 (1)	28.9 (8.4)
N6946 - Obj 115	179 (39)	25 (5)	44 (8)	1.9 (0.5)	25 (4)	76 (13)	43 (6)	480 (71)	159 (23)	51 (7)	37 (5)	2.7 (0.7)	2.0 (0.6)	11.0 (2.0)
N6946 - Obj 117	218 (62)	23 (6)	46 (12)	5 (1)	51 (12)	156 (35)	30 (6)	395 (74)	91 (17)	39 (7)	36 (7)	3.3 (0.6)	3.5 (0.7)	18.3 (4.2)
M 51 - Obj 46	49 (5)	26 (2)	47 (4)	...	2.0 (0.2)	6.0 (0.5)	43 (4)	369 (31)	129 (11)	28 (2)	22 (2)	0.9 (0.2)	...	70.6 (6.3)
M 51 - Obj 57	157 (46)	24 (6)	45 (12)	2.0 (0.5)	27 (6)	82 (19)	56 (11)	413 (79)	174 (33)	33 (6)	27 (5)	1.9 (0.5)	1.1 (0.3)	7.18 (1.70)
M 51 - Obj 73	216 (112)	29 (14)	50 (23)	1.0 (0.7)	9 (4)	30 (12)	49 (16)	343 (112)	152 (50)	47 (15)	37 (12)	4 (1)	...	14.1 (5.9)
M 51 - Obj 94	160 (61)	28 (10)	49 (16)	1.1 (0.4)	7 (2)	20 (6)	47 (11)	333 (81)	138 (34)	28 (7)	20 (5)	0.7 (0.3)	0.6 (0.3)	17.7 (5.4)
M 51 - Obj 100	109 (9)	26 (2)	46 (4)	0.9 (0.2)	7.2 (0.6)	22 (2)	54 (4)	401 (31)	161 (12)	31 (2)	26 (2)	0.9 (0.3)	0.7 (0.2)	207 (16)
M 51 - Obj 101	148 (13)	26 (2)	47 (4)	2.8 (0.3)	11.8 (1.0)	36 (3)	48 (4)	350 (28)	142 (11)	24 (2)	18 (1)	0.6 (0.3)	0.6 (0.2)	12.5 (1.0)
M 51 - Obj 103	181 (51)	24 (6)	45 (11)	3.1 (0.8)	20 (5)	64 (15)	66 (12)	484 (90)	200 (37)	44 (8)	32 (6)	1.9 (0.4)	1.4 (0.4)	8.78 (2.02)

^aThe extinction corrected flux of measured emission lines in comparison to H β , given in the last column with units of 10^{-15} ergs cm⁻² s⁻¹.

Table A5. Emission Line Fluxes for Non-WR Clusters^a

Source	H δ 4102 Å	H γ 4341 Å	[O III] 5007 Å	[N II] 6548 Å	H α 6563 Å	[N II] 6584 Å	H β ^a 4861 Å
NGC 2366 - Object 13	22 (2)	44 (3)	464 (36)	1.5 (0.2)	287 (22)	5.3 (0.4)	34.7 (2.7)
NGC 4449 - Object 3	23 (10)	48 (20)	229 (83)	11 (3)	402 (118)	38 (11)	41.4 (15.3)
NGC 4449 - Object 23	126 (18)	53 (7)	310 (37)	210 (25)	1.24 (0.176)
NGC 4449 - Object 27	32 (36)	66 (71)	119 (113)	10 (7)	467 (355)	32 (24)	21.3 (20.7)
NGC 6946 - Object 37	16 (10)	45 (26)	16 (8)	55 (23)	449 (185)	172 (71)	6.35 (3.32)
M 51 - Object 5	26 (3)	46 (5)	62 (6)	57 (5)	485 (43)	176 (16)	11.8 (1.1)
M 51 - Object 6	21 (6)	43 (11)	17 (4)	68 (13)	440 (85)	208 (40)	11.4 (2.7)
M 51 - Object 11	25 (2)	47 (4)	12 (1)	51 (4)	398 (32)	157 (13)	6.67 (0.56)
M 51 - Object 34	14 (7)	40 (19)	19 (8)	48 (16)	388 (133)	146 (50)	10.6 (4.6)
M 51 - Object 39	12 (7)	39 (22)	22 (11)	39 (16)	383 (153)	123 (49)	26.2 (13.3)
M 51 - Object 44	23 (9)	42 (16)	13 (4)	75 (20)	476 (126)	242 (64)	18.4 (6.1)
M 51 - Object 60	24 (4)	51 (6)	405 (49)	162 (19)	7.47 (1.07)
M 51 - Object 63	...	37 (10)	10 (4)	17 (4)	325 (65)	60 (12)	26.6 (6.7)
M 51 - Object 67	...	41 (10)	14 (3)	38 (6)	387 (61)	120 (19)	11.3 (2.2)
M 51 - Object 88	17 (6)	39 (11)	40 (10)	52 (11)	382 (80)	159 (33)	37.5 (9.8)
M 51 - Object 90	18 (6)	42 (12)	11 (3)	43 (9)	367 (78)	135 (28)	12.4 (3.3)
M 51 - Object 92	20 (5)	46 (11)	19 (4)	50 (9)	362 (64)	158 (28)	10.2 (2.2)
M 51 - Object 93	22 (5)	42 (9)	8 (2)	49 (8)	423 (71)	150 (25)	7.64 (1.57)
M 51 - Object 96	380 (55)	161 (20)	365 (44)	464 (56)	0.977 (0.189)
M 51 - Object 97	20 (9)	43 (18)	16 (6)	71 (21)	488 (143)	225 (66)	52.7 (19.4)
M 51 - Object 105	22 (11)	42 (19)	67 (27)	75 (25)	533 (175)	231 (75)	6.57 (2.73)

^aThe extinction corrected flux of measured emission lines in comparison to H β , given in the last column with units of 10^{-15} ergs cm^{-2} s^{-1} .

Chapter 4

Summary

This thesis demonstrates that WR stars may be a critical (and overlooked) component of in the emerging evolutionary phase of massive star clusters. After observing WR features in an partially-embedded, emerging massive star cluster known as S26 in NGC 4449, I infer that the WR stars may be significant during the evolution of massive star clusters. With my thesis, I investigate WR stars as an overlooked source of feedback that may contribute to the early evolution of massive star clusters. S26 is observed to be currently emerging, with both thermal radio emission and bright optical emission shown in archival *HST* images. While still bright in the radio, optical spectra of S26 unexpectedly show the WR bump, produced by the integrated stellar emission from WR stars. Using the WR feature and ionizing flux, I estimate that S26 hosts ~ 150 massive stars, of which ~ 20 are WR stars; a similar massive star population to other intense star-forming clusters. The presence of WR stars (particularly acknowledging the nature of their strong feedback) during the emerging phase suggests that the WR stars themselves may aid in removing the natal material surrounding S26. Ongoing feedback is evident in *Hubble*, *Spitzer*, and *Herschel Space Telescope* images, where a possible nebular bipolar outflow is seen in the center and conspicuous infrared emission from S26 rivals the nuclear emission of the galaxy at the longest wavelengths. By constructing and fitting the infrared SED with dust models, I find the exciting radiation is more intense and the PAH features are diminished towards the cluster center. This suggests the PAH particles are likely destroyed by the

strong radiation from the massive stars. Thus, it is clear the massive star population in S26, particularly the WR stars, is drastically altering enshrouding natal material. From this multiwavelength analysis of S26, I suggest WR feedback may provide the tipping point in the combined feedback processes that drive a massive star cluster to emerge.

With S26 as inspiration, I conduct an observational survey to search for WR stars in massive star clusters undergoing the same evolutionary transition to assess the role of WR stars in the emergence of massive star clusters. I use a novel method to find clusters undergoing the emerging phase by targeting radio continuum sources with thermal emission, similar to S26. I then obtain optical spectra with the 4m Mayall Telescope at Kitt Peak National Observatory (NOAO) and the 6.5m MMT at the Fred Lawrence Whipple Observatory to search for WR features in each targeted cluster.

I define a sample of 45 emerging massive star clusters in 5 galaxies and observe clear $\geq 3\sigma$ detections of the WR bump in many sources. I classify the sources as either ‘emerging WR clusters’ (WR bump is significantly detected) or as ‘non-WR clusters.’ I show that sources with WR features are not preferentially detected, and identify 21 emerging WR clusters. I find that WR stars are commonly present in massive star clusters undergoing the emerging process, as WR features are detected in 50% of this sample, and that WR stars may make the process of clearing out a cluster more efficient. Using emission line fluxes to probe the local environments, I determine the age, extinction, temperature, density, abundances, and metallicity. Additionally, I use the ionizing flux and the WR feature strengths to provide estimates of the massive star populations in each source. It is clear that the ionizing radiation produced by the massive star populations borders empirical and theoretical predictions for what can be produced by normal star formation alone (Kewley et al. 2001; Kauffmann et al. 2003).

Most intriguing, I find key differences between the emerging WR and Non-WR classes. Sources with the highest extinctions do not host WR stars and have ages past the onset of the WR phase, which may suggest that clusters without significant populations of WR stars stay embedded for longer periods of time or that WR stars

make the process of clearing out a cluster more efficient. This scenario is in agreement with my hypothesis derived from S26 that WR stars are important for a cluster to emerge, and my survey has revealed a possible acceleration of cluster emergence due to WR stars. Thus, my research has shown that WR stars are likely important in the emerging evolutionary transition of massive star clusters.

Looking forward, there is follow up that could be done to confirm the importance of WR feedback, from better models to new observations. It is not yet feasible to simulate all the factors involved in the evolution of massive star clusters, which would ultimately require the inclusion of all the different feedback processes, stellar evolution, and a complete range of cluster masses. Yet, we are seeing huge improvements in the quality and capabilities already. For instance, Skinner & Ostriker (2015) have modeled the effects of radiation feedback on a nascent super star cluster – one of the first simulations to reach the upper end of the cluster mass scale. Additionally, an improved version of a simulation of massive star cluster formation, which already includes many processes such as heating of dust by collisions, radiative cooling, and stellar winds (Rosen 2015), will include the WR phases (private comm. with A. Rosen). While these simulations certainly increase our understanding of the evolution of massive star clusters, especially as they become more complex and inclusive, they need to be paired with further observations as well.

My thesis is drawn from a beautiful dataset, but the intrinsic complexity of these regions and the various ongoing physics makes interpreting their evolutionary state quite difficult and leaves many uncertainties. More examples of emerging massive star clusters need to be found, along with observations searching for the WR signal; yet as mentioned in Section 3.8, the new surveys with the Karl G. Jansky VLA and additional future radio observations make identifying new targets an actual possibility. Furthermore, observations of the kinematics of the gas within these clusters could confirm these clusters are being observed at a stage while the emerging phase is currently action. Broadened Brackett lines have been observed in massive star clusters in the Antennae galaxy that indicate outflows and that the clusters are clearing their natal gas (Gilbert & Graham 2007). Similar observations of my sample will enable the characterization of the motions of the gas to search for differences in the kinematics

between my sample clusters with and without WR stars, possibly identifying how the gas is being expelled in each case. Utilizing near infrared observations will determine the gas kinematics even in clusters that have high extinction in the optical, pushing earlier into the evolutionary sequence of these extreme regions. NASA's upcoming James Webb Space Telescope will be able to observe farther distances, and will enable the study of massive star cluster evolution beyond nearby galaxies and potentially at the high redshift regime.

References

- Abbott, D. C. 1982, *ApJ*, 263, 723
- Agertz, O., Kravtsov, A. V., Leitner, S. N., & Gnedin, N. Y. 2013, *ApJ*, 770, 25
- Aniano, G., Draine, B. T., Gordon, K. D., & Sandstrom, K. 2011, *PASP*, 123, 1218
- Annibali, F., Aloisi, A., Mack, J., Tosi, M., van der Marel, R. P., Angeretti, L.,
Leitherer, C., & Sirianni, M. 2008, *AJ*, 135, 1900
- Arp, H. & Sandage, A. 1985, *AJ*, 90, 1163
- Ashman, K. M. & Zepf, S. E. 2001, *AJ*, 122, 1888
- Asplund, M., Grevesse, N., Sauval, A. J., & Scott, P. 2009, *ARA&A*, 47, 481
- Aversa, A. G., Johnson, K. E., Brogan, C. L., Goss, W. M., & Pisano, D. J. 2011,
AJ, 141, 125
- Baars, J. W. M., Genzel, R., Pauliny-Toth, I. I. K., & Witzel, A. 1977, *A&A*, 61, 99
- Bachiller, R. 1996, *ARA&A*, 34, 111
- Baldwin, J. A., Phillips, M. M., & Terlevich, R. 1981, *PASP*, 93, 5
- Balog, Z., Müller, T., Nielbock, M., Altieri, B., Klaas, U., Blommaert, J., Linz, H.,
Lutz, D., Moór, A., Billot, N., Sauvage, M., & Okumura, K. 2014, *Experimental
Astronomy*, 37, 129
- Banerjee, S. & Kroupa, P. 2015, *ArXiv e-prints*

- Barth, A. J., Ho, L. C., Filippenko, A. V., Gorjian, V., Malkan, M., & Sargent, W. L. W. 1996, in *Astronomical Society of the Pacific Conference Series*, Vol. 91, IAU Colloq. 157: Barred Galaxies, ed. R. Buta, D. A. Crocker, & B. G. Elmegreen, 94
- Bastian, N., Adamo, A., Gieles, M., Silva-Villa, E., Lamers, H. J. G. L. M., Larsen, S. S., Smith, L. J., Konstantopoulos, I. S., & Zackrisson, E. 2012, *MNRAS*, 419, 2606
- Bastian, N., Covey, K. R., & Meyer, M. R. 2010, *ARA&A*, 48, 339
- Bastian, N., Hollyhead, K., & Cabrera-Ziri, I. 2014, *MNRAS*, 445, 378
- Baumgardt, H. & Kroupa, P. 2007, *MNRAS*, 380, 1589
- Benedict, G. F., Higdon, J. L., Jefferys, W. H., Duncombe, R., Hemenway, P. D., Shelus, P. J., Whipple, A. L., Nelan, E., Story, D., McArthur, B., McCartney, J., Franz, O. G., Fredrick, L. W., & van Altena, W. F. 1993, *AJ*, 105, 1369
- Bibby, J. L. & Crowther, P. A. 2010, *MNRAS*, 405, 2737
- . 2012, *MNRAS*, 420, 3091
- Bonnell, I. A., Bate, M. R., & Zinnecker, H. 1998, *MNRAS*, 298, 93
- Brinchmann, J., Pettini, M., & Charlot, S. 2008, *MNRAS*, 385, 769
- Calura, F., Few, C. G., Romano, D., & D’Ercole, A. 2015, *ApJ*, 814, L14
- Calzetti, D., Kinney, A. L., & Storchi-Bergmann, T. 1994, *ApJ*, 429, 582
- Cao, Y., Kasliwal, M. M., Arcavi, I., Horesh, A., Hancock, P., Valenti, S., Cenko, S. B., Kulkarni, S. R., Gal-Yam, A., Gorbikov, E., Ofek, E. O., Sand, D., Yaron, O., Graham, M., Silverman, J. M., Wheeler, J. C., Marion, G. H., Walker, E. S., Mazzali, P., Howell, D. A., Li, K. L., Kong, A. K. H., Bloom, J. S., Nugent, P. E., Surace, J., Masci, F., Carpenter, J., Degenaar, N., & Gelino, C. R. 2013, *ApJ*, 775, L7

- Cappa, C., Goss, W. M., & van der Hucht, K. A. 2004, *AJ*, 127, 2885
- Cecil, G., Bland-Hawthorn, J., Veilleux, S., & Filippenko, A. V. 2001, *ApJ*, 555, 338
- Cerviño, M., Román-Zúñiga, C., Luridiana, V., Bayo, A., Sánchez, N., & Pérez, E. 2013, *A&A*, 553, A31
- Chandar, R., Fall, S. M., & Whitmore, B. C. 2006, *ApJ*, 650, L111
- Chandar, R., Leitherer, C., & Tremonti, C. A. 2004, *ApJ*, 604, 153
- Chandar, R., Whitmore, B. C., Kim, H., Kaleida, C., Mutchler, M., Calzetti, D., Saha, A., O'Connell, R., Balick, B., Bond, H., Carollo, M., Disney, M., Dopita, M. A., Frogel, J. A., Hall, D., Holtzman, J. A., Kimble, R. A., McCarthy, P., Paresce, F., Silk, J., Trauger, J., Walker, A. R., Windhorst, R. A., & Young, E. 2010, *ApJ*, 719, 966
- Chomiuk, L. & Wilcots, E. M. 2009, *AJ*, 137, 3869
- Churchwell, E. 2002, *ARA&A*, 40, 27
- Ciardullo, R., Feldmeier, J. J., Jacoby, G. H., Kuzio de Naray, R., Laychak, M. B., & Durrell, P. R. 2002, *ApJ*, 577, 31
- Condon, J. J. 1992, *ARA&A*, 30, 575
- Conti, P. S. 1976, *Mom. Soc. Roy. des Sciences de Liege*, sixth serie, 9, 193
- . 1991, *ApJ*, 377, 115
- Conti, P. S. 1993, in *Astronomical Society of the Pacific Conference Series*, Vol. 35, *Massive Stars: Their Lives in the Interstellar Medium*, ed. J. P. Cassinelli & E. B. Churchwell, 449
- Conti, P. S., Garmany, C. D., De Loore, C., & Vanbeveren, D. 1983, *ApJ*, 274, 302

- Corsi, A., Ofek, E. O., Gal-Yam, A., Frail, D. A., Poznanski, D., Mazzali, P. A., Kulkarni, S. R., Kasliwal, M. M., Arcavi, I., Ben-Ami, S., Cenko, S. B., Filippenko, A. V., Fox, D. B., Horesh, A., Howell, J. L., Kleiser, I. K. W., Nakar, E., Rabinak, I., Sari, R., Silverman, J. M., Xu, D., Bloom, J. S., Law, N. M., Nugent, P. E., & Quimby, R. M. 2012, *ApJ*, 747, L5
- Crowther, P. A. 2007, *ARA&A*, 45, 177
- Crowther, P. A. & Bibby, J. L. 2009, *A&A*, 499, 455
- Crowther, P. A. & Hadfield, L. J. 2006, *A&A*, 449, 711
- Crowther, P. A., Hillier, D. J., & Smith, L. J. 1995, *A&A*, 293
- Crowther, P. A. & Walborn, N. R. 2011, *MNRAS*, 416, 1311
- Cunningham, A. J., Klein, R. I., Krumholz, M. R., & McKee, C. F. 2011, *ApJ*, 740, 107
- Dale, J. E., Bonnell, I. A., Clarke, C. J., & Bate, M. R. 2005, *MNRAS*, 358, 291
- Dale, J. E., Ngoumou, J., Ercolano, B., & Bonnell, I. A. 2014, *MNRAS*, 442, 694
- de Grijs, R. 2004, in *Astronomical Society of the Pacific Conference Series*, Vol. 322, *The Formation and Evolution of Massive Young Star Clusters*, ed. H. J. G. L. M. Lamers, L. J. Smith, & A. Nota, 29
- De Marchi, G. & Panagia, N. 2014, *MNRAS*, 445, 93
- De Marchi, G., Paresce, F., Panagia, N., Beccari, G., Spezzi, L., Sirianni, M., Andersen, M., Mutchler, M., Balick, B., Dopita, M. A., Frogel, J. A., Whitmore, B. C., Bond, H., Calzetti, D., Carollo, C. M., Disney, M. J., Hall, D. N. B., Holtzman, J. A., Kimble, R. A., McCarthy, P. J., O'Connell, R. W., Saha, A., Silk, J. I., Trauger, J. T., Walker, A. R., Windhorst, R. A., & Young, E. T. 2011, *ApJ*, 739, 27

- De Pree, C. G., Wilner, D. J., Deblasio, J., Mercer, A. J., & Davis, L. E. 2005, *ApJ*, 624, L101
- De Robertis, M. M., Dufour, R. J., & Hunt, R. W. 1987, *JRASC*, 81, 195
- Doran, E. I., Crowther, P. A., de Koter, A., Evans, C. J., McEvoy, C., Walborn, N. R., Bastian, N., Bestenlehner, J. M., Gräfener, G., Herrero, A., Köhler, K., Maíz Apellániz, J., Najarro, F., Puls, J., Sana, H., Schneider, F. R. N., Taylor, W. D., van Loon, J. T., & Vink, J. S. 2013, *A&A*, 558, A134
- Draine, B. T. & Li, A. 2007, *ApJ*, 657, 810
- Ekström, S., Georgy, C., Eggenberger, P., Meynet, G., Mowlavi, N., Wyttenbach, A., Granada, A., Decressin, T., Hirschi, R., Frischknecht, U., Charbonnel, C., & Maeder, A. 2012, *A&A*, 537, A146
- Eldridge, J. J. 2008, *Philosophical Transactions of the Royal Society of London Series A*, 366, 4441
- Eldridge, J. J., Fraser, M., Smartt, S. J., Maund, J. R., & Crockett, R. M. 2013, *MNRAS*, 436, 774
- Eldridge, J. J., Izzard, R. G., & Tout, C. A. 2008, *MNRAS*, 384, 1109
- Eldridge, J. J. & Stanway, E. R. 2009, *MNRAS*, 400, 1019
- Eldridge, J. J. & Vink, J. S. 2006, *A&A*, 452, 295
- Engelbracht, C. W., Blaylock, M., Su, K. Y. L., Rho, J., Rieke, G. H., Muzerolle, J., Padgett, D. L., Hines, D. C., Gordon, K. D., Fadda, D., Noriega-Crespo, A., Kelly, D. M., Latter, W. B., Hinz, J. L., Misselt, K. A., Morrison, J. E., Stansberry, J. A., Shupe, D. L., Stolovy, S., Wheaton, W. A., Young, E. T., Neugebauer, G., Wachter, S., Pérez-González, P. G., Frayer, D. T., & Marleau, F. R. 2007, *PASP*, 119, 994
- Evans, II, N. J. 1999, *ARA&A*, 37, 311

- Fabricant, D., Fata, R., Roll, J., Hertz, E., Caldwell, N., Gauron, T., Geary, J., McLeod, B., Szentgyorgyi, A., Zajac, J., Kurtz, M., Barberis, J., Bergner, H., Brown, W., Conroy, M., Eng, R., Geller, M., Goddard, R., Honsa, M., Mueller, M., Mink, D., Ordway, M., Tokarz, S., Woods, D., Wyatt, W., Epps, H., & Dell'Antonio, I. 2005, *PASP*, 117, 1411
- Fall, S. M. 2004, in *Astronomical Society of the Pacific Conference Series*, Vol. 322, *The Formation and Evolution of Massive Young Star Clusters*, ed. H. J. G. L. M. Lamers, L. J. Smith, & A. Nota, 399
- Fall, S. M. & Chandar, R. 2012, *ApJ*, 752, 96
- Fall, S. M., Chandar, R., & Whitmore, B. C. 2009, *ApJ*, 704, 453
- Fall, S. M., Krumholz, M. R., & Matzner, C. D. 2010, *ApJ*, 710, L142
- Fazio, G. G., Hora, J. L., Allen, L. E., Ashby, M. L. N., Barmby, P., Deutsch, L. K., Huang, J.-S., Kleiner, S., Marengo, M., Megeath, S. T., Melnick, G. J., Pahre, M. A., Patten, B. M., Polizotti, J., Smith, H. A., Taylor, R. S., Wang, Z., Willner, S. P., Hoffmann, W. F., Pipher, J. L., Forrest, W. J., McMurty, C. W., McCreight, C. R., McKelvey, M. E., McMurray, R. E., Koch, D. G., Moseley, S. H., Arendt, R. G., Mentzell, J. E., Marx, C. T., Losch, P., Mayman, P., Eichhorn, W., Krebs, D., Jhabvala, M., Gezari, D. Y., Fixsen, D. J., Flores, J., Shakoorzadeh, K., Jungo, R., Hakun, C., Workman, L., Karpati, G., Kichak, R., Whitley, R., Mann, S., Tollestrup, E. V., Eisenhardt, P., Stern, D., Gorjian, V., Bhattacharya, B., Carey, S., Nelson, B. O., Glaccum, W. J., Lacy, M., Lowrance, P. J., Laine, S., Reach, W. T., Stauffer, J. A., Surace, J. A., Wilson, G., Wright, E. L., Hoffman, A., Domingo, G., & Cohen, M. 2004, *ApJS*, 154, 10
- Fierlinger, K. M., Burkert, A., Ntormousi, E., Fierlinger, P., Schartmann, M., Balone, A., Krause, M. G. H., & Diehl, R. 2016, *MNRAS*, 456, 710
- Fitzpatrick, E. L. 1985, *ApJ*, 299, 219
- Fouesneau, M. & Lançon, A. 2010, *A&A*, 521, A22

- Freyer, T., Hensler, G., & Yorke, H. W. 2003, *ApJ*, 594, 888
- . 2006, *ApJ*, 638, 262
- Fritz, J., Gentile, G., Smith, M. W. L., Gear, W. K., Braun, R., Duval, J. R., Bendo, G. J., Baes, M., Eales, S. A., Verstappen, J., Blommaert, J. A. D. L., Boquien, M., Boselli, A., Clements, D., Cooray, A. R., Cortese, L., De Looze, I., Ford, G. P., Galliano, F., Gomez, H. L., Gordon, K. D., Lebouteiller, V., O'Halloran, B., Kirk, J., Madden, S. C., Page, M. J., Remy, A., Roussel, H., Spinoglio, L., Thilker, D., Vaccari, M., Wilson, C. D., & Waelkens, C. 2012, *A&A*, 546, A34
- Fryer, C. L. 1999, *ApJ*, 522, 413
- Gal-Yam, A., Arcavi, I., Ofek, E. O., Ben-Ami, S., Cenko, S. B., Kasliwal, M. M., Cao, Y., Yaron, O., Tal, D., Silverman, J. M., Horesh, A., De Cia, A., Taddia, F., Sollerman, J., Perley, D., Vreeswijk, P. M., Kulkarni, S. R., Nugent, P. E., Filippenko, A. V., & Wheeler, J. C. 2014, *Nature*, 509, 471
- Galliano, E., Alloin, D., Pantin, E., Granato, G. L., Delva, P., Silva, L., Lagage, P. O., & Panuzzo, P. 2008, *A&A*, 492, 3
- Gamow, G. 1943, *ApJ*, 98, 500
- Georgy, C., Ekström, S., Eggenberger, P., Meynet, G., Haemmerlé, L., Maeder, A., Granada, A., Groh, J. H., Hirschi, R., Mowlavi, N., Yusof, N., Charbonnel, C., Decressin, T., & Barblan, F. 2013, *A&A*, 558, A103
- Georgy, C., Ekström, S., Hirschi, R., Meynet, G., Groh, J. H., & Eggenberger, P. 2015, in *Wolf-Rayet Stars: Proceedings of an International Workshop held in Potsdam, Germany, 1-5 June 2015*. Edited by Wolf-Rainer Hamann, Andreas Sander, Helge Todt. Universitätsverlag Potsdam, 2015., p.229-232, ed. W.-R. Hamann, A. Sander, & H. Todt, 229–232
- Georgy, C., Ekström, S., Meynet, G., Massey, P., Levesque, E. M., Hirschi, R., Eggenberger, P., & Maeder, A. 2012, *A&A*, 542, A29

- Gieles, M., Lamers, H. J. G. L. M., & Portegies Zwart, S. F. 2007, *ApJ*, 668, 268
- Gilbert, A. M. & Graham, J. R. 2007, *ApJ*, 668, 168
- Gnedin, O. Y. & Ostriker, J. P. 1997, *ApJ*, 474, 223
- González Delgado, R. M., Leitherer, C., Heckman, T., & Cerviño, M. 1997, *ApJ*, 483, 705
- González Delgado, R. M., Leitherer, C., Stasińska, G., & Heckman, T. M. 2002, *ApJ*, 580, 824
- Green, D. A. 1998, *VizieR Online Data Catalog*, 7211
- Griffin, M. J., Abergel, A., Abreu, A., Ade, P. A. R., André, P., Augeres, J.-L., Babbedge, T., Bae, Y., Baillie, T., Baluteau, J.-P., Barlow, M. J., Bendo, G., Benielli, D., Bock, J. J., Bonhomme, P., Brisbin, D., Brockley-Blatt, C., Caldwell, M., Cara, C., Castro-Rodriguez, N., Cerulli, R., Chanial, P., Chen, S., Clark, E., Clements, D. L., Clerc, L., Coker, J., Communal, D., Conversi, L., Cox, P., Crumb, D., Cunningham, C., Daly, F., Davis, G. R., de Antoni, P., Delderfield, J., Devin, N., di Giorgio, A., Didschuns, I., Dohlen, K., Donati, M., Dowell, A., Dowell, C. D., Duband, L., Dumaye, L., Emery, R. J., Ferlet, M., Ferrand, D., Fontignie, J., Fox, M., Franceschini, A., Frerking, M., Fulton, T., Garcia, J., Gastaud, R., Gear, W. K., Glenn, J., Goizel, A., Griffin, D. K., Grundy, T., Guest, S., Guillemet, L., Hargrave, P. C., Harwit, M., Hastings, P., Hatziminaoglou, E., Herman, M., Hinde, B., Hristov, V., Huang, M., Imhof, P., Isaak, K. J., Israelsson, U., Ivison, R. J., Jennings, D., Kiernan, B., King, K. J., Lange, A. E., Latter, W., Laurent, G., Laurent, P., Leeks, S. J., Lellouch, E., Levenson, L., Li, B., Li, J., Lilienthal, J., Lim, T., Liu, S. J., Lu, N., Madden, S., Mainetti, G., Marliani, P., McKay, D., Mercier, K., Molinari, S., Morris, H., Moseley, H., Mulder, J., Mur, M., Naylor, D. A., Nguyen, H., O'Halloran, B., Oliver, S., Olofsson, G., Olofsson, H.-G., Orfei, R., Page, M. J., Pain, I., Panuzzo, P., Papageorgiou, A., Parks, G., Parr-Burman, P., Pearce, A., Pearson, C., Pérez-Fournon, I., Pinsard, F., Pisano, G., Podosek, J., Pohlen, M., Polehampton, E. T., Pouliquen, D., Rigopoulou, D., Rizzo, D., Roseboom, I. G.,

- Roussel, H., Rowan-Robinson, M., Rownd, B., Saraceno, P., Sauvage, M., Savage, R., Savini, G., Sawyer, E., Scharnberg, C., Schmitt, D., Schneider, N., Schulz, B., Schwartz, A., Shafer, R., Shupe, D. L., Sibthorpe, B., Sidher, S., Smith, A., Smith, A. J., Smith, D., Spencer, L., Stobie, B., Sudiwala, R., Sukhatme, K., Surace, C., Stevens, J. A., Swinyard, B. M., Trichas, M., Tourette, T., Triou, H., Tseng, S., Tucker, C., Turner, A., Vaccari, M., Valtchanov, I., Vigroux, L., Virique, E., Voellmer, G., Walker, H., Ward, R., Waskett, T., Weilert, M., Wesson, R., White, G. J., Whitehouse, N., Wilson, C. D., Winter, B., Woodcraft, A. L., Wright, G. S., Xu, C. K., Zavagno, A., Zemcov, M., Zhang, L., & Zonca, E. 2010, *A&A*, 518, L3
- Groh, J. H. 2014, *A&A*, 572, L11
- Groh, J. H., Meynet, G., Ekström, S., & Georgy, C. 2014, *A&A*, 564, A30
- Guseva, N. G., Izotov, Y. I., & Thuan, T. X. 2000, *ApJ*, 531, 776
- Hadfield, L. J. & Crowther, P. A. 2006, *MNRAS*, 368, 1822
- . 2007, *MNRAS*, 381, 418
- Hadfield, L. J. & Crowther, P. A. 2008, in *IAU Symposium*, Vol. 250, *IAU Symposium*, ed. F. Bresolin, P. A. Crowther, & J. Puls, 327–332
- Hainich, R., Pasemann, D., Todt, H., Shenar, T., Sander, A., & Hamann, W.-R. 2015, *A&A*, 581, A21
- Hainich, R., Rühling, U., Todt, H., Oskinova, L. M., Liermann, A., Gräfener, G., Foellmi, C., Schnurr, O., & Hamann, W.-R. 2014, *A&A*, 565, A27
- Heckman, T. M., Dahlem, M., Lehnert, M. D., Fabbiano, G., Gilmore, D., & Waller, W. H. 1995, *ApJ*, 448, 98
- Heesen, V., Brinks, E., Krause, M. G. H., Harwood, J. J., Rau, U., Rupen, M. P., Hunter, D. A., Chyży, K. T., & Kitchener, G. 2015, *MNRAS*, 447, L1
- Hillier, D. J. & Miller, D. L. 1998, *ApJ*, 496, 407

- . 1999, *ApJ*, 519, 354
- Ho, L. C. 1997, in *Revista Mexicana de Astronomia y Astrofisica Conference Series*, Vol. 6, *Revista Mexicana de Astronomia y Astrofisica Conference Series*, ed. J. Franco, R. Terlevich, & A. Serrano, 5
- Hodge, P. W. 1961, *ApJ*, 133, 413
- Hollyhead, K., Bastian, N., Adamo, A., Silva-Villa, E., Dale, J., Ryon, J. E., & Gazak, Z. 2015, *MNRAS*, 449, 1106
- Holtzman, J. A., Faber, S. M., Shaya, E. J., Lauer, T. R., Groth, J., Hunter, D. A., Baum, W. A., Ewald, S. P., Hester, J. J., Light, R. M., Lynds, C. R., O’Neil, Jr., E. J., & Westphal, J. A. 1992, *AJ*, 103, 691
- Huggins, W. & Huggins, M. 1890, *Proceedings of the Royal Society of London Series I*, 49, 33
- Hunt, L. K. & Hirashita, H. 2009, *A&A*, 507, 1327
- Hunter, D. A., O’Connell, R. W., & Gallagher, III, J. S. 1994, *AJ*, 108, 84
- Hunter, D. A., Shaya, E. J., Holtzman, J. A., Light, R. M., O’Neil, Jr., E. J., & Lynds, R. 1995, *ApJ*, 448, 179
- Hyman, S. D., Lacey, C. K., Weiler, K. W., & Van Dyk, S. D. 2000, *AJ*, 119, 1711
- Izotov, Y. I., Stasińska, G., Meynet, G., Guseva, N. G., & Thuan, T. X. 2006, *A&A*, 448, 955
- Izotov, Y. I., Thuan, T. X., & Lipovetsky, V. A. 1994, *ApJ*, 435, 647
- . 1997, *ApJS*, 108, 1
- Jaskot, A. E. & Oey, M. S. 2013, *ApJ*, 766, 91
- Johnson, K. 2002, *Science*, 297, 776
- Johnson, K. E., Hunt, L. K., & Reines, A. E. 2009, *AJ*, 137, 3788

- Johnson, K. E., Indebetouw, R., Watson, C., & Kobulnicky, H. A. 2004, *AJ*, 128, 610
- Johnson, K. E. & Kobulnicky, H. A. 2003, *ApJ*, 597, 923
- Karczewski, O. L., Barlow, M. J., Page, M. J., Kuin, N. P. M., Ferreras, I., Baes, M., Bendo, G. J., Boselli, A., Cooray, A., Cormier, D., De Looze, I., Galametz, M., Galliano, F., Lebouteiller, V., Madden, S. C., Pohlen, M., Rémy-Ruyer, A., Smith, M. W. L., & Spinoglio, L. 2013, *MNRAS*, 431, 2493
- Kauffmann, G., Heckman, T. M., Tremonti, C., Brinchmann, J., Charlot, S., White, S. D. M., Ridgway, S. E., Brinkmann, J., Fukugita, M., Hall, P. B., Ivezić, Ž., Richards, G. T., & Schneider, D. P. 2003, *MNRAS*, 346, 1055
- Kehrig, C., Pérez-Montero, E., Vílchez, J. M., Brinchmann, J., Kunth, D., García-Benito, R., Crowther, P. A., Hernández-Fernández, J., Durret, F., Contini, T., Fernández-Martín, A., & James, B. L. 2013, *MNRAS*, 432, 2731
- Kennicutt, Jr., R. C., Armus, L., Bendo, G., Calzetti, D., Dale, D. A., Draine, B. T., Engelbracht, C. W., Gordon, K. D., Grauer, A. D., Helou, G., Hollenbach, D. J., Jarrett, T. H., Kewley, L. J., Leitherer, C., Li, A., Malhotra, S., Regan, M. W., Rieke, G. H., Rieke, M. J., Roussel, H., Smith, J.-D. T., Thornley, M. D., & Walter, F. 2003, *PASP*, 115, 928
- Kepley, A. A., Reines, A. E., Johnson, K. E., & Walker, L. M. 2014, *AJ*, 147, 43
- Kewley, L. J., Dopita, M. A., Sutherland, R. S., Heisler, C. A., & Trevena, J. 2001, *ApJ*, 556, 121
- Kim, S., Staveley-Smith, L., Dopita, M. A., Sault, R. J., Freeman, K. C., Lee, Y., & Chu, Y.-H. 2003, *ApJS*, 148, 473
- Kobulnicky, H. A. & Johnson, K. E. 1999, *ApJ*, 527, 154
- Kobulnicky, H. A. & Kewley, L. J. 2004, *ApJ*, 617, 240
- Kroupa, P. 2001, *MNRAS*, 322, 231

- Kroupa, P., Aarseth, S., & Hurley, J. 2001, MNRAS, 321, 699
- Krumholz, M. R., Bate, M. R., Arce, H. G., Dale, J. E., Gutermuth, R., Klein, R. I., Li, Z.-Y., Nakamura, F., & Zhang, Q. 2014, Protostars and Planets VI, 243
- Krumholz, M. R., Fumagalli, M., da Silva, R. L., Rendahl, T., & Parra, J. 2015, MNRAS, 452, 1447
- Krumholz, M. R. & Matzner, C. D. 2009, ApJ, 703, 1352
- Kudritzki, R.-P. & Puls, J. 2000, ARA&A, 38, 613
- Lacey, C., Duric, N., & Goss, W. M. 1997, ApJS, 109, 417
- Lada, C. J. & Lada, E. A. 1991, in Astronomical Society of the Pacific Conference Series, Vol. 13, The Formation and Evolution of Star Clusters, ed. K. Janes, 3–22
- Lada, C. J. & Lada, E. A. 2003, ARA&A, 41, 57
- Langer, N., Hamann, W.-R., Lennon, M., Najarro, F., Pauldrach, A. W. A., & Puls, J. 1994, A&A, 290
- Larsen, S. S. 2004, in Astronomical Society of the Pacific Conference Series, Vol. 322, The Formation and Evolution of Massive Young Star Clusters, ed. H. J. G. L. M. Lamers, L. J. Smith, & A. Nota, 19
- Larsen, S. S. & Richtler, T. 2000, A&A, 354, 836
- Lee, J. C., Gil de Paz, A., Tremonti, C., Kennicutt, Jr., R. C., Salim, S., Bothwell, M., Calzetti, D., Dalcanton, J., Dale, D., Engelbracht, C., Funes, S. J. J. G., Johnson, B., Sakai, S., Skillman, E., van Zee, L., Walter, F., & Weisz, D. 2009, ApJ, 706, 599
- Leitherer, C. 1999, in IAU Symposium, Vol. 193, Wolf-Rayet Phenomena in Massive Stars and Starburst Galaxies, ed. K. A. van der Hucht, G. Koenigsberger, & P. R. J. Eenens, 526

- Leitherer, C., Ekström, S., Meynet, G., Schaerer, D., Agienko, K. B., & Levesque, E. M. 2014, *ApJS*, 212, 14
- Leitherer, C., Schaerer, D., Goldader, J. D., Delgado, R. M. G., Robert, C., Kune, D. F., de Mello, D. F., Devost, D., & Heckman, T. M. 1999, *ApJS*, 123, 3
- Leloudas, G., Sollerman, J., Levan, A. J., Fynbo, J. P. U., Malesani, D., & Maund, J. R. 2010, *A&A*, 518, A29
- Lequeux, J., Peimbert, M., Rayo, J. F., Serrano, A., & Torres-Peimbert, S. 1979, *A&A*, 80, 155
- Liu, Q.-Z., Hu, J.-Y., Hang, H.-R., Qiu, Y.-L., Zhu, Z.-X., & Qiao, Q.-Y. 2000, *A&AS*, 144, 219
- Lopez, L. A., Krumholz, M. R., Bolatto, A. D., Prochaska, J. X., & Ramirez-Ruiz, E. 2011, *ApJ*, 731, 91
- Lopez, L. A., Krumholz, M. R., Bolatto, A. D., Prochaska, J. X., Ramirez-Ruiz, E., & Castro, D. 2014, *ApJ*, 795, 121
- Lutz, D. 1991, *A&A*, 245, 31
- Madden, S. C., Rémy-Ruyer, A., Galametz, M., Cormier, D., Lebouteiller, V., Galiano, F., Hony, S., Bendo, G. J., Smith, M. W. L., Pohlen, M., Roussel, H., Sauvage, M., Wu, R., Sturm, E., Poglitsch, A., Contursi, A., Doublier, V., Baes, M., Barlow, M. J., Boselli, A., Boquien, M., Carlson, L. R., Ciesla, L., Cooray, A., Cortese, L., de Looze, I., Irwin, J. A., Isaak, K., Kamenetzky, J., Karczewski, O. L., Lu, N., MacHattie, J. A., O'Halloran, B., Parkin, T. J., Rangwala, N., Schirm, M. R. P., Schulz, B., Spinoglio, L., Vaccari, M., Wilson, C. D., & Wozniak, H. 2013, *PASP*, 125, 600
- Maddox, L. A., Cowan, J. J., Kilgard, R. E., Schinnerer, E., & Stockdale, C. J. 2007, *AJ*, 133, 2559
- Maeder, A. 1983, *A&A*, 120, 113

- Maeder, A. & Conti, P. S. 1994, *ARA&A*, 32, 227
- Martins, F., Schaerer, D., & Hillier, D. J. 2005, *A&A*, 436, 1049
- Massey, P. 1996, in *Liege International Astrophysical Colloquia*, Vol. 33, *Liege International Astrophysical Colloquia*, ed. J. M. Vreux, A. Detal, D. Fraipont-Caro, E. Gosset, & G. Rauw, 361
- Massey, P. 2003, *ARA&A*, 41, 15
- Massey, P. 2011, in *Astronomical Society of the Pacific Conference Series*, Vol. 440, *UP2010: Have Observations Revealed a Variable Upper End of the Initial Mass Function?*, ed. M. Treyer, T. Wyder, J. Neill, M. Seibert, & J. Lee, 29
- . 2013, *NewAr*, 57, 14
- Massey, P. & Holmes, S. 2002, *ApJ*, 580, L35
- Massey, P. & Hunter, D. A. 1998, *ApJ*, 493, 180
- Massey, P. & Johnson, O. 1998, *ApJ*, 505, 793
- Mathis, J. S., Mezger, P. G., & Panagia, N. 1983, *A&A*, 128, 212
- Matzner, C. D. 2002, *ApJ*, 566, 302
- . 2007, *ApJ*, 659, 1394
- Melnick, J. & D’Odorico, S. 1978, *A&AS*, 34, 249
- Melnick, J., Moles, M., & Terlevich, R. 1985, *A&A*, 149, L24
- Meynet, G., Georgy, C., Maeder, A., Ekström, S., Groh, J. H., Barblan, F., Song, H. F., & Eggenberger, P. 2016, *ArXiv e-prints*
- Meynet, G. & Maeder, A. 2005, *A&A*, 429, 581

- Mink, D. J., Wyatt, W. F., Caldwell, N., Conroy, M. A., Furesz, G., & Tokarz, S. P. 2007, in *Astronomical Society of the Pacific Conference Series*, Vol. 376, *Astronomical Data Analysis Software and Systems XVI*, ed. R. A. Shaw, F. Hill, & D. J. Bell, 249
- Misselt, K. A., Clayton, G. C., & Gordon, K. D. 1999, *ApJ*, 515, 128
- Mokiem, M. R., de Koter, A., Vink, J. S., Puls, J., Evans, C. J., Smartt, S. J., Crowther, P. A., Herrero, A., Langer, N., Lennon, D. J., Najarro, F., & Villamariz, M. R. 2007, *A&A*, 473, 603
- Moll, S. L., Mengel, S., de Grijs, R., Smith, L. J., & Crowther, P. A. 2007, *MNRAS*, 382, 1877
- Murphy, E. J., Bremseth, J., Mason, B. S., Condon, J. J., Schinnerer, E., Aniano, G., Armus, L., Helou, G., Turner, J. L., & Jarrett, T. H. 2012, *ApJ*, 761, 97
- Murray, N., Quataert, E., & Thompson, T. A. 2010, *ApJ*, 709, 191
- Nakajima, K. & Ouchi, M. 2014, *MNRAS*, 442, 900
- Neugent, K. F. & Massey, P. 2011, *ApJ*, 733, 123
- Neugent, K. F., Massey, P., & Georgy, C. 2012, *ApJ*, 759, 11
- O'Connell, R. W., Gallagher, III, J. S., & Hunter, D. A. 1994, *ApJ*, 433, 65
- O'Connell, R. W., Gallagher, III, J. S., Hunter, D. A., & Colley, W. N. 1995, *ApJ*, 446, L1
- Pauldrach, A. W. A., Lennon, M., Hoffmann, T. L., Sellmaier, F., Kudritzki, R.-P., & Puls, J. 1998, in *Astronomical Society of the Pacific Conference Series*, Vol. 131, *Properties of Hot Luminous Stars*, ed. I. Howarth, 258
- Pellegrini, E. W., Baldwin, J. A., & Ferland, G. J. 2011, *ApJ*, 738, 34
- Pfalzner, S. & Kaczmarek, T. 2013, *A&A*, 559, A38

- Pilbratt, G. L., Riedinger, J. R., Passvogel, T., Crone, G., Doyle, D., Gageur, U., Heras, A. M., Jewell, C., Metcalfe, L., Ott, S., & Schmidt, M. 2010, *A&A*, 518, L1
- Poglitsch, A., Waelkens, C., Geis, N., Feuchtgruber, H., Vandenbussche, B., Rodriguez, L., Krause, O., Renotte, E., van Hoof, C., Saraceno, P., Cepa, J., Kerschbaum, F., Agnèse, P., Ali, B., Altieri, B., Andreani, P., Augueres, J.-L., Balog, Z., Barl, L., Bauer, O. H., Belbachir, N., Benedettini, M., Billot, N., Boulade, O., Bischof, H., Blommaert, J., Callut, E., Cara, C., Cerulli, R., Cesarsky, D., Contursi, A., Creten, Y., De Meester, W., Doublier, V., Doumayrou, E., Duband, L., Exter, K., Genzel, R., Gillis, J.-M., Grözinger, U., Henning, T., Herreros, J., Huygen, R., Inguscio, M., Jakob, G., Jamar, C., Jean, C., de Jong, J., Katterloher, R., Kiss, C., Klaas, U., Lemke, D., Lutz, D., Madden, S., Marquet, B., Martignac, J., Mazy, A., Merken, P., Montfort, F., Morbidelli, L., Müller, T., Nielbock, M., Okumura, K., Orfei, R., Ottensamer, R., Pezzuto, S., Popesso, P., Putzeys, J., Regibo, S., Reveret, V., Royer, P., Sauvage, M., Schreiber, J., Stegmaier, J., Schmitt, D., Schubert, J., Sturm, E., Thiel, M., Tofani, G., Vavrek, R., Wetzstein, M., Wieprecht, E., & Wiezorrek, E. 2010, *A&A*, 518, L2
- Portegies Zwart, S. F., McMillan, S. L. W., & Gieles, M. 2010, *ARA&A*, 48, 431
- Reach, W. T., Megeath, S. T., Cohen, M., Hora, J., Carey, S., Surace, J., Willner, S. P., Barmby, P., Wilson, G., Glaccum, W., Lowrance, P., Marengo, M., & Fazio, G. G. 2005, *PASP*, 117, 978
- Reed, J. E., Hester, J. J., Fabian, A. C., & Winkler, P. F. 1995, *ApJ*, 440, 706
- Reines, A. E., Johnson, K. E., & Goss, W. M. 2008, *AJ*, 135, 2222
- Reines, A. E., Nidever, D. L., Whelan, D. G., & Johnson, K. E. 2010, *ApJ*, 708, 26
- Rémy-Ruyer, A., Madden, S. C., Galliano, F., Hony, S., Sauvage, M., Bendo, G. J., Roussel, H., Pohlen, M., Smith, M. W. L., Galametz, M., Cormier, D., Lebouteiller, V., Wu, R., Baes, M., Barlow, M. J., Boquien, M., Boselli, A., Ciesla, L., De Looze, I., Karczewski, O. Ł., Panuzzo, P., Spinoglio, L., Vaccari, M., & Wilson, C. D. 2013, *A&A*, 557, A95

- Reynolds, T. M., Fraser, M., & Gilmore, G. 2015, *MNRAS*, 453, 2885
- Rieke, G. H., Young, E. T., Engelbracht, C. W., Kelly, D. M., Low, F. J., Haller, E. E., Beeman, J. W., Gordon, K. D., Stansberry, J. A., Misselt, K. A., Cadien, J., Morrison, J. E., Rivlis, G., Latter, W. B., Noriega-Crespo, A., Padgett, D. L., Stapelfeldt, K. R., Hines, D. C., Egami, E., Muzerolle, J., Alonso-Herrero, A., Blaylock, M., Dole, H., Hinz, J. L., Le Floch, E., Papovich, C., Pérez-González, P. G., Smith, P. S., Su, K. Y. L., Bennett, L., Frayer, D. T., Henderson, D., Lu, N., Masci, F., Pesenson, M., Rebull, L., Rho, J., Keene, J., Stolovy, S., Wachter, S., Wheaton, W., Werner, M. W., & Richards, P. L. 2004, *ApJS*, 154, 25
- Rogers, H. & Pittard, J. M. 2013, *MNRAS*, 431, 1337
- . 2014, *MNRAS*, 441, 964
- Rosen, A. 2015, *IAU General Assembly*, 22, 2255497
- Rosslowe, C. K. & Crowther, P. A. 2015, *MNRAS*, 447, 2322
- Rubin, V. C., Ford, Jr., W. K., & D’Odorico, S. 1970, *ApJ*, 160, 801
- Russell, S. C. & Dopita, M. A. 1990, *ApJS*, 74, 93
- Ryś, A., Grocholski, A. J., van der Marel, R. P., Aloisi, A., & Annibali, F. 2011, *A&A*, 530, A23
- Sales, L. V., Marinacci, F., Springel, V., & Petkova, M. 2014, *MNRAS*, 439, 2990
- Sandage, A. & Katem, B. 1976, *AJ*, 81, 743
- Sander, A., Hamann, W.-R., & Todt, H. 2012, *A&A*, 540, A144
- Sander, A., Todt, H., Hainich, R., & Hamann, W.-R. 2014, *A&A*, 563, A89
- Schaerer, D., Contini, T., & Pindao, M. 1999, *A&AS*, 136, 35
- Schaerer, D. & Vacca, W. D. 1998, *ApJ*, 497, 618
- Schlegel, D. J., Finkbeiner, D. P., & Davis, M. 1998, *ApJ*, 500, 525

- Sidoli, F., Smith, L. J., & Crowther, P. A. 2006, *MNRAS*, 370, 799
- Sidoli, F., Smith, L. J., Crowther, P. A., Vacca, W. D., & Schmutz, W. 2004, in *Astronomical Society of the Pacific Conference Series*, Vol. 322, *The Formation and Evolution of Massive Young Star Clusters*, ed. H. J. G. L. M. Lamers, L. J. Smith, & A. Nota, 217
- Silich, S. & Tenorio-Tagle, G. 2013, *ApJ*, 765, 43
- Simon, R., Schneider, N., Stutzki, J., Güsten, R., Graf, U. U., Hartogh, P., Guan, X., Staguhn, J. G., & Benford, D. J. 2012, *A&A*, 542, L12
- Skinner, M. A. & Ostriker, E. C. 2015, *ApJ*, 809, 187
- Smartt, S. J. 2015, *PASA*, 32, e016
- Smith, L. J., Norris, R. P. F., & Crowther, P. A. 2002, *MNRAS*, 337, 1309
- Smith, N. & Conti, P. S. 2008, *ApJ*, 679, 1467
- Sokal, K. R., Johnson, K. E., Indebetouw, R., & Massey, P. 2016, *ApJ*
- Sokal, K. R., Johnson, K. E., Indebetouw, R., & Reines, A. E. 2015a, *AJ*, 149, 115
- Sokal, K. R., Johnson, K. E., Massey, P., & Indebetouw, R. 2015b, in *Wolf-Rayet Stars: Proceedings of an International Workshop held in Potsdam, Germany, 1-5 June 2015*. Edited by Wolf-Rainer Hamann, Andreas Sander, Helge Todt. Universitätsverlag Potsdam, 2015., p.337-340, ed. W.-R. Hamann, A. Sander, & H. Todt, 337–340
- Stasińska, G. 1990, *A&AS*, 83, 501
- Stevens, I. R. & Hartwell, J. M. 2003, *MNRAS*, 339, 280
- Telles, E., Thuan, T. X., Izotov, Y. I., & Carrasco, E. R. 2014, *A&A*, 561, A64
- Topping, M. W. & Shull, J. M. 2015, *ApJ*, 800, 97

- Tsai, C.-W., Turner, J. L., Beck, S. C., Crosthwaite, L. P., Ho, P. T. P., & Meier, D. S. 2006, *AJ*, 132, 2383
- Tsai, C.-W., Turner, J. L., Beck, S. C., Meier, D. S., & Ho, P. T. P. 2009, *AJ*, 137, 4655
- Tully, R. B. 1988, *Nearby galaxies catalog*
- Tully, R. B., Courtois, H. M., Dolphin, A. E., Fisher, J. R., Héraudeau, P., Jacobs, B. A., Karachentsev, I. D., Makarov, D., Makarova, L., Mitronova, S., Rizzi, L., Shaya, E. J., Sorce, J. G., & Wu, P.-F. 2013, *AJ*, 146, 86
- Turner, J. L., Beck, S. C., Benford, D. J., Consiglio, S. M., Ho, P. T. P., Kovács, A., Meier, D. S., & Zhao, J.-H. 2015, *Nature*, 519, 331
- Turner, J. L., Beck, S. C., & Ho, P. T. P. 2000, *ApJ*, 532, L109
- van den Bergh, S. 1981, *A&AS*, 46, 79
- . 1995, *Nature*, 374, 215
- van der Hucht, K. A. 2001, *NewAR*, 45, 135
- van Zee, L., Salzer, J. J., Haynes, M. P., O'Donoghue, A. A., & Balonek, T. J. 1998, *AJ*, 116, 2805
- Vink, J. S. 2015, in *Wolf-Rayet Stars: Proceedings of an International Workshop held in Potsdam, Germany, 1-5 June 2015*. Edited by Wolf-Rainer Hamann, Andreas Sander, Helge Todt. Universitätsverlag Potsdam, 2015., p.133-138, ed. W.-R. Hamann, A. Sander, & H. Todt, 133–138
- Vink, J. S. & de Koter, A. 2005, *A&A*, 442, 587
- Vink, J. S., de Koter, A., & Lamers, H. J. G. L. M. 2001, *A&A*, 369, 574
- Walch, S. & Naab, T. 2015, *MNRAS*, 451, 2757

- Walch, S. K., Whitworth, A. P., Bisbas, T., Wünsch, R., & Hubber, D. 2012, *MNRAS*, 427, 625
- Walker, A. R. 2012, *Ap&SS*, 341, 43
- Watson, A. M., Gallagher, III, J. S., Holtzman, J. A., Hester, J. J., Mould, J. R., Ballester, G. E., Burrows, C. J., Casertano, S., Clarke, J. T., Crisp, D., Evans, R., Griffiths, R. E., Hoessel, J. G., Scowen, P. A., Stapelfeldt, K. R., Trauger, J. T., & Westphal, J. A. 1996, *AJ*, 112, 534
- Weidner, C., Kroupa, P., & Bonnell, I. A. D. 2010, *MNRAS*, 401, 275
- Weisz, D. R., Johnson, L. C., Foreman-Mackey, D., Dolphin, A. E., Beerman, L. C., Williams, B. F., Dalcanton, J. J., Rix, H.-W., Hogg, D. W., Fouesneau, M., Johnson, B. D., Bell, E. F., Boyer, M. L., Gouliermis, D., Guhathakurta, P., Kalirai, J. S., Lewis, A. R., Seth, A. C., & Skillman, E. D. 2015, *ApJ*, 806, 198
- Werner, M. W., Roellig, T. L., Low, F. J., Rieke, G. H., Rieke, M., Hoffmann, W. F., Young, E., Houck, J. R., Brandl, B., Fazio, G. G., Hora, J. L., Gehrz, R. D., Helou, G., Soifer, B. T., Stauffer, J., Keene, J., Eisenhardt, P., Gallagher, D., Gautier, T. N., Irace, W., Lawrence, C. R., Simmons, L., Van Cleve, J. E., Jura, M., Wright, E. L., & Cruikshank, D. P. 2004, *ApJS*, 154, 1
- Westmoquette, M. S., Smith, L. J., Gallagher, III, J. S., O'Connell, R. W., Rosario, D. J., & de Grijs, R. 2007, *ApJ*, 671, 358
- Whitmore, B. C. 1999, in *IAU Symposium, Vol. 186, Galaxy Interactions at Low and High Redshift*, ed. J. E. Barnes & D. B. Sanders, 251
- Whitmore, B. C. 2003, in *A Decade of Hubble Space Telescope Science*, ed. M. Livio, K. Noll, & M. Stiavelli, Vol. 14, 153–178
- Whitmore, B. C., Brogan, C., Chandar, R., Evans, A., Hibbard, J., Johnson, K., Leroy, A., Privon, G., Remijan, A., & Sheth, K. 2014, *ApJ*, 795, 156
- Whitmore, B. C. & Schweizer, F. 1995, *AJ*, 109, 960

- Whitmore, B. C., Schweizer, F., Leitherer, C., Borne, K., & Robert, C. 1993, AJ, 106, 1354
- Whitmore, B. C. & Zhang, Q. 2002, AJ, 124, 1418
- Williams, J. P. & McKee, C. F. 1997, ApJ, 476, 166
- Wilson, C. D., Petitpas, G. R., Iono, D., Baker, A. J., Peck, A. B., Krips, M., Warren, B., Golding, J., Atkinson, A., Armus, L., Cox, T. J., Ho, P., Juvela, M., Matsushita, S., Mihos, J. C., Pihlstrom, Y., & Yun, M. S. 2008, ApJS, 178, 189
- Wofford, A., Leitherer, C., Chandar, R., & Bouret, J.-C. 2014, ApJ, 781, 122
- Woosley, S. E. & Bloom, J. S. 2006, ARA&A, 44, 507
- Wray, J. D. & de Vaucouleurs, G. 1980, AJ, 85, 1
- Wright, A. E. & Barlow, M. J. 1975, MNRAS, 170, 41